Summer 2015

Nano Scale Mechanical Analysis of Biomaterials Using Atomic Force Microscopy

Diganta Dutta
Old Dominion University

Nano Scale Mechanical Analysis of Biomaterials Using Atomic Force Microscopy

by

Diganta Dutta
B.Sc. April 2004, Chittagong University of Engineering & Technology, Bangladesh
M.Sc. December 2009, University of Ulsan, South Korea

A Dissertation Submitted to the Faculty of
Old Dominion University in Partial Fulfillment of the
Requirements for the Degree of

DOCTOR OF PHILOSOPHY

MECHANICAL & AEROSPACE ENGINEERING

OLD DOMINION UNIVERSITY
August 2015

Approved by:

Shizhi Qian (Director)

Venkat Maruthamuthu (Member)

Xiaoyu Zhang (Member)

Yan Peng (Member)

ABSTRACT

NANO SCALE MECAHNICAL ANALYSIS OF BIOMATERIALS USING ATOMIC FORCE MICROSCOPY

Diganta Dutta
Old Dominion University, 2015
Director: Shizhi Qian

The atomic force microscope (AFM) is a probe-based microscope that uses nanoscale and structural imaging where high resolution is desired. AFM has also been used in mechanical, electrical, and thermal engineering applications. This unique technique provides vital local material properties like the modulus of elasticity, hardness, surface potential, Hamaker constant, and the surface charge density from force versus displacement curve.

Therefore, AFM was used to measure both the diameter and mechanical properties of the collagen nanostraws in human costal cartilage. Human costal cartilage forms a bridge between the sternum and bony ribs. The chest wall of some humans is deformed due to defective costal cartilage. However, costal cartilage is less studied compared to load bearing cartilage. Results show that there is a difference between chemical fixation and non-chemical fixation treatments. Our findings imply that the patients' chest wall is mechanically weak and protein deposition is abnormal. This may impact the nanostraws' ability to facilitate fluid flow between the ribs and the sternum.

At present, AFM is the only tool for imaging cells' ultra-structure at the nanometer scale because cells are not homogeneous. The first layer of the cell is called the cell membrane, and the layer under it is made of the cytoskeleton. Cancerous cells are different from normal cells in term of cell growth, mechanical properties, and ultra-structure. Here, force is measured with very high sensitivity and this is accomplished with highly sensitive probes such as a nano-probe. We performed experiments to determine ultra-structural differences that emerge when such cancerous cells are subject to treatments such as with drugs and electric pulses. Jurkat cells are cancerous cells. These cells were pulsed at different conditions. Pulsed and non-pulsed Jurkat cell ultra-structures were investigated at the nano meter scale using AFM. Jurkat cell mechanical properties were measured under different conditions. In addition, AFM was used to measure the charge density of cell surface in physiological conditions. We found that the treatments changed the cancer cells' ultra-structural and mechanical properties at the nanometer scale.

Finally, we used AFM to characterize many non-biological materials with relevance to biomedical science. Various metals, polymers, and semi-conducting materials were characterized in air and multiple liquid media through AFM - techniques from which a plethora of industries can benefit. This applies especially to the fledging solar industry which has found much promise in nanoscopic insights. Independent of the material being examined, a reliable method to measure the surface force between a nano probe and a sample surface in a variety of ionic concentrations was also found in the process of procuring these measurements. The key findings were that the charge density increases with the increase of the medium's ionic concentration.

This Dissertation is dedicated to wife, parents and brothers

ACKNOWLEDGMENTS

First, I give an abundance of thanks to my dissertation advisor, Dr. Shizhi Qian, as he has provided sound advice throughout my path and has been a steadfast rock of encouragement in tough times. Having him has my mentor and having access to his insight has been a fortunate circumstance, especially with the freedom that he has granted me to explore new projects. Without his grand vision and support for my curiosity, you, the reader, would not be reading this dissertation.

I appreciate the efforts of my dissertation committee members at ODU: Drs. Venkat Maruthamuthu, Xiaoyu Zhang, and Yan Peng, for their help in improving this dissertation. Additionally, I would like to thank Dr. Michael Stacey at the Frank Reidy Research Center for Bioelectrics for the numerous constructive collaborations as well as Xavier-Lewis Palmer, previously from Old Dominion University and now at Eastern Virgina Medical School, for his many volunteer efforts. Everyone above helped significantly in this research and has been an absolute pleasure to work with.

Nomenclature

a	contact radius
A	area
A_H	Hamaker constant
C	Capacitance
c	Speed of light vacuum
C_K	Keesom coefficient
C_D	Debye coefficient
C_L	London coefficient
D	tip-sample distance
e	unit charge
E	Young's modulus
E_1	Young's modulus of probe
E_2	Young's modulus of sample
f	force per unit area
F	force
F_{ad}	adhesion force
F_{el}	double-layer force
F_{vdw}	van der walls force
N_0	Avogadro's constant
h	Planck's constant
k_B	Boltzmann constant
k_c	Spring constant of the cantilever

P	pressure
Q	quality factor
r	distance between atoms or molecules
R	tip radius
T	temperature
U	potential energy
u_1	dipole moment of molecules
u_2	dipole moment of molecules
v	velocity of the tip
I	ionic strength
V	voltage
Z_i	valence ion
α_{01}	electronic polarizabilities of molecules
ε	dielectric constant of the medium
ε_0	vacuum permittivity
λ	Debye length
υ	poisson's ratio
ρ	density
σ_S	surface charge density of sample surface
σ_T	surface charge density of AFM Tip
ρ_f	density of fluid surrounding the cantilever (kg/m3)
σ	molecular diameter (m)
ψ	electric potential

ψ_S	electric potential of sample surface
ψ_T	electric potential of AFM Tip
η	viscosity
π	Pi (3.1415……)
κ	inverse debye length
ω	angular frequency (Hz)
ω_0	angular resonance frequency of the cantilever

TABLE OF CONTENTS

LIST OF TABLES

LIST OF FIGURES

Figure Page

Figure Page

Figure Page

CHAPTER 1

INTRODUCTION TO ATOMIC FORCE MICROSCOPY

1.1 Introduction

In 1986, Binning, Gerber, and Quate invented the Atomic Force Microscope (AFM) and received the Nobel Prize for physics [1]. AFM is the foremost device which provides 3D morphological and ultra-structure images of sample surfaces at very high resolution. It is also a unique tool for nano scale measurements such as sample imaging of physiological conditions, interfacial force measurements between sample and liquid interface, and nano indentation for soft and hard materials [2-6]. At the beginning stage, AFM worked in static mode, which involved the microscope's probe scanning along the sample surface at a constant height. Martin, Williams and Wickramasinghe developed dynamic mode AFM in 1987 [7]. In this mode, the mechanical probe, which works as a sensing element, oscillates above the sample surface. AFM resolution is 1000 times finer than the normal optical microscope. It has many advantages over the scanning electron microscope (SEM) and the Transmission Electron microscope (TEM). AFM operates in liquid, air and vapor environments; whereas SEM and TEM cannot run in liquid environments. In order for the SEM to operate, it must have a high electric field and vacuum environment. Two consequences of using the SEM are increased operating costs and destruction of biological cells; whereas AFM operates in ambient conditions and preserves biological morphology. One could not get true images in SEM and TEM because the samples need to be coated with conductive materials; whereas AFM does not require such special sample preparations. Height images are generated by the AFM probe of the sample

surfaces. The outstanding feature of the atomic force microscope is that it obtains the images at atomic level, enabling new discoveries in many fields such as nanotechnology, life sciences, material science and biotechnology.

Figure 1.1: Photograph of the nanonics AFM setup at ODU biomicrofludics lab.

1.2 AFM Components

AFM typically consists of cantilever, probe, feedback controller, detection mechanism, image processing unit, upper and lower scanner. Figure 1.1 shows a photograph of the

Nanonics AFM setup at ODU Biomicrofluidics Lab. Figure 1.2 shows different components of AFM.

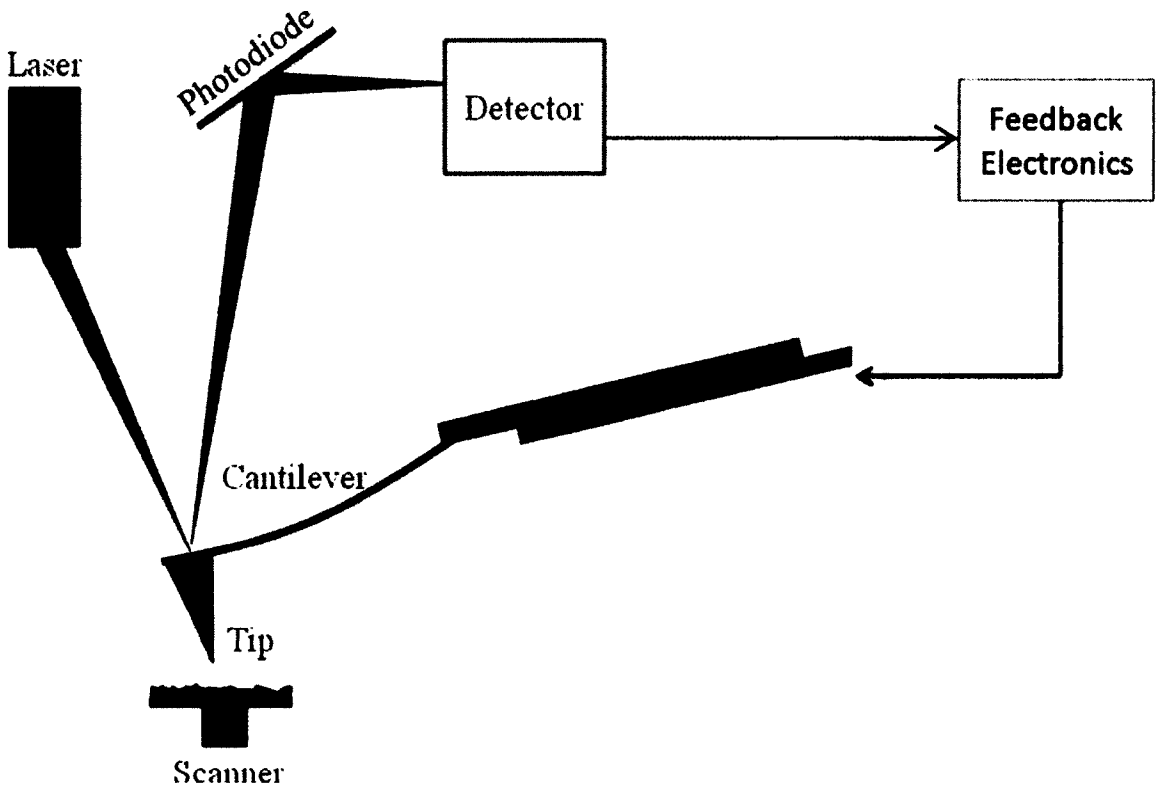

Figure 1.2: Different components of AFM.

1.2.1 AFM Cantilevers

The cantilever is usually a few millimeters in length, a few microns thick, and is flexible and strong. Cantilevers are fabricated with micro fabrication techniques such as lithography and etching methods [8-10]. Most of the AFM cantilevers are made of silicon and silicon nitride and are rectangular and V-shaped [11-15]. Researchers use micro and nano fabricated cantilevers that are specific to certain types of work for optimal measurements such as resonance frequency, quality factor and spring constant.

1.2.2 Tips

AFM image resolutions depend on the size and aspect ratio of the tip [16-19]. Tips are made from different materials such as silicon, silicon nitride, quartz, single wall carbon nano tube, etc [12-13]. They are pyramidal, parabolic and round shaped; and the tip apex is slightly round shaped. The tip's radius varies from 2 nm to 10 microns. Through a variety of micro and nano-fabrication techniques, AFM probes are made in a clean room. Special care is needed since deformations in the desired tip geometry can produce image artifacts. The tip size influences resolution as well; a larger probe radius gives less resolution and a small probe gives higher resolution. For example, one cannot image 60 nm collagen fibers using a 1 micron radius probe. In such a case, using smaller probes is preferred as they can provide the desired resolution. Figure 1.3 shows the AFM tip and cantilever.

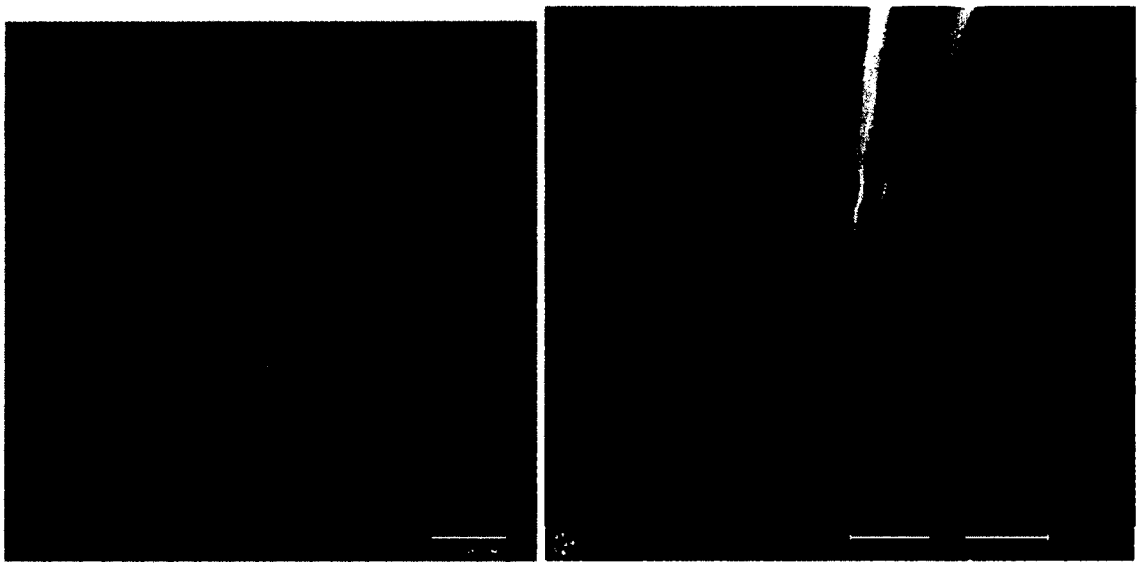

Figure 1.3: SEM images of AFM tip and cantilever (Left SEM Images taken from Nano and More GMBH Website,www.nanoandmore.com/AFM-Probe-ISC-125C40-R.html and right SEM images are from Nanonics).

1.2.3 Scanner

AFM has two scanners- one is the upper scanner and the other is the lower scanner. They are made of piezoelectric elements. They are very small and work very precisely during scanning. Piezoelectric materials expand and contract under applied voltages. The scanner has three independent electrodes in X, Y and Z directions, so they can move precisely in three directions when the tip scans the sample's surface.

1.3 AFM's Working Principal

AFM is a new technique compared to other microscopy methods. Forces act between the tip and sample when the tip approaches the sample surfaces. During the process, the cantilever is deflected, as expected through Hooke's law. Cantilever deflection can be measured in various ways. The common one is the beam bounce method. Laser light is reflected from the top surface of the cantilever and detected into a photodiode [20]. Another AFM working technique is piezoelectric cantilevers. Using the micro fabrication process, these cantilevers are made of piezoelectric materials. The main features of these materials are to expand or contract with applied voltage, like a strain gauge. The cantilever is deflected when AFM piezoresistive cantilevers are brought too near or touch the sample surface. The amount of cantilever deflection can be measured using Wheatstone Bridge Principal.

1.4 AFM Scan Mode

There are two basic ways in which AFM imaging can be performed: one is the static (or contact) mode and the other is the dynamic mode. Dynamic mode can also be divided

into non-contact mode and tapping mode. Figure 1.4 shows repulsive force experienced in contact mode operation, attractive force experienced in non-contact mode operation, and attractive as well as repulsive forces experienced in the tapping mode operation.

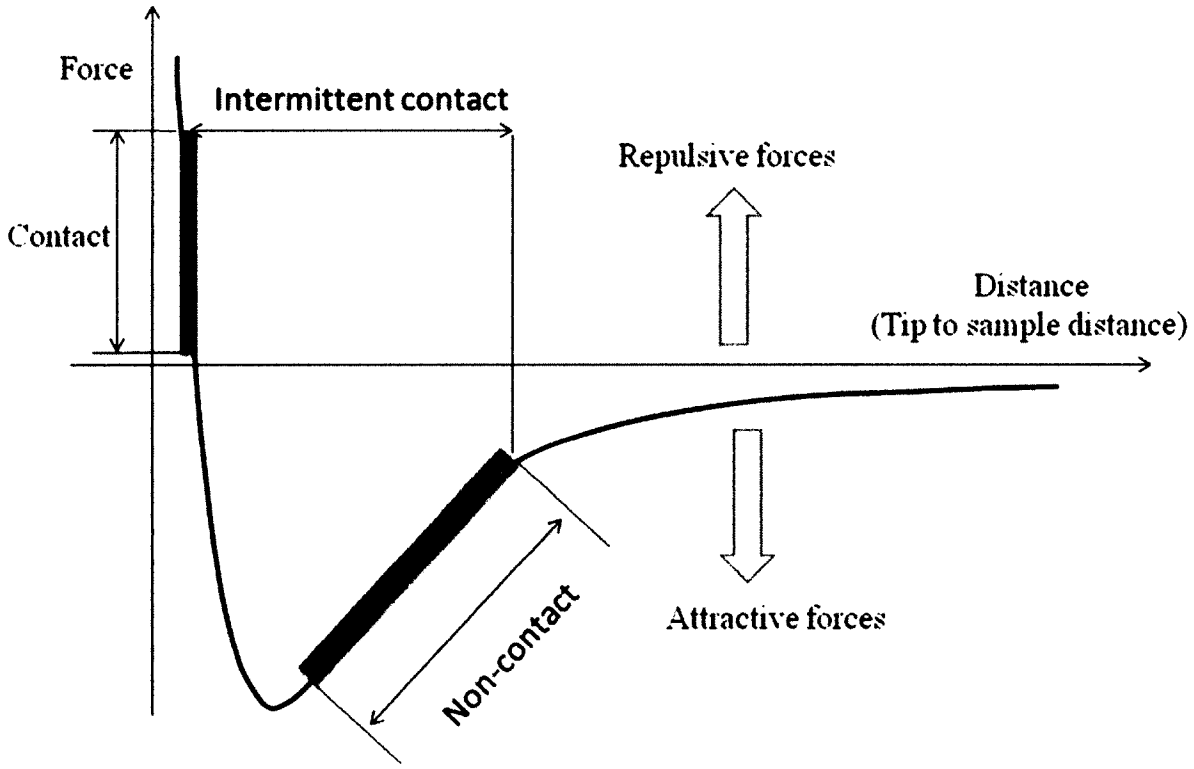

Figure 1.4: Attractive and repulsive forces experienced in different scanning modes (http://pafezov.gloxx.com/?c=9&p=299).

1.4.1 Contact Mode

Static mode is also known as the contact mode. In contact mode, the tip is dragged above the sample surface and generates height images. In contact mode scanning, the overall force is repulsive. It is the easiest mode of scanning operation. It takes less scanning time,

and tip loading forces are controlled more accurately. In contact mode, the AFM tip touches the sample, and as a result, the tip loading force is high. However, it can manipulate a biological sample as the tip touches the surface [21]. AFM probes degrade over time, resulting in a build-up of artificial images, leading to a need for replacements. After detecting the cantilever deflection, the AFM can generate image data in two ways: one is the constant-height mode and the other is the constant-force mode.

The Constant Height Mode

In constant height mode, change of the cantilever deflection is used to generate height images, and the height of the scanner is fixed during the scanning. The advantage of constant height mode is that it generates topographic images at an atomic scale. For this mode, the tip and surface interaction force varies from 10^{-10} to 10^{-8} N for scanning. Flat surfaces are preferable for this mode. The main disadvantage of this mode is that the probes can collide with the surface if one scans with a constant height, increasing the chance of both generating artifacts and damaging the probe. This problem can be solved by applying a feedback mechanism in constant force mode.

The Constant Force Mode

The constant force mode is useful for most applications. In this mode, deflection of the cantilever is constant but the scanner moves up and down. The interaction force between the tip and the sample is constant, and the tip and sample distance is always adjusted with the help of the feedback mechanism. In this mode, scanning speed is slow due to the

feedback circuit response. As a result, there are possibilities for thermal drift for slow scanning speed, and noise occurs during the scanning.

1.4.2 Non-Contact Mode

In non-contact mode, the tip does not touch the sample surface. There is no tip or sample degradation, which is a typical problem occurring in the contact mode operation. At resonance frequency the cantilever tip is oscillating above the sample surface. The amplitude of the oscillation is less than 10 nm where the Van der Waals force is strong. Long range forces such as electrostatic forces are present between the tip and the sample in this case. The resonance frequency of the cantilever decreases due to long range forces, and it can increase by adjusting the average distance between tip and sample. Tip loading forces are low, and there is no sample manipulation and no contamination of AFM tip because the tip does not touch the sample surface. Topographic images are generated by scanning software and every (x, y) data is collected from tip and sample distance [22].

Contact and non-contact mode topography images are not the same for hard surfaces. In ambient conditions, sometimes there is a thin liquid monolayer above the sample surfaces. In this case, the images of contact and non-contact mode are different. In the contact mode, the tip penetrates the liquid surfaces to generate the underlying surface image. In non-contact mode, images are generated above the liquid surface. If we scan the sample surface several times by the contact mode method, there is the possibility of damage to the tip. On the other hand, the tips do not suffer from this problem in non-contact mode operations. From the above discussion we can say that non-contact mode is preferable for scanning biological cells and tissues.

Frequency and amplitude modulation are included in the dynamic mode operation. By changing the oscillation frequency we obtain the sample topography from the frequency modulation mode. Advantages of the frequency modulation mode are that it provides atomic level resolution and can be used with a very stiff cantilever, which gives high stability above the sample surface. Amplitude modulation can be used in both non-contact and tapping modes. By changing the phase oscillation we can distinguish different types of materials using the amplitude modulation mode.

1.4.3 Tapping Mode

Tapping mode is also known as the intermittent contact mode. From the name, the AFM tip periodically touches the sample surface. In tapping mode, the cantilever is oscillating at resonance frequency by piezoelectric materials. These materials are attached on the AFM tip holder. In non-contact mode, the cantilever can oscillate with amplitude of 10 nm; whereas in tapping mode the cantilever oscillation amplitude can be as high as 100 nm. The interaction forces between the tip and sample increase when the tip comes very close to the surface. In tapping mode, the tip loading force is very low and the tip touches the surface periodically. In this mode, the tip can manipulate the sample and there is the possibility of contamination of the tip as the tip touches the surface. In this mode, three types of data are collected: height, phase and amplitude.

Height Data

The cantilever is excited by resonance frequency through the piezo-electric drive, and the oscillation amplitudes are used for generating height images. When the tip scans the

surfaces, its vertical position changes and these changes are controlled and monitored by the xyz scanning piezo-tube.

Topography images can be generated by changing the z-axis. These data are good enough for height imaging but they do not show the clear edge of the samples. Figure 1.5 shows Jurkat cell AFM height image in air. These Jurkat cells are fixed above poly lysine cover slips. The bio samples were collected from ODU Frank Reidy Bioelectrics Center.

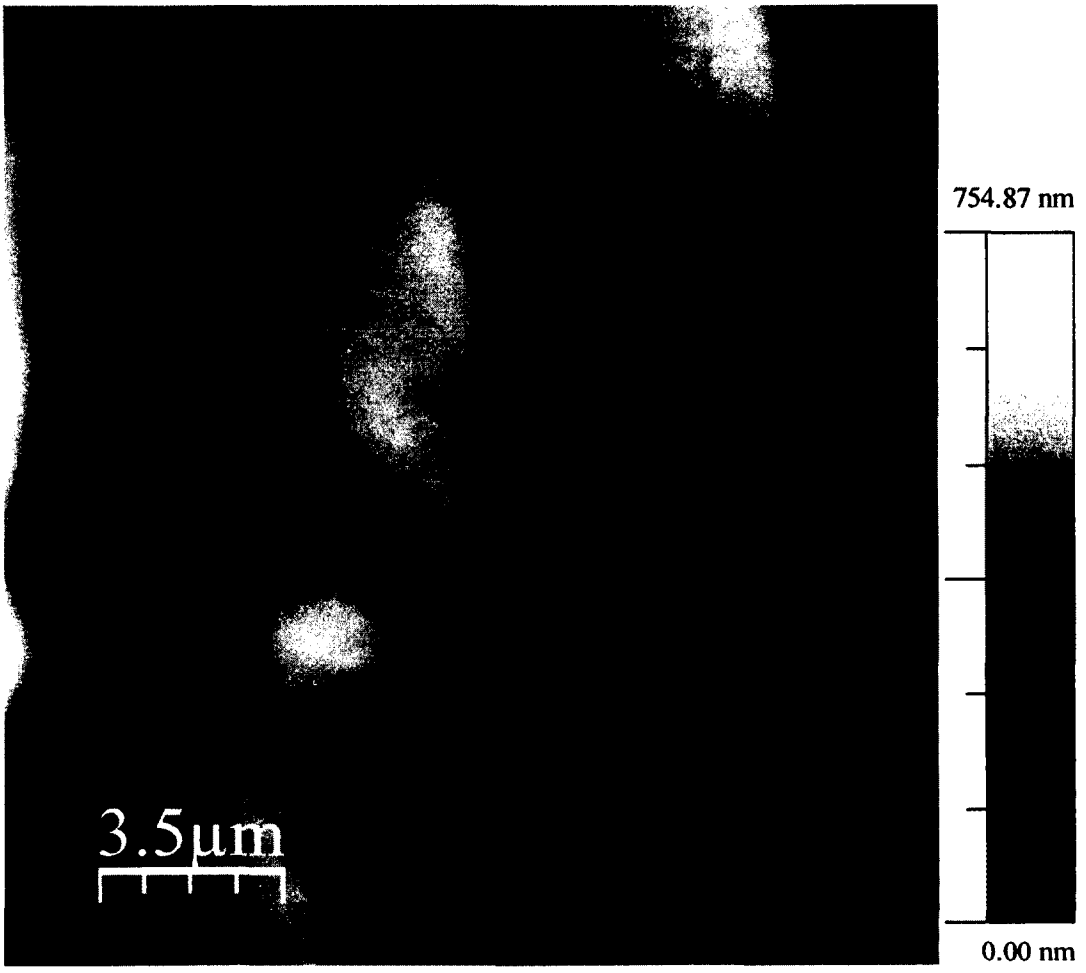

Figure 1.5: 17.4 x 17.4 μm AFM Jurkat cells height image.

Phase Data

Phase images can be generated from the change of the phase offset or phase angle. Phase change between the two signals is set to zero when the tip is oscillated high above the sample surface. Phase change occurs when the tip touches the sample. Phase angles of the two signals also change when it scans at different elasticity of the materials. These phase changes are plotted and called phase imaging. Figure 1.6 shows Jurkat cell AFM phase image in air. The AFM height images are not as clear as the phase image.

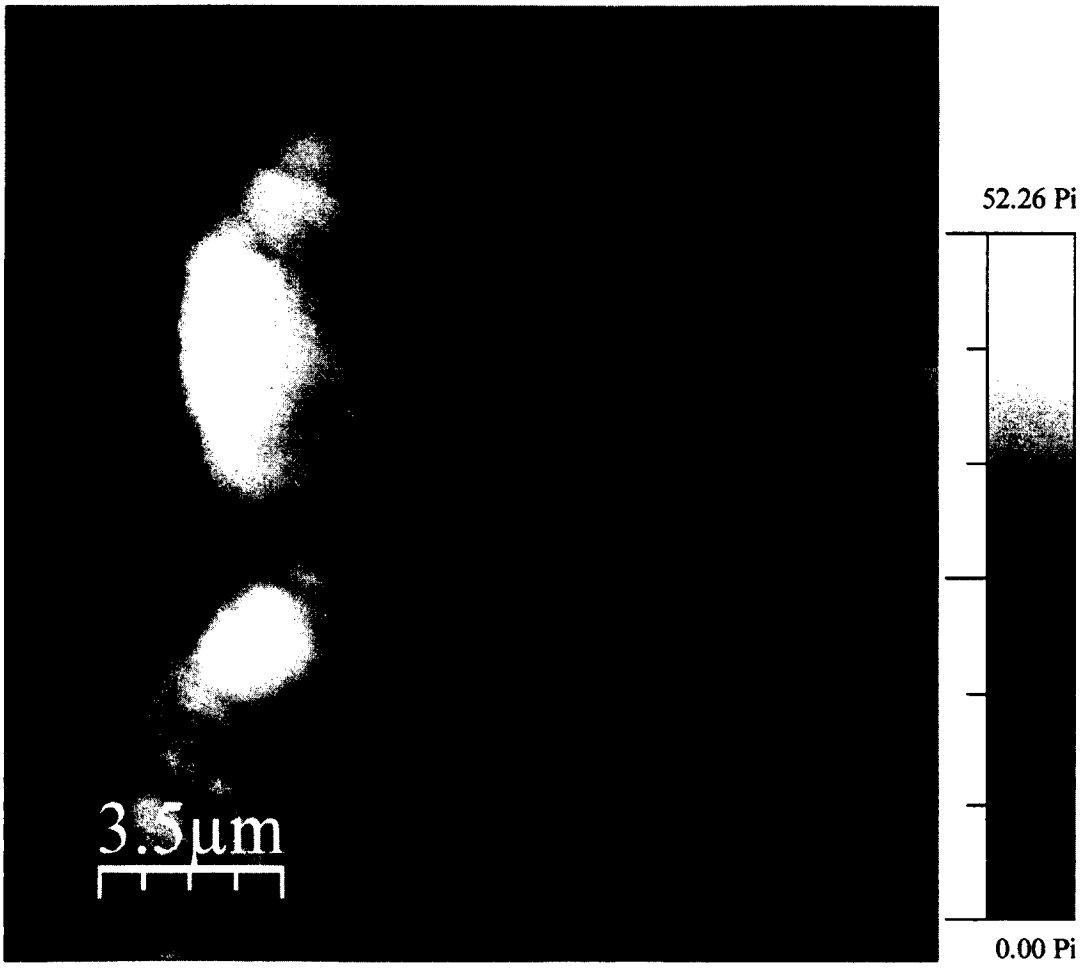

Figure 1.6: 17.4 x 17.4 µm AFM Jurkat cells phase image.

1.5 Advantages

AFM has several advantages compared to the optical, transmission electron and scanning electron microscopes. AFM generates 2D and 3D images where SEM can only generate 2D images. SEM requires special surface treatment that may change the original topography of the samples, but AFM does not require these treatments. AFM works in air and liquid as well as in a vacuum. On the other hand, SEM works better in a vacuum.

Only AFM can execute all types of engineering applications like force, electrical, thermal measurements. AFM gives us true atomic level topography images with very high resolution. TEM is also a powerful microscopy tool, which has nanometer scale resolution. However, TEM cannot work in liquid, and sample surfaces must be ultra-thin so that electrons can pass through the sample surfaces. AFM does not have such restrictions like TEM. Optical microscopy resolution is 1000 times lower than AFM. It is only used for imaging purposes. AFM can be used for electrical, thermal and mechanical measurements, while TEM, SEM and optical microscopy cannot perform these special measurements.

1.6 Disadvantages

To scan sample sizes on the order of 20 x 20 micrometers, AFM takes about 30 minutes; whereas SEM would image that size sample in a few minutes. Another disadvantage is that AFM can only scan about 35 x 35 micrometers at a time, but SEM can scan square millimeters. Furthermore, there are possibilities of creating thermal drifts for this slow scanning speed, resulting in artificial images. Some of the AFM images have image artifacts and these are introduced by broken tip, rough sample surface, coarse tip and unfavorable operating conditions. Nowadays, these problems can be eliminated by using image processing software. One more disadvantage is the difficulty of AFM to scan on steep walls of a sample's surface. Rough sample surfaces require special types of tips that can increase AFM's overall cost.

1.7 AFM Use in Biological Applications

AFM can be used for imaging biological cells. One of the valuable features of AFM for biological applications is the ability of investigating living biological tissues/cells. For this purpose biological cells are attached above a cover slip. For hard surfaces, AFM resolution is about atomic scale. For soft surfaces, like biological cells, AFM resolution is about 1 nm [23]. AFM is widely used to obtain cell morphology. A number of researchers have investigated biomechanical properties of biological cells using AFM [24], such as hardness, modulus of elasticity and adhesion. AFM can also detect DNA. Nowadays, researchers use AFM for the study of cancer cells, which exhibit different properties from normal cells in their stiffness, growth, mechanics and morphology. Optical and confocal microscopies are also used for imaging cells, but they cannot detect cells' stiffness, morphology, mechanics, ultra-structure and interaction between cells. Hence, AFM becomes the foremost tool for biological cell study. The following paragraph only lists some examples of the use of AFM to determine the mechanical properties of cartilage samples.

Stolz et al. [25] measured the modulus of elasticity of articular cartilage at micro and nano size AFM probe. They showed that micron sized probes cannot image nano sized collagen straws. Heim et al. [26-27] investigated native collagen fibrils' modulus of elasticity as 1-2 GPa. Yang et al. [28] determined cross link collagen-fibrils' young modulus as 3.8 GPa and native collagen fibrils' modulus of elasticity as 1.4 GPa. Yang et al. [29] measured type-1 collagen fibrils bending modulus ranging from 1 to 3.9 GPa. They also measured shear modulus 74 MPa in air, and 3.4 MPa in PBS buffer. Stacey et

al. [30] measured human costal cartilage modulus of elasticity at ambient condition and in PBS buffer as 2.06 GPa and 23 MPa, respectively. Wenge et al. [31] obtained Young modulus of elasticity of rat tail type-1 collagen fiber ranging from 5 GPa to 11.5 GPa at ambient conditions. The biomechanical properties of Cancer cells were investigated [32-35].

1.8 Use of AFM to Measure Interaction Force

Surface forces between liquid and solid interfaces play a vital role in colloidal sciences. AFM has been used to measure surface forces between the approaching AFM tip and sample surface [36]. Islam et al. [37] introduced the surface charge regulation model. Sample surface was ionized when AFM probes were immersed in liquid due to ionization process. In their model, they showed surface charge variation due to the change in pH and ionic concentration. Ducker et al. [38] also made interfacial force measurements between 3.5 micron AFM probe and flat surface. They showed how the force curves vary with changing ionic concentration and pH values. Li et al. [39] performed surface force measurements between pairs of micron size polystyrene spheres at different ionic concentrations. They showed long range repulsive forces below 0.01M KCl solution. They also measured adhesion forces, and their results vary from experiment to experiment. At 1mM KCl solution, they fitted their experimental data with theory and got surface potential 87 mV and Debye length 7.7 nm. Prica et al. [40] measured interaction forces between AFM colloidal probe and zirconia flat plate at different ionic concentrations and pH values. They demonstrated that their results best fit with the DLVO theory at a constant charge and a constant potential. Veeramasuneni et al. [41-42]

made AFM force measurements between sphere silica and α alumina at different pH values, and showed good agreements between theory and experiments. They also showed that the interfacial forces are repulsive at high pH values and attractive at low pH values. Hu et al. [43] measured surface force between modified colloid probes and modified gold substrates. The gold substrate was coated with sodium dodecyl sulfate. The AFM probe made of silica was also modified to have negative surface charge. They fitted their experimental results with electrostatic theory at constant charge. Kanda et al. [44] worked on AFM force measurements in a water–alcohol solution, and measured interaction and adhesion forces between silica and mica surfaces. They did not observe any significant difference in the force curves between low alcohol concentrations and aqueous solution. But at high alcohol concentrations, interaction forces decreased and the adhesion forces were increased. Chin et al. [45] measured surface forces between AFM probe and a glass plate in solutions. They showed long range repulsive forces and the magnitude of the force decreased with an increase in ionic concentration. Their experimental results showed very good agreement with DLVO theory up to 3 nm separation distances. Nguyena et al. [46] measured hydrodynamic forces between AFM colloid particle and a bubble in DI water and aqueous solutions with different ionic concentrations. Their results showed very good agreements between experimental data and the theoretical hydrodynamic forces.

1.9 Objectives of the Studies in this Dissertation

The objectives of the studies in this thesis include:

1) Measurements of topography of hard and soft surface materials in air and buffer solutions
2) Measurements of mechanical properties of polymeric materials, biological cells and tissues
3) Measurements of chemical properties of biological cells in ionic concentrations
4) Measurements of interfacial forces.

Objective 1 is achieved by measuring the topography of silicon surface in air and buffer solutions, followed by topography of collagen nano straws in human cartilage under six different preparation conditions, as well as pulsed and nonpulsed Jurkat cells.

Objective 2 is achieved by measuring the Young modulus of elasticity of PDMS, collagen nano-straws, and pulsed and nonpulsed Jurkat cells.

Objective 3 is achieved by mapping the surface charge density of pulsed and nonpulsed Jurkat cells.

Objective 4 is achieved by measuring the interfacial forces between quartz AFM tips and silica surface in various concentrations of KCl solutions. AFM results are compared with predictions from the existing DLVO theory.

1.9.1 Outline of the Dissertation

Chapter 1 describes the introduction of Atomic Force Microscopy, working principal of AFM, operation mode of AFM, AFM advantages and disadvantages, biological applications of AFM and the use of AFM for interaction force measurement. Chapter 2 describe the fundamentals of the interfacial forces and the experimental results of the interaction force between AFM tips and silica surfaces in 0.1 M, 0.01 M, 0.001 M and 0.0005 M KCl solutions. Van der Waals forces are measured between AFM probe and silica surface in DI water. Chapter 3 discusses the nano-indentation and results on mechanical properties of collagen nanostraws in both air and PBS buffer solution. In addition, the diameters of collagen nanostraws are estimated from the obtained AFM images. Chapter 4 investigated the effects of nanosecond pulses on cancer cells' morphology, mechanical and charge properties. Chapter 5 concludes the thesis with a list of future work.

CHAPTER 2

AFM MEASUREMENTS OF INTERACTION FORCE IN AQUEOUS SOLUTIONS

2.1 Introduction

Colloid means adhesive, and this word was first used by Thomas Graham in 1861 [47]. Colloidal systems have been used since the start of human civilizations [48]. For example, colloidal pigments were used for painting purpose during the Stone Age. Daily necessities like soap and cosmetics were made by the manipulation of colloidal systems. Interfacial forces are the forces experienced between two bodies. Surface Force Apparatuses (SFA) have been used for force measurements for the last 40 years [49-51]. Tabor et al. [52] conducted Van der Waals force measurements between two surfaces using SFA. SFA have 1 micron resolution and the force sensitivity is 10^{-8} N. Researchers worked extensively to measure the surfaces forces between two microscopic samples by SFA before the invention of Atomic Force Microscopy [52-59]. With the advancement of cutting edge technology within AFM, researchers are better able to measure Pico-Newton level forces with AFM [60]. AFM resolution is at the angstrom level, and the force sensitivity is about 1-10 pN. Both AFM and SFA work similarly. The main difference between AFM and SFA is that AFM measures force between a small probe and the surface while SFA measures force between two macroscopic bodies. In addition to the development of the experimental techniques for measuring the interfacial forces, in 1941 Derjaguin-Landau and Verwey-Overbeek (DLVO) developed a theory for attractive Van der Waals forces and electrostatic forces between two samples [61-71].

Four basic interaction forces exist and they can be divided into two categories: the short and long range forces. Strong and weak forces act over short ranges, while electromagnetic and gravitational forces act over long range. The interfacial forces include Van der Waals, electrostatic, hydration and steric forces. These forces are again divided into short and long range forces. These forces are dominated when the AFM probe and sample separation distance is about a nanometer. Interfacial forces between the AFM probe and the surface depend on the Hamaker constant, surface charge, and surface potential of materials. Electrostatic long range forces were measured at different ionic concentrations. Short range Van der Waals forces were measured in DI water.

Many researchers have been using the unique AFM tool for interfacial force measurements between two surfaces. Larson et al. [72] measured interfacial force between titanium dioxide colloid and single crystal in ionic solution. They measured interaction forces by changing pH values and ionic concentrations. Their experimental results show good agreement with theoretical Debye length. Vinogradova et al. [73] measured forces between pairs of polystyrene particles in electrolyte solution. They observed long range repulsive forces below 0.01 M KCl concentration. Their 0.001 M KCl concentration results show a good fit with the DLVO theory. Fielden et al. [74] measured interaction force between air bubbles and silica particles in electrolyte. They observed repulsive forces at long ranges and attractive forces when bubbles and AFM tip distance decreases.

Meagher et al. [75] investigated hydrophobic interaction force between modified AFM tip and polypropylene surface in NaCl solution. They measured attractive interaction force when the separation distance is about 30 nm. Christenson et at. [76] measured attractive hydrophobic force between two mica surfaces in divalent solutions. In their experiments, they used magnesium sulfate at different ionic concentrations and they also showed interaction magnitude decreased with increasing ionic concentration. Parker et al. [77] investigated force measurements between AFM tips and functionalized glass surface in NaCl solution. They showed the magnitude of the force reduced with increasing of high salt concentration, but the attractive force magnitude increased. Kokkoli et al. [78] found that the strength of attractive force decreased when adding ethanol to water. They also showed hydrophobic attractive force magnitude close to the Van der Waal when ethanol mole fraction increased about 75%. Dorobantu et at. [60] performed a force measurements investigation between AFM tip and gold surface. Both surfaces are functionalized with bacteria. Their results showed very good agreement with extended DLVO theory.

Colloidal science, biomolecular transport and drug delivery mostly used silica particles [79-88]. One of the objectives of this study is to get the fundamental understanding of nano particles in salt concentration at a very small scale. In this study, we quantify the force magnitude between micro and nano sized probes and a smooth flat surface under salt solutions. We also figured out the force trend in varying salt concentrations. In this study, we investigated how ions changes in solution with increasing salt concentrations. Our study shows that charge density increased with increase of ionic concentrations.

2.2 Method and Materials

2.2.1 Sample Preparation

The sample surfaces were taken from a big silica wafer (Montco Silicon Technologies, San Jose, CA, USA) and it was cut into 1 cm x 1 cm. These silica surfaces were sonicated with 1 M KOH (Acros Organics, New Jersey, USA) solution for about 15 minutes. Then these samples were rinsed with DI water for about 2 to 3 minutes. The sample surfaces were sonicated with acetone for about 15 minutes. After this step, the samples were rinsed with acetone (Fisher Scientific, Pittsburgh, PA, USA) followed by DI water for about 2 to 3 minutes. These sample surfaces were then sonicated with isopropanol (Fisher Science Education, Pittsburgh, PA, USA) for another 15 minutes; after this process, they were rinsed with isopropanol and DI water for about 2 to 3 minutes. Finally, sample surfaces were sonicated with DI water following a 15 minute rinse with acetone, ethanol and DI water. These samples were dried with an air gun and then put above a hot plate at 120 °C for 3 minutes. These sample surfaces were kept in the clean boxes so that dust could not deposit above sample surfaces. Before the experiments, I kept these samples above the microscopic sample holder. AFM probes, made of fused silica, were bought from Nanonics, Israel.

2.3 DLVO Theory

2.3.1 Van der Waals Force

Van der Waals forces are the sum of attractions and repulsions between atoms, not counting ionic electrostatic interactions or those of covalent bonding [89]. An Electromagnetic field is created when two particles approach each other at less than 10 nm apart and electrons move between particles. Van der Waals forces consist of three different kinds of forces such as Keesom force, Debey force and Dispersion force [90]. Dipole-dipole interactions between atoms or molecules are also known as Keesom forces. The interaction potential is [90]

$$w(r) = -\frac{u_1^2 u_2^2}{3(4\pi\varepsilon\varepsilon_0)^2 k_B T r^6} = -\frac{C_K}{r^6} \tag{2.1}$$

Where $w(r)$ is the Keesom potential energy, k_B is the Boltzmann constant, T is the temperature, r is the distance between atoms, C_K is Keesom coefficient, ε is the relative dielectric constant, ε_0 is the dielectric constant of vacuum, u_1^2 is the dipole moments of one molecule, u_2^2 is the dipole moments of another molecule, and π is the constant. Dipole-induced dipole interactions between atoms or molecules are also known as Debye forces. The interaction potential is [90]

$$w(D) = -\frac{u^2 \alpha_0}{(4\pi\varepsilon\varepsilon_0)^2 r^6} = -\frac{C_D}{r^6} \tag{2.2}$$

$w(D)$ is the Debye potential, α_0 is the electronic polarizability, r is the distance, C_D is Debye coefficient and u is the dipole moment.

Another name for the Dispersion force is London force. Dispersion forces are nonadditive and bring atoms or molecules closer as well as align them. Dispersion force interacted between instantaneous dipole-induced dipole. The interaction potential is [90]

$$w(L) = -\frac{3}{2}\frac{\alpha_{01}\alpha_{02}}{(4\pi\varepsilon_0)^2 r^6}\frac{h\upsilon_1\upsilon_2}{(\upsilon_1+\upsilon_2)} = -\frac{C_L}{r^6} \tag{2.3}$$

$w(L)$ is the dispersion potential, h is Planck constant, $\upsilon_1\upsilon_2$ are the frequency of the electron, C_L is London coefficient, α_{01} is the electronic polarizability of one molecule, and α_{02} is the electronic polarizability of another molecule.

The most simplified approximation of the Van der Waals force between a sphere and a flat surface is [90]

$$F_{vdw} = -\frac{AR}{6h^2}\ . \tag{2.4}$$

In the above, R is the radius of the sphere, A is the Hamakar constant, and h is the separation distance.

2.3.2 Electrostatic Force

Due to the ionization or dissociation process, solid surfaces become charged in aqueous solutions [90]. These ions on the silica surfaces are attracted by the equal and opposite charged ions in liquid and are distributed very close to the silica surfaces. Consequently, electrical double layers form between the liquid and silica surface. The thickness of the double layer depends on the ionic concentration and varies from less than a nanometer to hundreds of nanometers. The AFM probe also becomes charged when it is immersed in liquid. Electrostatic force occurs when the double layer of AFM tip overlays with the

double layer of the silica surface. The electrostatic force becomes repulsive when the surface charges of AFM tip and silica surface are similar.

Poisson equation is used to describe the potential distribution in the gap between the AFM tip and the silica surface,

$$\varepsilon\varepsilon_0\nabla^2\Psi = -\rho_f . \tag{2.5}$$

In the above, Ψ is the electric potential within the electrolyte solution, ε is the relative permittivity of the solution, and ρ_f is the free charge density.

The free charge density is [90]

$$\rho_f = \sum_{i=1}^{N} z_i e n_i , \tag{2.6}$$

With e being the charge of electron, n_i and z_i being the ionic concentration and valance of the i^{th} species, and N being the total number of ions in the solution.

Without external field, the ionic concentration is governed by the Boltzmann distribution,

$$n_i = n_{i\alpha} \exp\left(-\frac{z_i e\Psi}{k_B T} \right) , \tag{2.7}$$

With $n_{i\alpha}$ being the bulk ionic number concentration for the ith species.

The corresponding Debye length for binary z:-z electrolyte solution is

$$\kappa^2 = \frac{1}{{\lambda_D}^2} = \frac{2e^2 z^2 n_\alpha}{\varepsilon\varepsilon_0 k_B T} . \tag{2.8}$$

The Osmotic pressure is described by

$$-\rho_f \nabla\psi = \nabla p . \tag{2.9}$$

When the surface pontials or charge densities of the two objects are relatively low, Butt et al. [91] derived the electrical double layer force at constant potentials and surface charge densities,

$$F_{EDL} = \frac{2\pi R\varepsilon\varepsilon_0}{\lambda_D}\left[2\Psi_a\Psi_b e^{-h/\lambda_D} - (\Psi_a^2 + \Psi_b^2)e^{-2h/\lambda_D}\right], \tag{2.10}$$

And

$$F_{EDL} = \frac{2\pi R\lambda_D}{\varepsilon\varepsilon_0}\left[2\sigma_a\sigma_b e^{-h/\lambda_D} + (\sigma_a^2 + \sigma_b^2)e^{-2h/\lambda_D}\right] \tag{2.11}$$

2.3.3 Derjaguin-Landau-Verwey-Overbeek (DLVO) Theory

In colloidal science, particles coalesce or flocculate depending on the combination of attractive and repulsive forces. This idea was first developed by the Derjaguin and Landau in 1941 and in 1948 Verwey and Overbeek presented similar results. DLVO theory is based on electrostatic force and Van der Waals's force in liquids [92-115]. For DLVO theory, surface charge density and potentials are constant for two interacting bodies [116-125].

DLVO force objects for constant potentials [94]:

$$F = -\frac{AR}{6h^2} + \frac{2\pi R\varepsilon\varepsilon_0}{\lambda_D}\left[2\Psi_a\Psi_b e^{-h/\lambda_D} - (\Psi_a^2 + \Psi_b^2)e^{-2h/\lambda_D}\right] \tag{2.12}$$

DLVO force for objects with constant charges [94]:

$$F = -\frac{AR}{6h^2} + \frac{2\pi R\lambda_D}{\varepsilon\varepsilon_0}\left[2\sigma_a\sigma_b e^{-h/\lambda_D} + (\sigma_a^2 + \sigma_b^2)e^{-2h/\lambda_D}\right] \tag{2.13}$$

2.4 Results

All AFM experiments were carried out by commercially available Nanonics Multiview-4000 multi-probe AFM. Interfacial forces were measured between AFM tip with 10 nm radius of curvature and silica surface at different KCL solution. For AFM image calibration, I used the standard silicon grid imaging. The AFM scanning images were taken in air at room temperature. The scanning speed was 30 microns per second. Before imaging the sample surface, we waited for 30 minutes to stabilize the system. I checked resonance frequency and quality factors of the AFM tip. The resonance frequency was 31,580 Hz and quality factor was 1,058. These values were matched with the manufacturer's values. The AFM nano tip radius of curvature was 10 nm. Figure 2.1 shows the silicon grid AFM topography image. The AFM scanning area was 30 micron x 16.1micron.

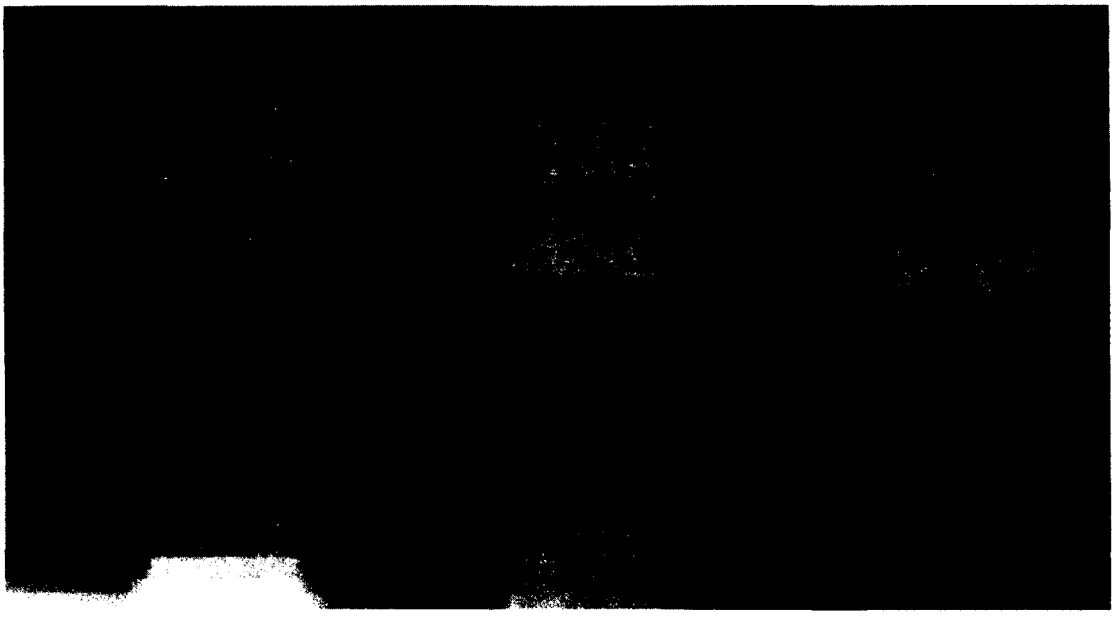

Figure 2.1: Silicon grid AFM topography image.

Figure 2.2 shows the silicon grid height profile at the specific area (green solid line in Figure 2.1).The silicon grid height is about 120 nm, which was obtained from the vendor. My AFM silicon grid images showed very close value.

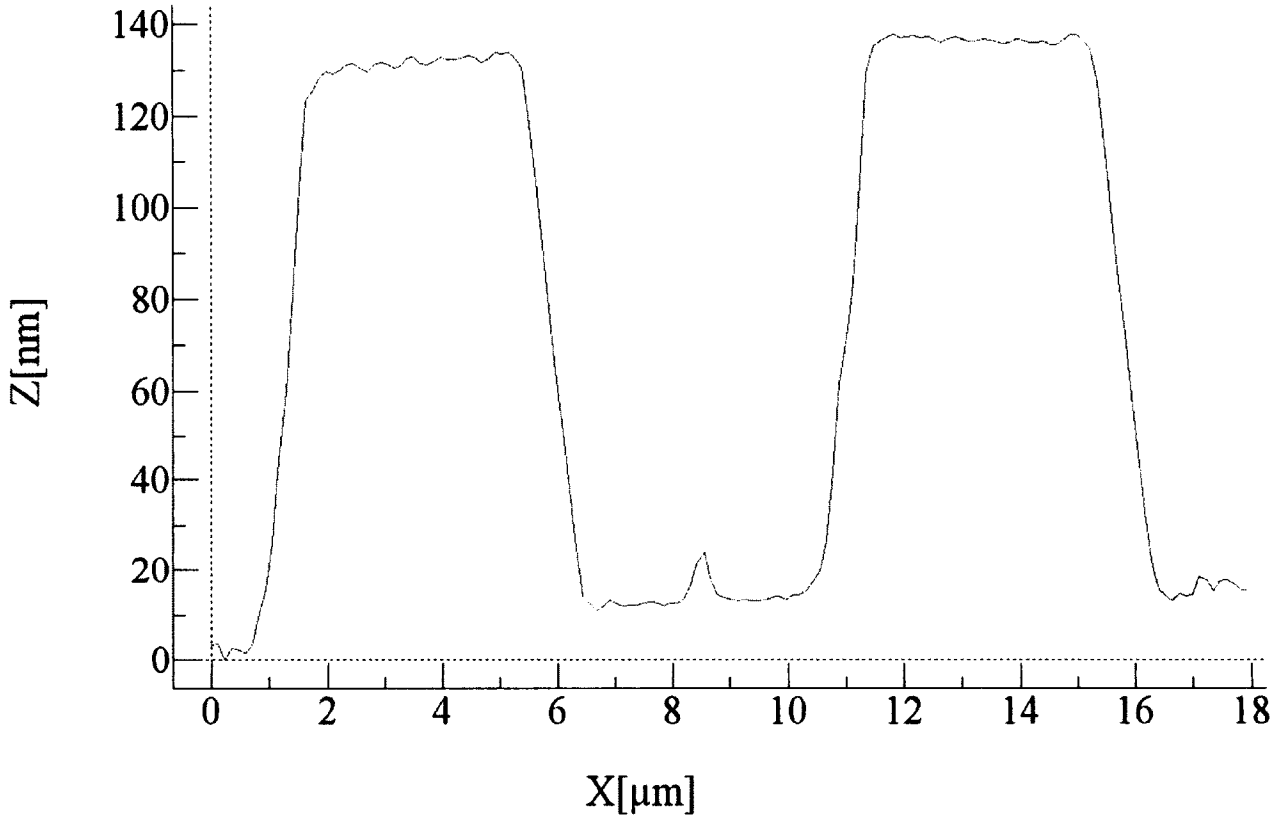

Figure 2.2: Silicon grid height profile.

Before doing interfacial force measurements, we examined silica surfaces roughness. The AFM scanning images were taken in air at room temperature. The AFM scanning area is 10 x 10 μm^2. The scanning speed was 20 micron per second. Figure 2.3 shows the silica surface AFM topography image. The resolution of the AFM image is very high and its vertical resolution is less than 1 nm.

Figure 2.3: Silicon wafer 10 x 10 μm AFM topography image.

Interfacial forces were measured between AFM tip with 10 nm radius of curvature and silica surface at different KCL solution.

2.4.1 Force Measurements using Colloid Probe

The colloid probe was made of quartz. The interaction force between the AFM's colloidal tip and silica surface was measured in 0.1M KCL solution. Figure 2.4 shows the experimental results along with fitted curves by the DLVO theory with constant surface charge densities. The solid red line represents the theoretical results, and the solid blue line represents the experimental one. The experimental curve shows a maximum force of about 2.2 nN when the probe reaches to the sample surface. The double layer thickness is about 0.96 nm at 0.1 M KCL solution, and hence, the electrical double layer forces are experienced when the AFM tip and the substrate are about 2 nm apart. Figure 2.4 shows

repulsive forces due to the similarly charged surfaces. The experimental curve was fitted with the DLVO theory with constant surface charge densities by using a Matlab code to estimate the surface charge densities of the probe tip and the silica substrate. Table 2.1 shows the surface charge densities of the AFM tip and silica surface. The maximum tip surface charge density was -0.013318248 C/m^2 and the minimum was -0.012455295 C/m^2. The maximum silica surface charge density was -0.013319725 C/m^2 and the minimum value was -0.012452229 C/m^2. The average and SD curve fit results in tip and silica surface charge densities of -0.01287 (± 0.00036) C/m^2 and -0.01287 (± 0.00036) C/m^2, respectively.

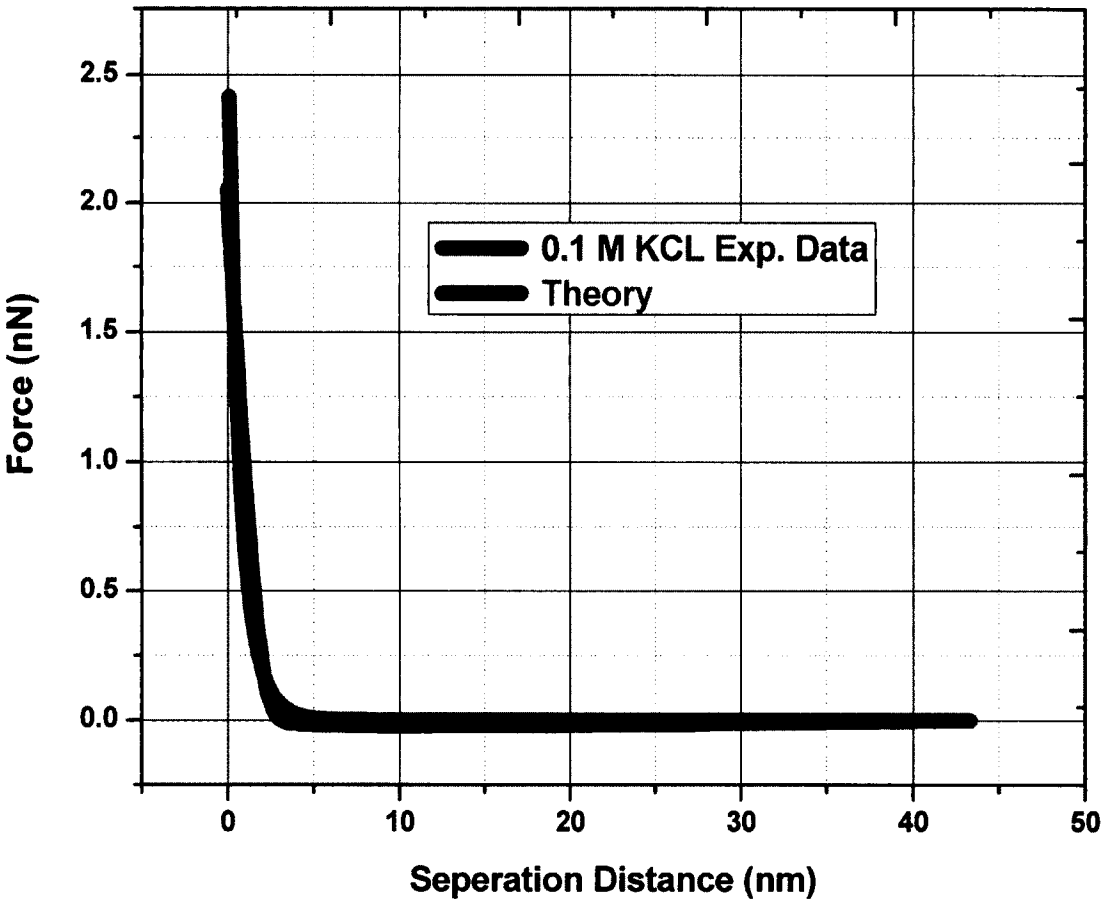

Figure 2.4: Force versus separation distance experimental curve fitted with theory in 0.1M KCL solution using colloid probe.

Table 2.1: Tip and silica surface charge density in different experiments at 0.1M KCL solution.

No of Experiments	Tip Surface Charge Density (C/m^2)	Silica Surface Charge Density (C/m^2)
1	-0.012455295	-0.012452229
2	-0.013318248	-0.013319725
3	-0.012796564	-0.012794662
4	-0.012917552	-0.012915556
Avg. (±SD)	-0.01287 (± 0.00036)	-0.01287 (± 0.00036)

In 0.01M KCL solution, interaction forces were measured between the AFM colloid tip and the silica surface. Figure 2.5 shows experimental results along with the DLVO theory fitted curves. The solid red line represents the theoretical results, and the solid blue line represents those of the experiment. The experiment curve shows a maximum force of about 3.75 nN when the probe reaches the sample surface. The double layer thickness is about 3.06 nm at 0.01 M KCL solution, and hence, the electrical double layer forces are experienced when the AFM tip and the substrate are about 6 nm apart. The AFM tip and silica surface densities are listed in table 2.2. The maximum tip surface charge density was -0.009114434 C/m^2 and the minimum was -0.007809534 C/m^2. The maximum silica surface charge density was -0.009114456 C/m^2 and the minimum value was -0.007808818 C/m^2. The average and SD of the tip and silica surface charge densities are -0.00861 (± 0.0007) C/m^2 and -0.00861 (± 0.0007) C/m^2, respectively.

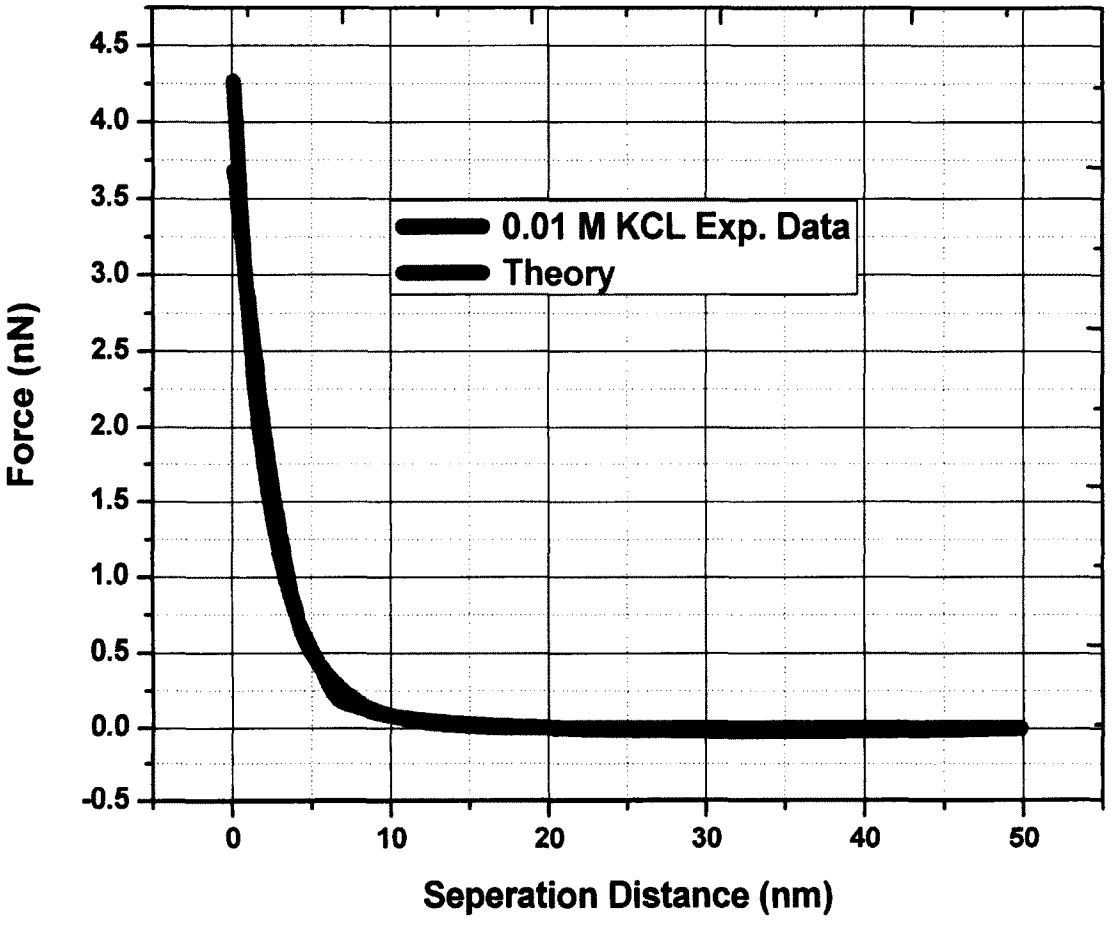

Figure 2.5: Force versus separation distance experimental curve fitted with theory in 0.01 M KCL solution using colloid probe.

Table 2.2: Tip and silica surface charge density in different experiments at 0.01M KCL solution.

No of Experiments	Tip Surface Charge Density (C/m^2)	Silica Surface Charge Density (C/m^2)
1	-0.009114434	-0.009114456
2	-0.008915695	-0.008915694
3	-0.007809534	-0.007808818
Avg. (±SD)	-0.00861 (± 0.0007)	-0.00861 (± 0.0007)

Figures 2.6 and 2.7 depict, respectively, the interaction force in 1 mM and 0.5 mM KCl solutions, and the estimated surface charge densities are shown in Tables 2.3 and 2.4. Obviously, as the salt concentration decreases, the EDL thickness increases, yielding more significant interaction. Figure 2.9 shows the interaction forces as a function of the separation distance at different KCl concentrations. As KCl concentration dercreases, EDL thickness increases, resulting in high interaction force at larger separation distances. Figure 2.10 shows the silica's surface charge density as a function of the ionic concentration. Under the considered conditions, the silica surface is negatively charged. As the salt concentration decreases, the magnitude of the surface charge density decreases. This observation qualitatively agrees with the predictions made by Atalay et al. [126].

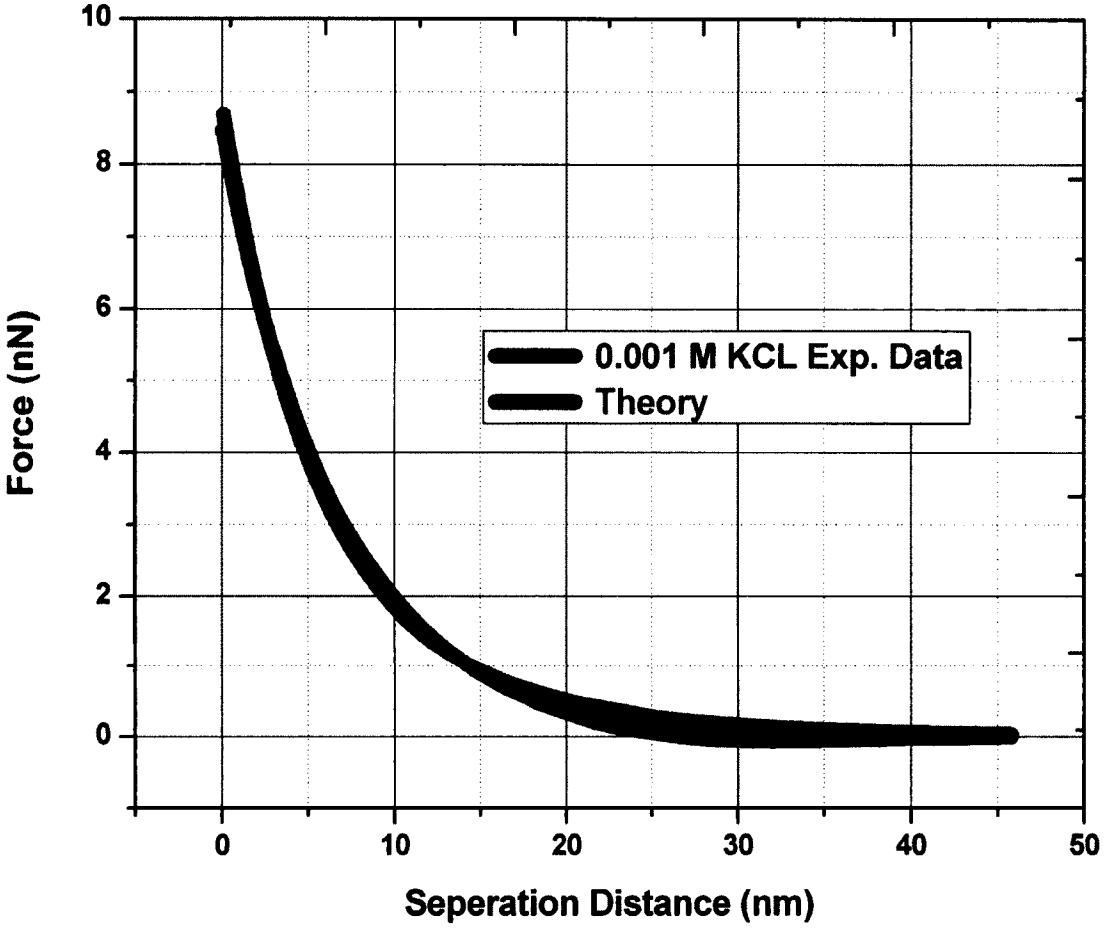

Figure 2.6: Force versus separation distance experimental curve fitted with theory in 0.001 M KCL solution using colloid probe.

Table 2.3: Tip and silica surface charge density in different experiments at 0.001M KCL solution.

No of Experiments	Tip Surface Charge Density (C/m^2)	Silica Surface Charge Density (C/m^2)
1	-0.010810789	-0.003574139
2	-0.00706371	-0.007064141
3	-0.006842919	-0.006843018
Avg. (±SD)	-0.00824 (± 0.00223)	-0.00583 (± 0.00195)

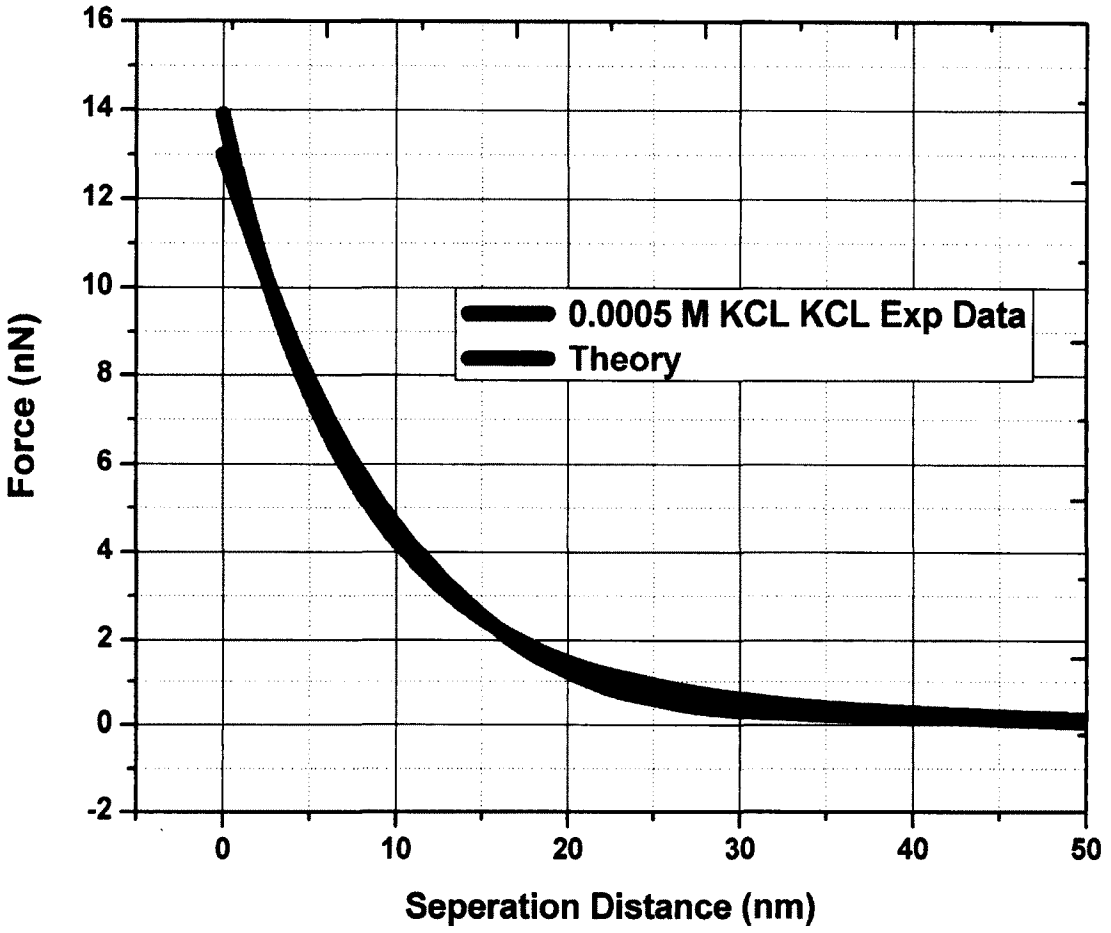

Figure 2.7: Force versus separation distance experimental curve fitted with theory in 0.0005 M KCL solution using colloid probe.

Table 2.4: Tip and silica surface charge density in different experiments at 0.0005M KCL solution.

No of Experiments	Tip Surface Charge Density (C/m^2)	Silica Surface Charge Density (C/m^2)
1	-0.013056099	-0.002430071
2	-0.012296685	-0.002906252
3	-0.014398812	-0.0011996
Avg. (±SD)	-0.01325 (± 0.00106)	-0.00218 (± 0.00088)

Figure 2.8 demonstrates curves of force versus separation distance fitted with theoretical curves in different KCL concentrations with the use of a colloidal probe. The KCL concentrations of 0.1, 0.01, 0.001 and 0.0005 M were matched with theoretical ones, and both agree. In higher concentrations, like 0.1 M KCL solution, the double layer thickness is 0.9 nm; as a result, electrostatic forces were experienced at about 2 nm apart and had shown a lower magnitude of force. On the other hand, at a lower concentration like 0.0005 M, the KCL concentration had a higher magnitude of force.

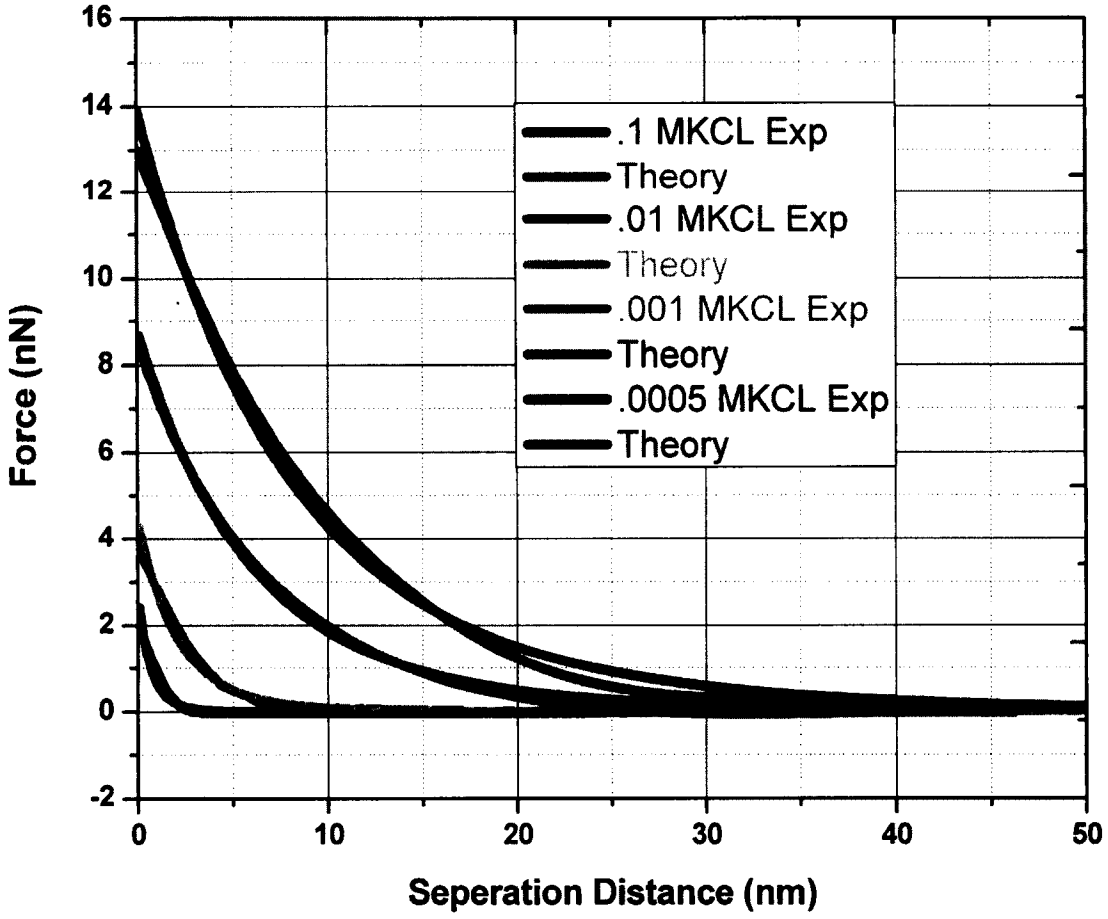

Figure 2.8: Four different KCL concentrations force versus separation distance experimental curve fitted with theory.

Figure 2.9 is of the silica surface charge density versus a differential ionic concentration curve. The lower ionic concentration predicted a lower amount of charge density. In the 0.005 M KCL solution, charge density is -0.00218 C/m^2. The charge density increased with increasing ionic concentration. At higher ionic concentrations, it exhibited a higher density whereas in the 0.1 M KCL concentration it showed that the silica surface density was -0.01287 C/m^2.

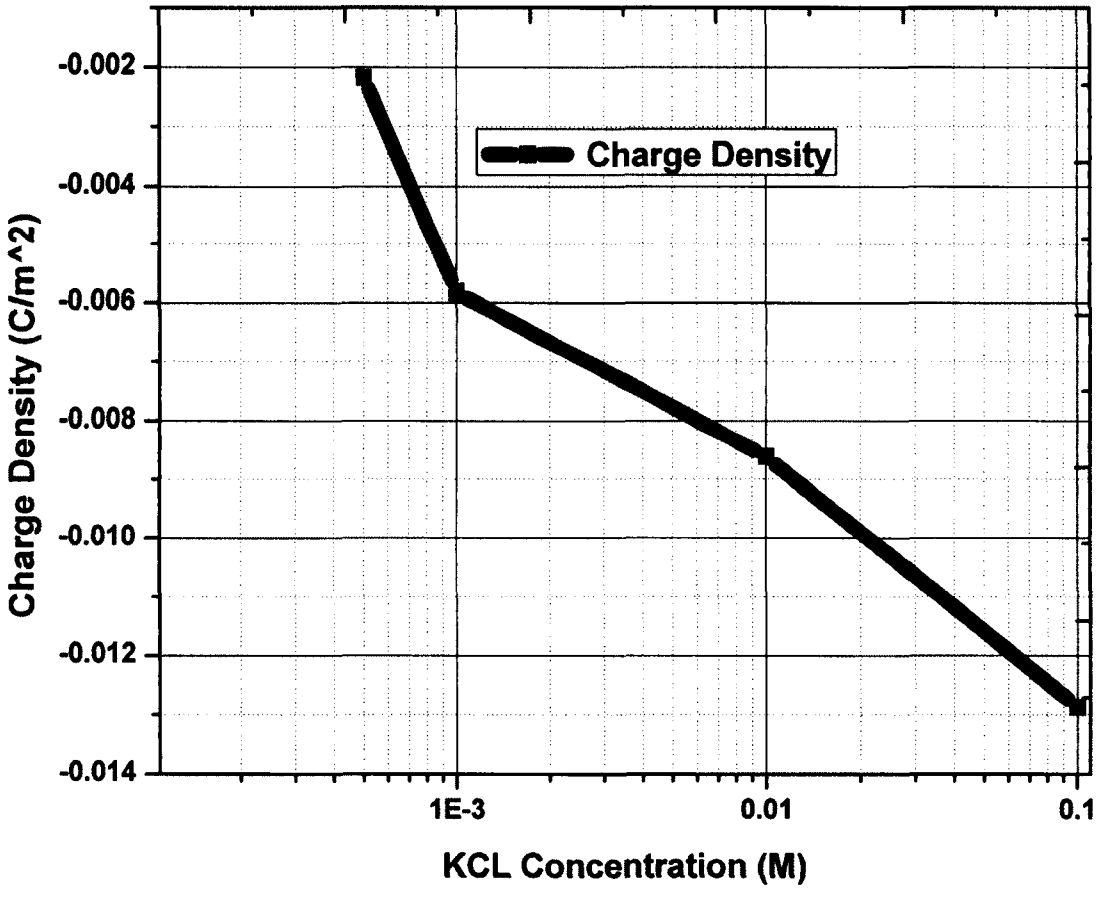

Figure 2.9: Charge density versus different KCL concentrations using colloid probe.

2.4.2 Force Measurements using Nano Probe

The AFM nano tip was made of quartz with the curvature radius of 10 nm. Figures 2.10-2.13 depict the interaction forces between the nano tip and flat silica surface at various KCl concentrations. The experimental force-separation distance curves are fitted with the DLVO theory with constant surface charge densities, and the estimated surface charge densities are shown in Tables 2.5-2.8. Figure 2.16 depicts the surface charge density of the silica flat surface as a function of the salt concentration. In Figure 2.16, the black line with squares represents the results obtained from the previous section using micron-sized AFM probe, while the blue line with squares represents the results obtained with the nano-sized AFM probe. Obviously, the magnitude of the surface charge density of silica's surface obtained with the nano-sized tip is higher than that obtained with the micron-sized AFM probe. Since silica surface is charge regulated, its charge properties depend on the local solution properties such as salt concentration and pH. The observations also qualitatively agree with the theoretical results obtained by Atalay et al. [126]. Results from both micron- and nano-sized probes show that the surface charge density increases as the salt concentration increases.

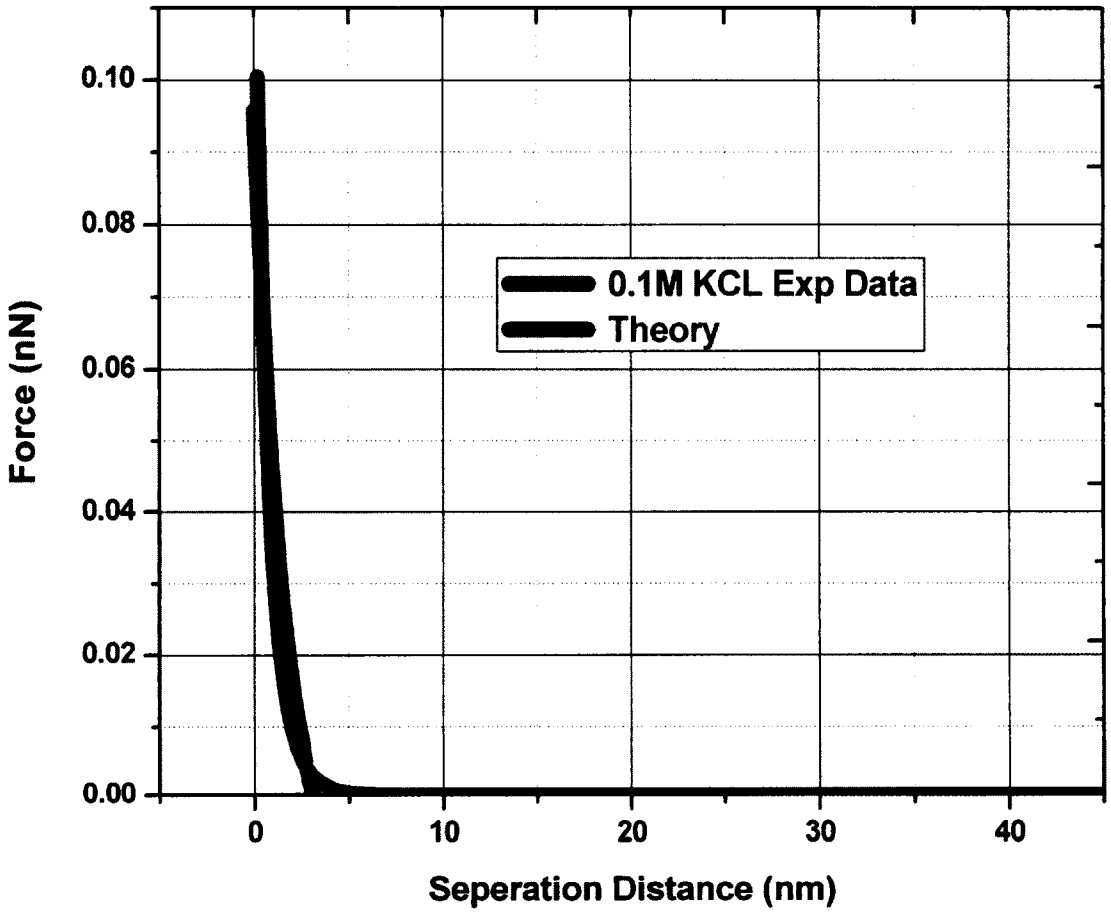

Figure 2.10: Force versus separation distance experimental curve fitted with theory in 0.1 M KCL solution using nano probe.

Table 2.5: Tip and silica surface charge density in different experiments at 0.1M KCL solution.

No of Experiments	surface Charge Density (C/m^2)	surface Charge Density (C/m^2)
1	-0.019262881	-0.01933123
2	-0.01989913	-0.019866338
3	-0.02020149	-0.020155317
Avg. (±SD)	-0.01979 (± 0.00048)	-0.01978 (± 0.00042)

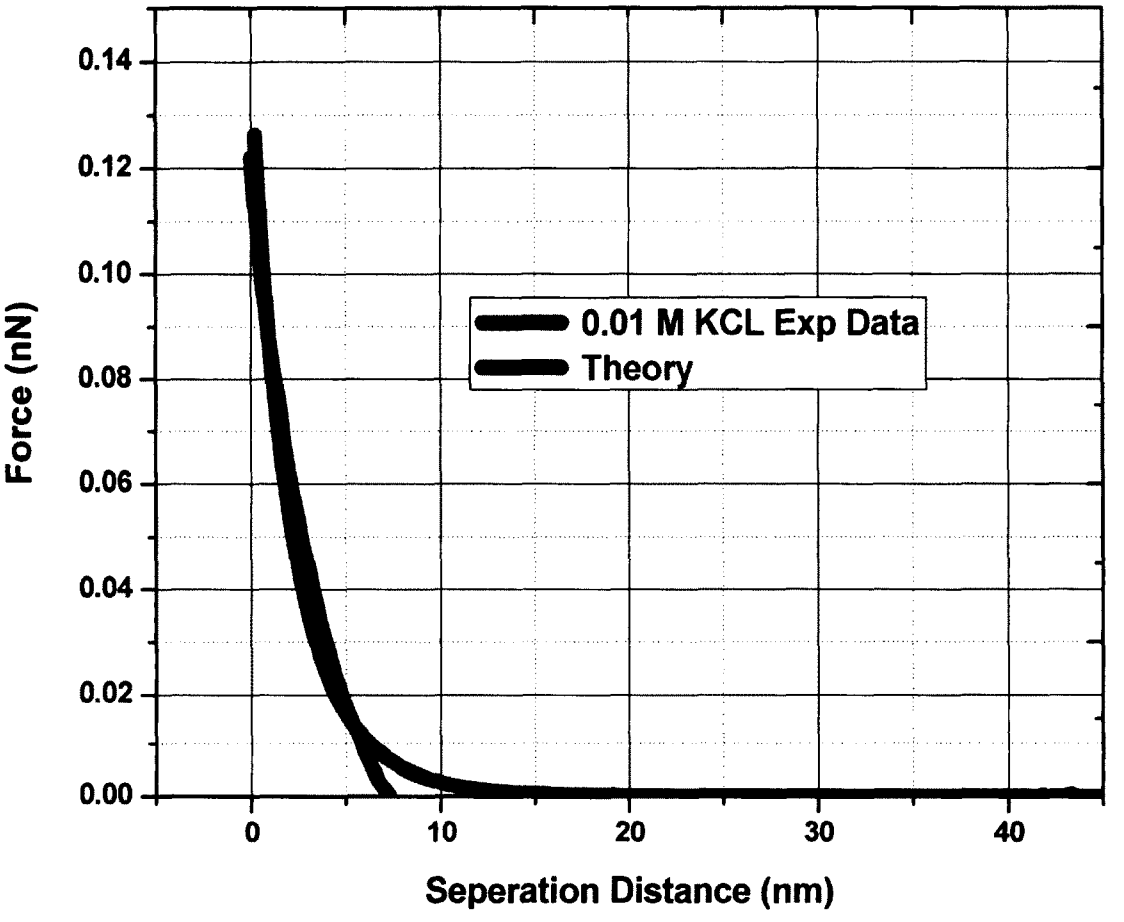

Figure 2.11: Force versus separation distance experimental curve fitted with theory in 0.01 M KCL solution using nano probe.

Table 2.6: Tip and silica surface charge density in different experiments at 0.01M KCL solution.

Experimental	Tip Surface Charge Density (C/m^2)	Silica Surface Charge Density (C/m^2)
1	-0.011619128	-0.011582201
2	-0.011872085	-0.011864888
3	-0.011486689	-0.011190537
4	-0.012213051	-0.01220581
Avg. (±SD)	-0.0118(± 0.00032)	-0.01171(± 0.00043)

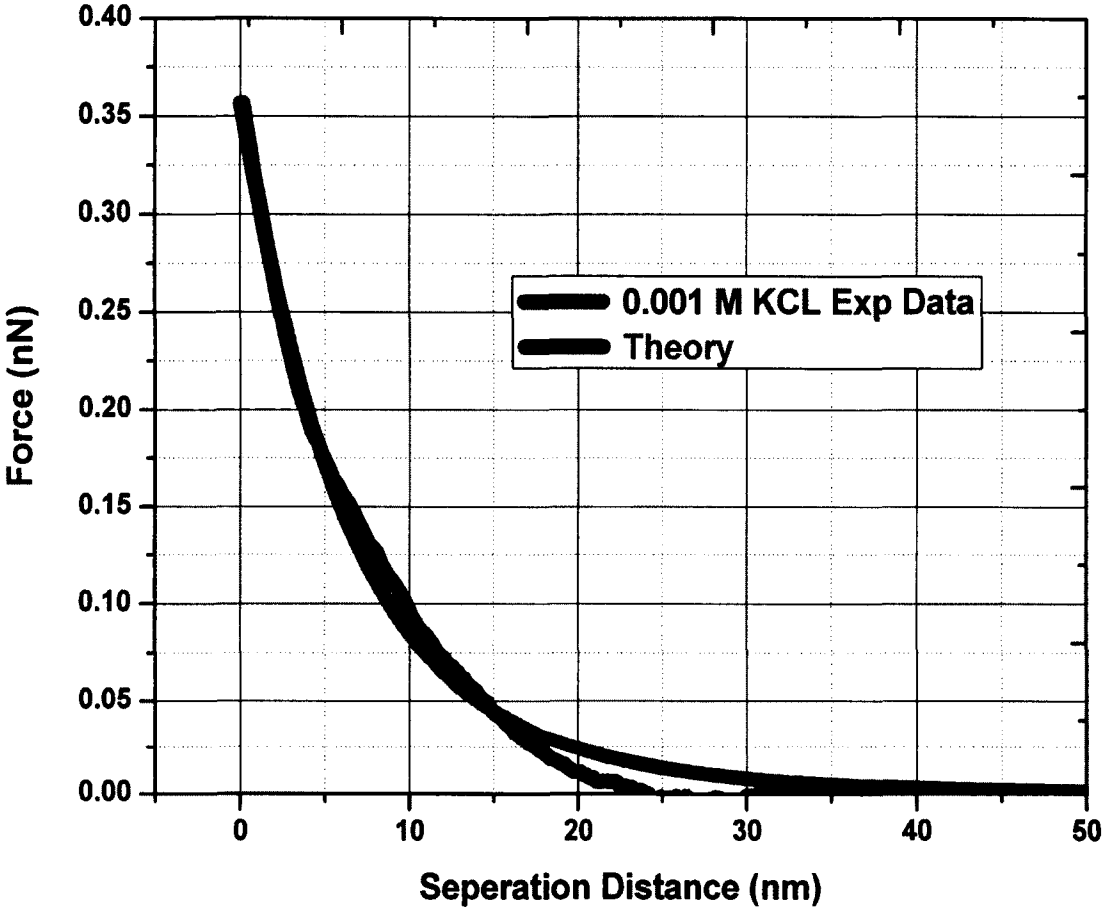

Figure 2.12: Force versus separation distance experimental curve fitted with theory in 0.001 M KCL solution using nano probe.

Table 2.7: Tip and silica surface charge density in different experiments at 0.001M KCL solution.

Experimental	Tip Surface Charge Density (C/m^2)	Silica Surface Charge Density (C/m^2)
1	-0.015386465	-0.005745121
2	-0.015462142	-0.004507068
3	-0.013071774	-0.007704033
Avg. (±SD)	-0.01464(± 0.00136)	-0.00599(± 0.00161)

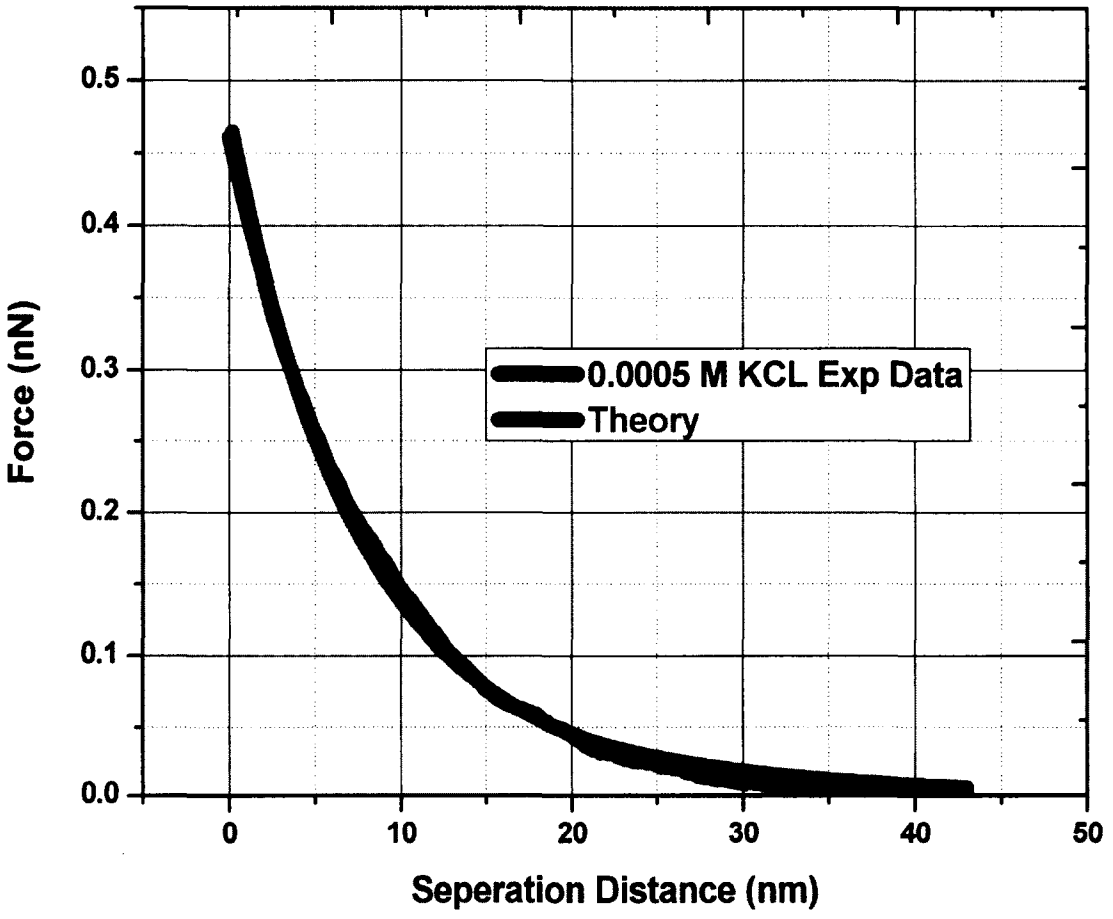

Figure 2.13: Force versus separation distance experimental curve fitted with theory in 0.0005 M KCL solution using nano probe.

Table 2.8: Tip and silica surface charge density in different experiments at 0.0005M KCL solution.

Experimental	Tip Surface Charge Density (C/m^2)	Silica Surface Charge Density (C/m^2)
1	-0.017078161	-0.002777057
2	-0.017313576	-0.001587851
3	-0.01575993	-0.003525419
Avg. (±SD)	-0.01672 (± 0.00084)	-0.00263(± 0.00098)

Figure 2.14 shows force versus separation distance curves fitted with theory in different KCL concentrations using the nano-probe as opposed to a colloidal probe. The KCL concentrations are 0.1, 0.01, 0.001 and 0.0005. In each condition, experimental curve was fitted with theory. Experimental curves were fitted with electrical double layer theory. All of the experimental curves have good agreement with theory. In higher concentration like 0.1 M KCL solution, double layer thickness is 0.9 nm; hence, electrostatic force were experienced about 2 nm apart, showing a lower magnitude of force. On the other hand, at lower concentrations like 0.0005 M KCL, concentration has higher magnitude of force.

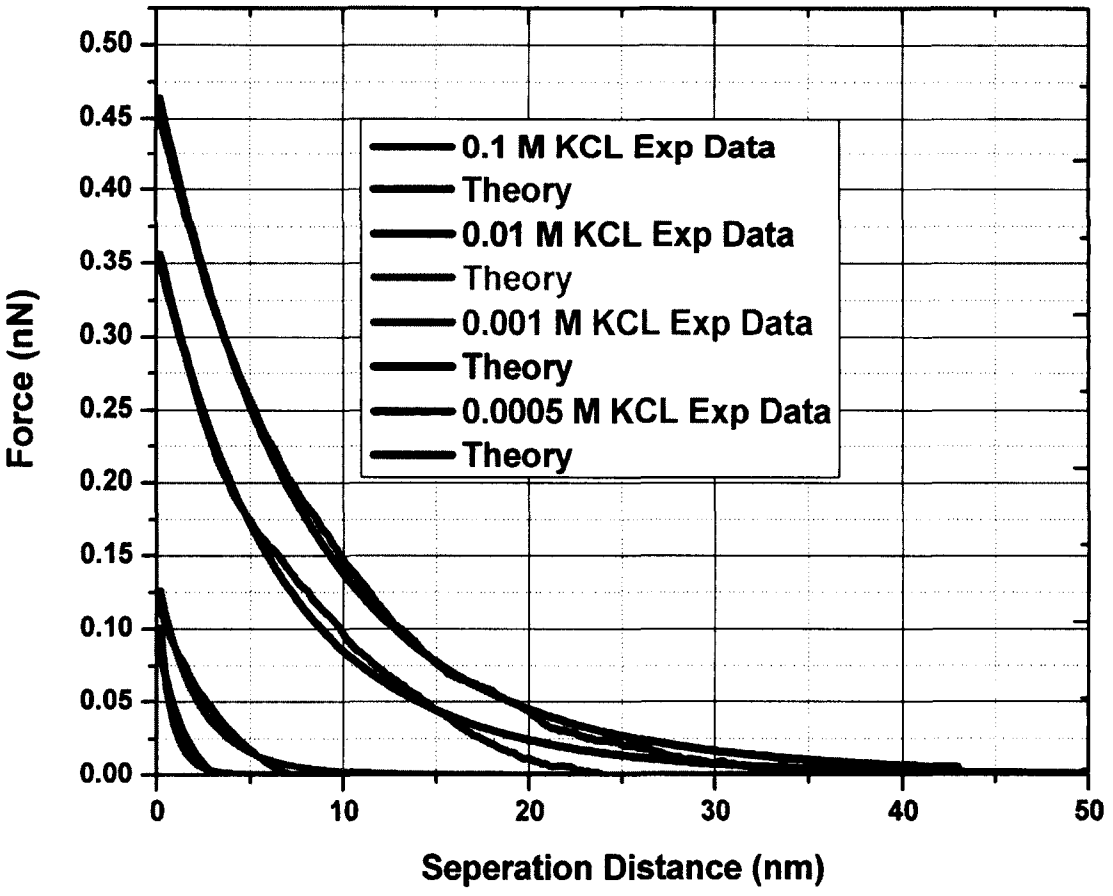

Figure 2.14: Force versus separation distance different experimental curves fitted with theory in different KCL solution using nano probe.

Figure 2.15 shows the silica surface charge density versus different ionic concentration curve. In the lower ionic concentration predicted lower amount of charge density. In the 0.005 M KCL solution, charge density is -0.00263 C/m^2. The charge density increased with increasing of ionic concentration; the density increased with the higher ionic concentration as well. 0.1 M KCL concentration shows silica surface density was -0.01978 C/m^2.

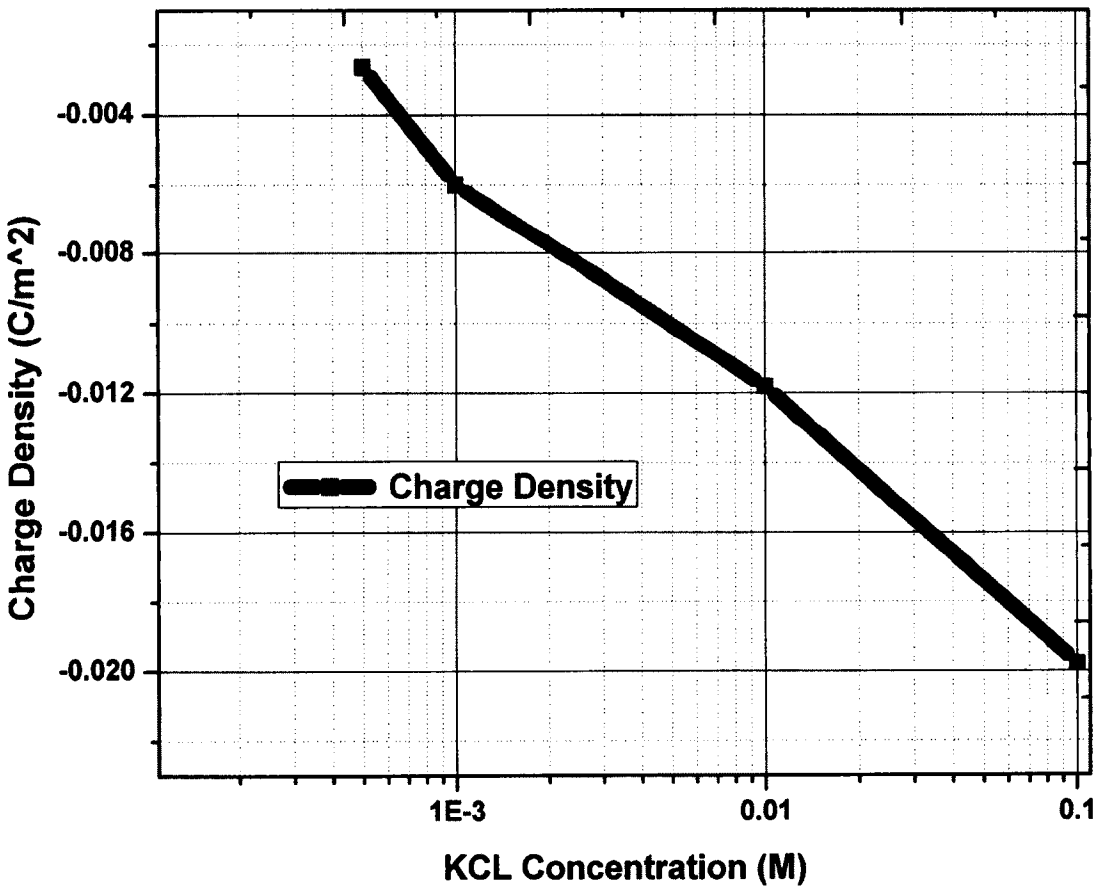

Figure 2.15: Charge density versus different KCL concentrations using nano probe.

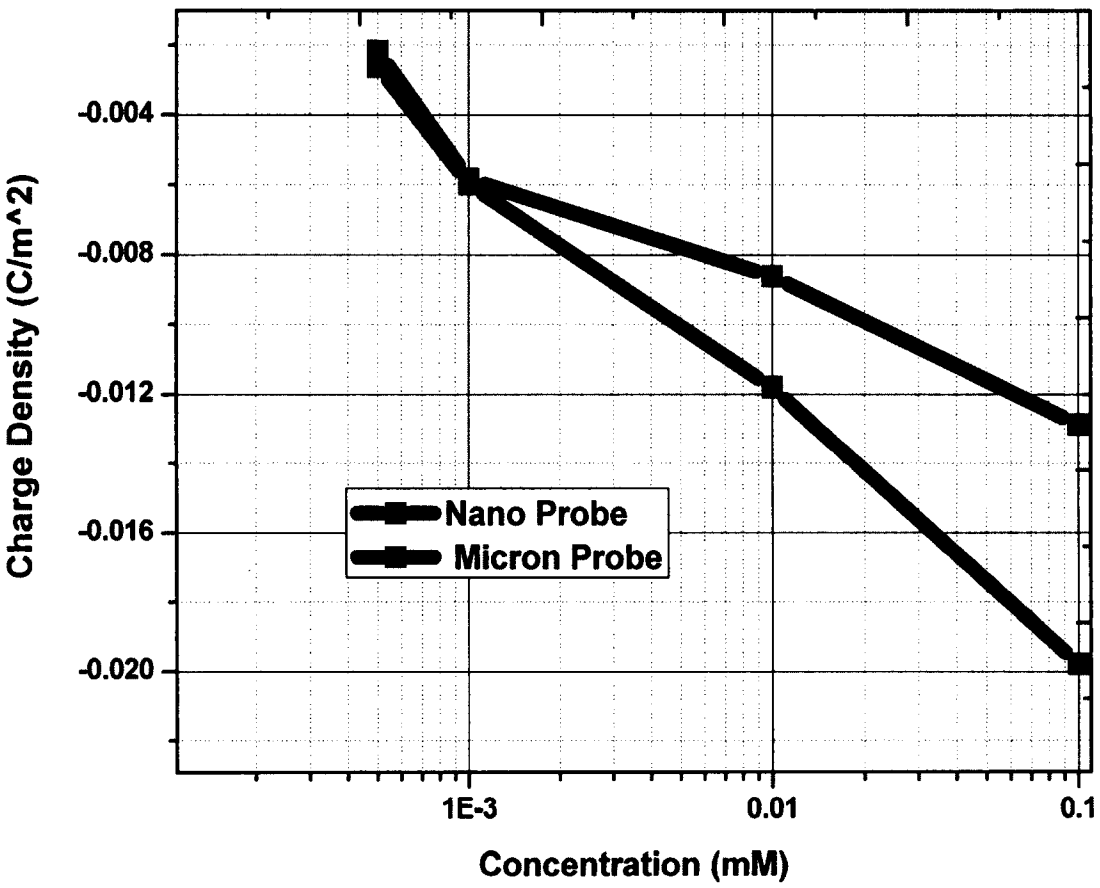

Figure 2.16: Comparison between nano probe and micron probe surface charge density mapping above the silicon wafer in different ionic concentrations.

Figure 2.16 shows charge density measurements in different ionic concentrations using different sizes of AFM probe. It also shows how charge density varies within ionic concentrations. Both micron and nano size probe charge density increased with increasing of ionic concentrations. The qualitative increase of charge density with higher ionic concentrations agrees with theoretical results got by Atalay et al. [126].

2.4.3 Van der Waals Forces in DI water

AFM experiments were carried out in DI water by using the nano-sized AFM probe with radius of curvature about 10 nm to measure the Van der Waals force. Figure 2.17 shows the force versus the separation distance in DI water, and attractive Van der Waals force is observed when the separation distance between the tip and the flat silica surface is very close. The measured force is fitted by the Van der Waals theory (symbols in Figure 2.17) to estimate the Hamaker constant. Based on the fit of the last part of the force curves, the estimated Hamaker constant is $A= 1.99 \times 10^{-19}$J. Hu et al. [127] investigated Van der Waals force measurements between silica and gold surface in DI water, and their Hamaker constant is $A= 1.6 \times 10^{-19}$J, which is close to our result.

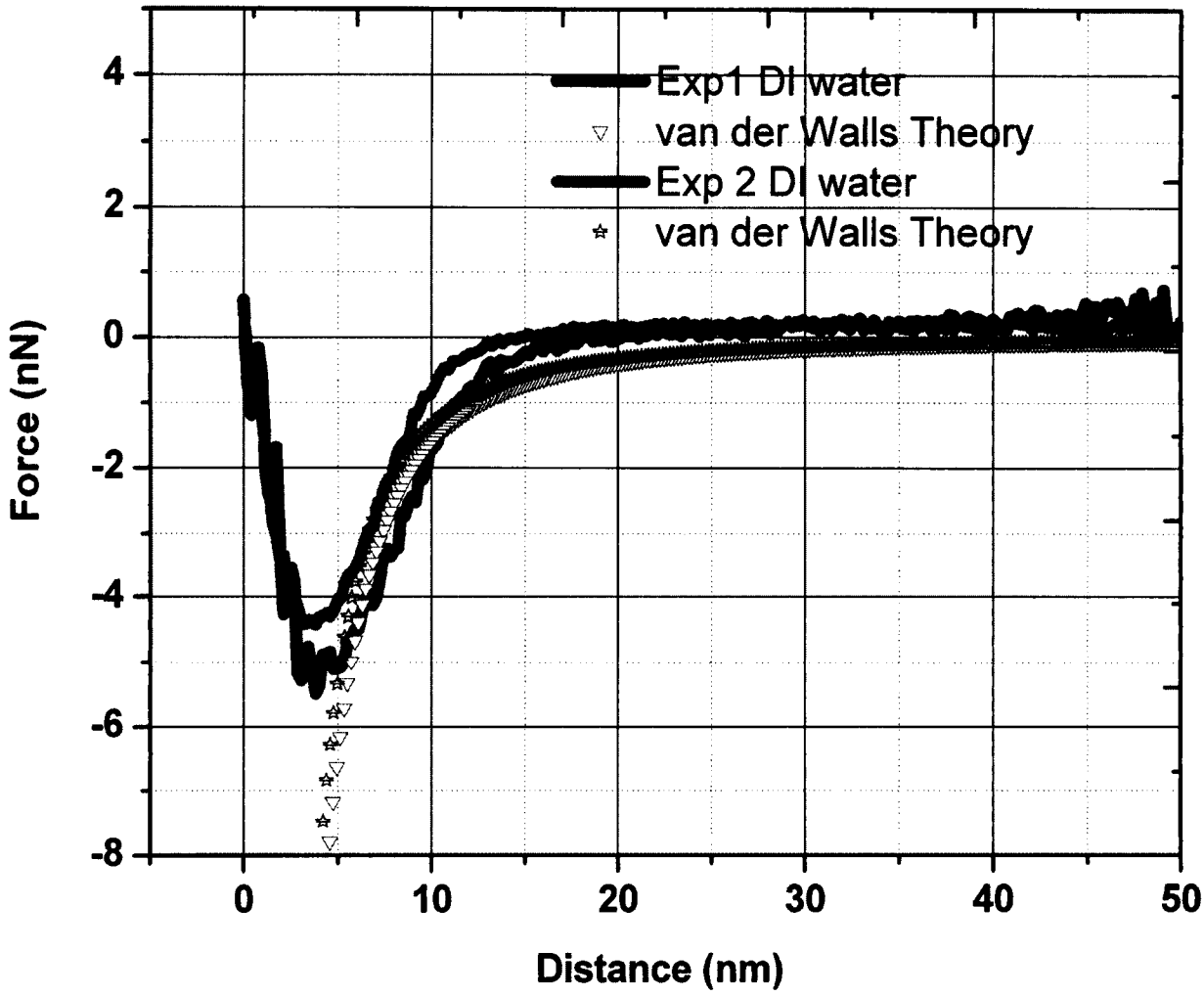

Figure 2.17: Force versus distance curves in DI water and fit based on the Van der Waals theory.

2.5 Conclusions

In this chapter the Van der Waals force between the AFM probe and silica surface in DI water was measured and fitted to estimate the Hamaker constant. The interaction forces between the AFM probe made of silica and silica surface in various KCl solutions were systematically measured using both micron- and nano-sized AFM probes. The measured force-distance curves were fitted with the DLVO theory with constant surface charge densities on the interacting objects. In general, the DLVO theory fits very well with the measured forces under various conditions. The obtained surface charge density increases as the salt concentration increases. In addition, the surface charge density of the silica surface obtained from the nano-sized AFM probe is higher than that from the micron-sized probe under the other same conditions. The obtained experimental results qualitatively agree with the theoretical predictions obtained from our group. The results clearly show that silica is charge-regulated and its charge properties depend on the local solution properties, which depend on pH, salt concentration, and nearby interacting objects.

CHAPTER 3

NANO-MECHANICS OF POLYMERIC MATERIALS AND COLLAGEN NANOSTRAWS

3.1 Introduction

Atomic Force Microscopy (AFM) has been used to study multiple types of materials using imaging and force measurements with atomic scale resolution [128-129]. This is invaluable, especially with regards to characterization of polymeric and biological materials [130-144]. AFM was used to image Cartilages at nano scale and nano mechanical properties were measured [145-158]. In this chapter, we describe different nano-indentation theories and contact mechanics models as they apply to measuring the bio-physical properties of 'nanostraws' of collagen. Samples of costal cartilage exposed to six different types of treatment were extracted and then brought to the lab for preparation before testing. The collagen fibrils were imaged in both air and buffer solutions at nanometer resolution and their nano-mechanics were measured using an AFM nano-indenter.

Costal cartilage is the bridge between bony ribs and the sternum. A clear example can be found in Pectus Excavatum (PE), a disease characterized by a deformity in the chest wall which causes the chest to appear caved in. This condition typically increases in severity in adolescent years and beyond, where it can impair cardiac and respiratory functions, also affecting one's back if pronounced enough. Nearly 1 in 400 possesses some form of a pectus deformity and their symptoms can worsen with aging. Collagen is a protein that

is one of the principle components of connective tissues within the body; it gives strength and structural support for connective tissues within their extracellular matrices. Different tissues have different diameters of collagen fibrils, ranging from nanometers to micrometers. Collagen is worth studying to give insight to diseases that affect connective tissues. Knowing collagen mechanics can help the treatment of the diseases that affect it. Another protein found in the extra-cellular matrix is elastin; it is the component which gives elasticity to the skin and tissues of the cardiopulmonary system. Both of these proteins play a large part in the mechanics of cartilage, especially costal cartilage which we would like to study specifically. It bridges the bones between the ribs and sternum, protecting vital parts as well. Our research can help address the gap in knowledge that exists towards a nano-scale characterization of the fibers that support the tissue.

3.2 Materials

3.2.1 Sample Preparation

Human costal cartilage samples were received from patients at the Children's Hospital of the King's Daughter, Norfolk, VA, USA. The samples were removed surgically and treated according to an IRB approved protocol at Eastern Virginia Medical School and Old Dominion University. They were stored in a -80^0C freezer and mounted in CRYO-OCT Compound (Tissue-Tek, CA, USA) [30]. With the aid of a Micron HM525 cryostat, the samples were cut into 5, 10 and 20 micron slices. Sample slices were then attached to coverslips using a COL2A1 mouse monoclonal antibody (sc-52658, Santa Cruz, CA) and then fixed on cover slips with ice-cold acetone. Optical microscopy with a CCD camera was used to image the samples. Analysis of the samples was accomplished through the use of Image J.

3.2.2 Atomic Force Microscopy

A Nanonics Multiview-4000 multi-probe AFM with a lock in amplifier and data acquisition were used for all AFM experiments. Throughout the experimental work, AFM nano-probes made of quartz were used for topography imaging and nano-indentation. These AFM probes' radius of curvature varies from 10 nm to 200 nm (Nanonics, Israel). The AFM operation modes available were the static and tapping modes. However, all of our experimental work was carried out using the tapping mode. Topography image calibration was done with a micro-fabricated silicon grid. Before imaging any samples, I worked on a silicon grid which has a standard size and shape for comparison. The silicon grid's AFM image and profile are shown in Figures 2.1 and 2.2. Their dimensions were calibrated and matched with the manufacturer's dimensions. All AFM images were acquired with NWS and filtered with WSxM software. I also performed nano-indentation of PDMS at different indentation depths and obtained modulus of elasticity values which matched with comparable literature values [161]. I used the frequency modulation dynamic mode for force measurements. All of the collected force data from the experiments was post-processed based on frequency modulation force spectroscopy [162].

3.3 Results: Images of Human Costal Cartilage using AFM

Frozen costal cartilage was fixed in CRYO-OCT and a micron blade was used to cut from it slices of width from 5 to 20μm. These small samples were attached to cover slips coated with poly L-lysine. Ice-cold acetone was used to fix the samples while dry so they would not move during the AFM measurements. All AFM images were taken in air. We had more than ten samples and scanned these samples in various places, with the scan

size varying with time. Figure 3.1 shows undigested and fixed costal cartilage via AFM imaging; the right side contains the height bar of the topography image. Nano-straws were not found everywhere within the samples, and wherever they were found, they were oriented in different positions.

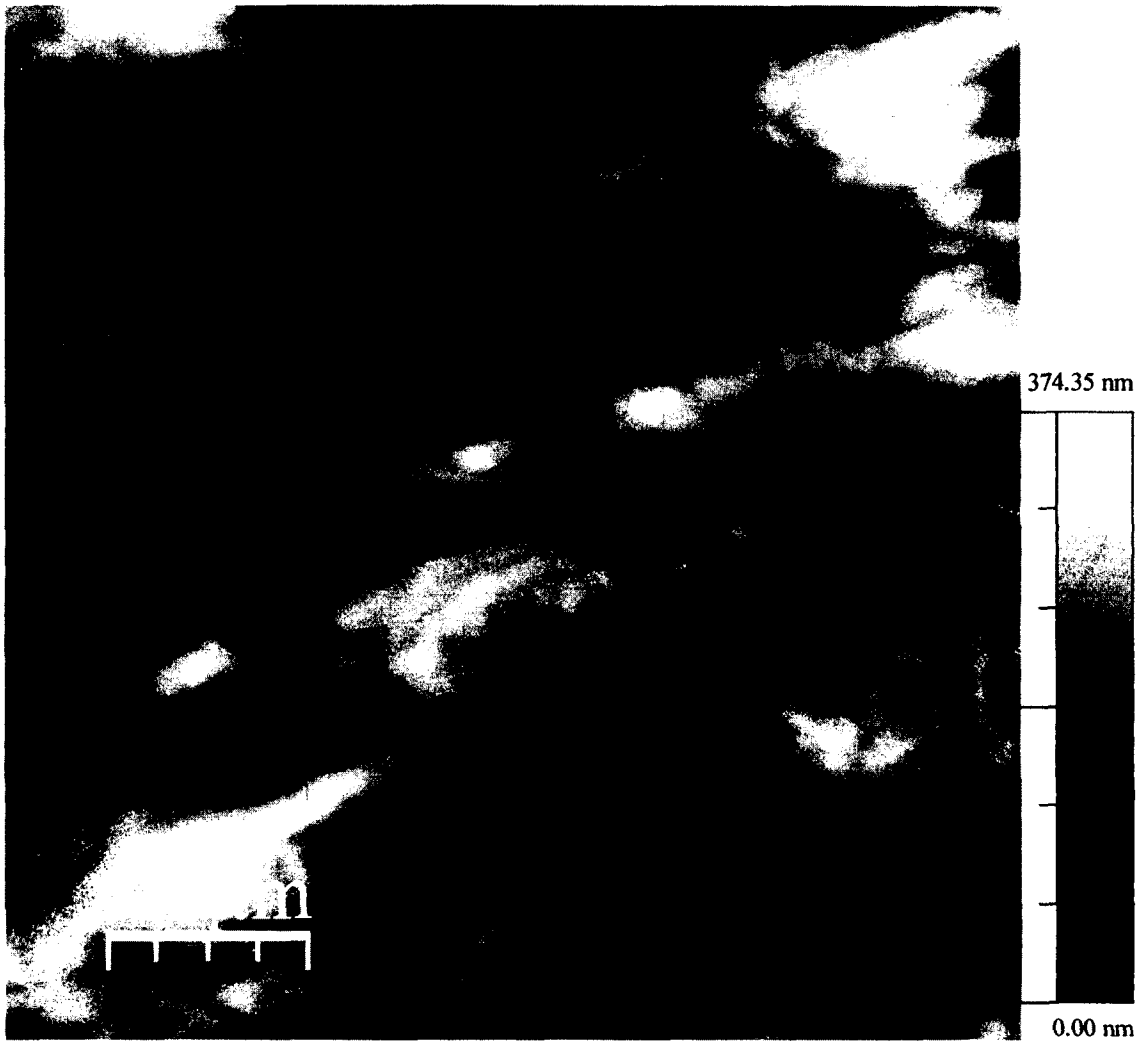

Figure 3.1: 15 x 15 μm AFM height image with scale bar of undigested and non-homogenized costal cartilage.

In Figure 3.2 is an optical microscopy image taken in air of a sample of undigested and fixed costal cartilage. This image was taken while the AFM was scanning - i.e., while the

AFM probe oscillated above the sample surface. The red box within outlines the area where the AFM probe scanned. In this figure, we can see round shape chondrocytes with sizes of about 15 micron and also noncollagenous proteins.

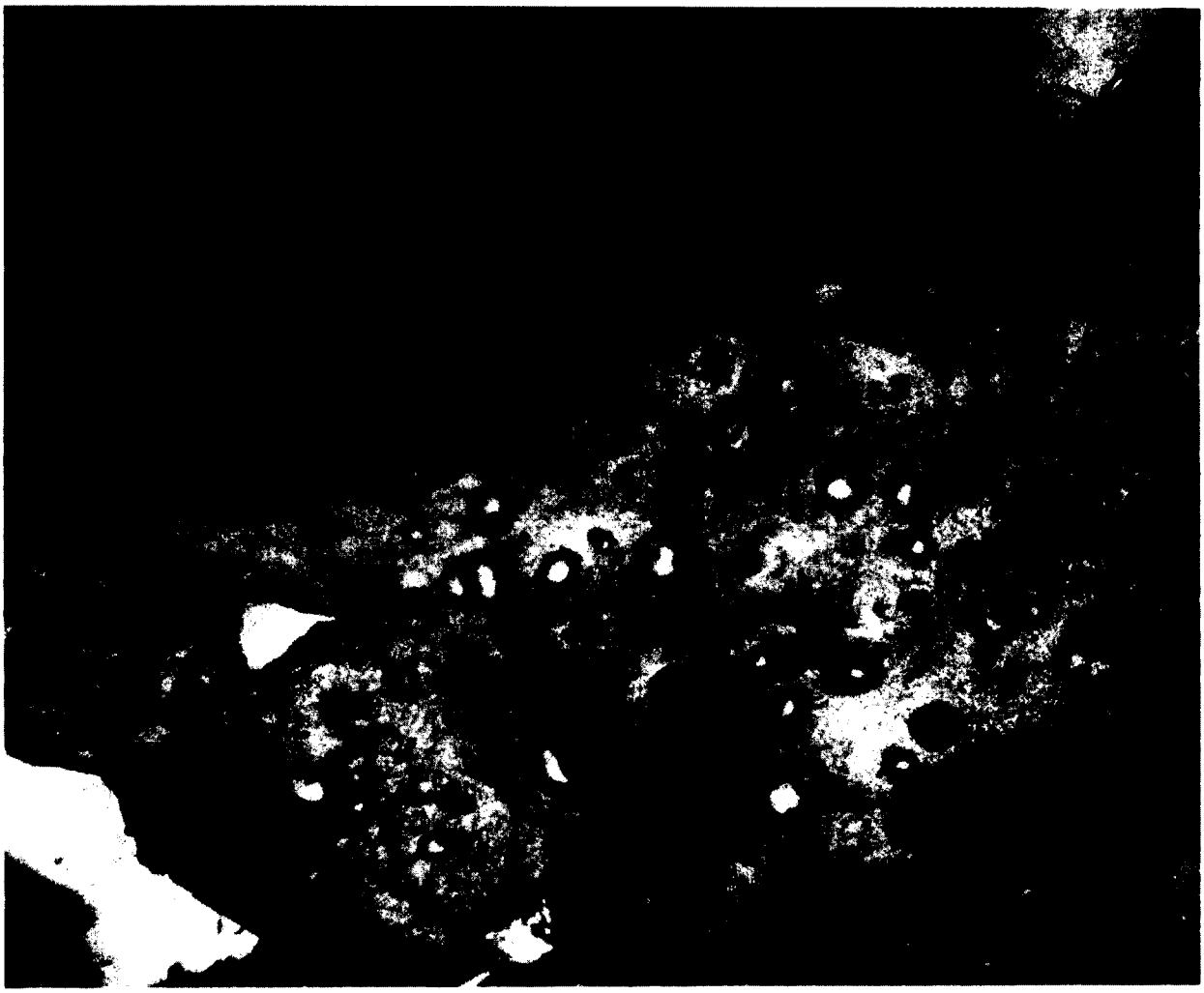

Figure 3.2: An optical microscopy image taken in air of a sample of undigested and fixed costal cartilage.

From all of the AFM topography images, we measured the width of 74 nano-straws. The mean value of the width of these straws is 435 nm, and the standard deviation is 64 nm as shown in Figure 3.3.

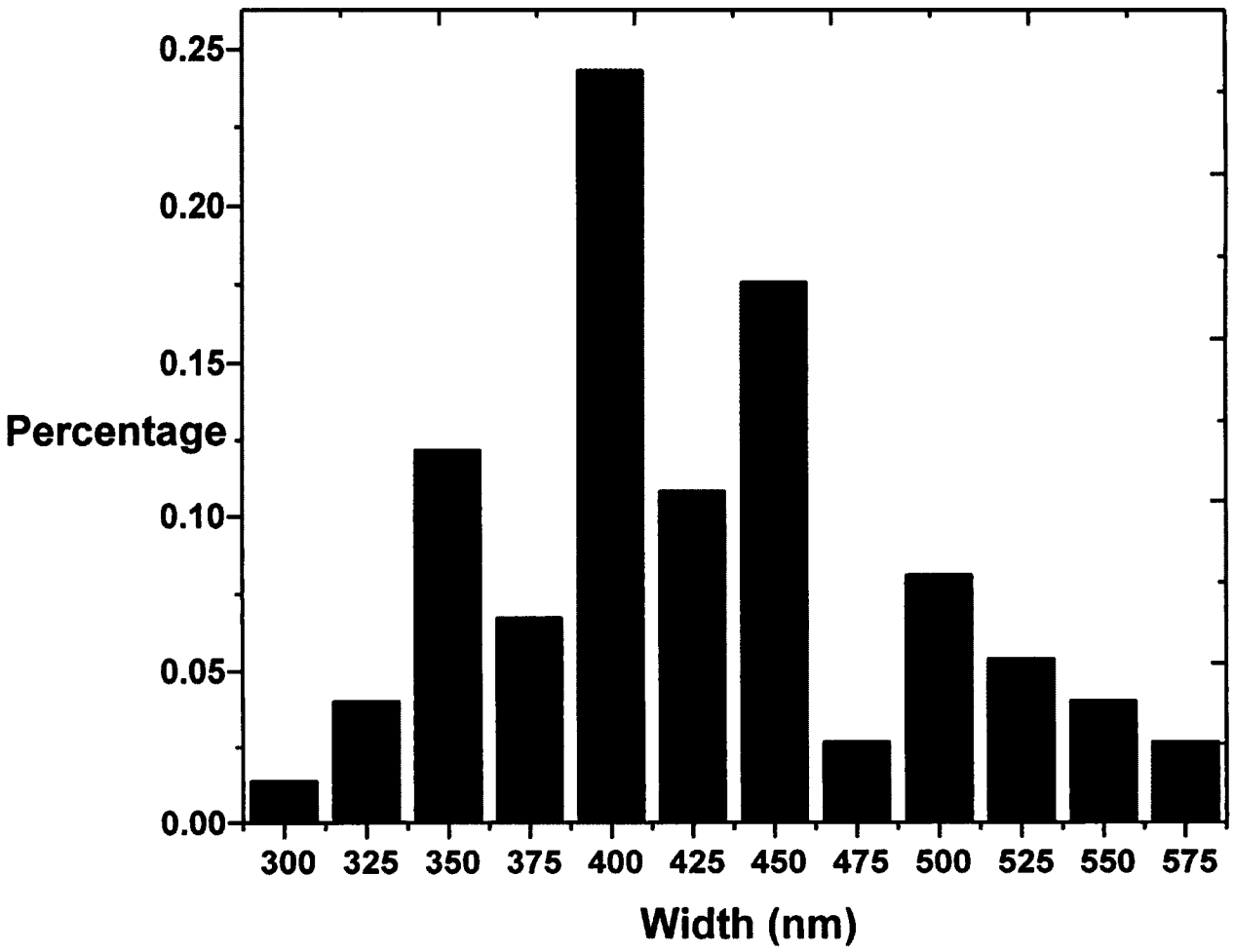

Figure 3.3: Width distribution of non-digested and non-homogenized fixed nano-straws.

Figure 3.4 shows a 10 x 10 μm area AFM topographical image of digested and fixed costal cartilage taken in air. These thin biological samples were digested with 0.1 mg/ml hyaluronidase and 0.1 mg/ml trypsin in buffer at 37^0 C for 48 hours [30]. The digestion process released nano-straws from the surrounding extracellular matrix components. In comparison, the nano-straws can be clearly seen in Figure 3.4 while they are not as clear

as in Figure 3.1. The right hand side of Figure 3.4 includes the height bar of the digested nano-straws.

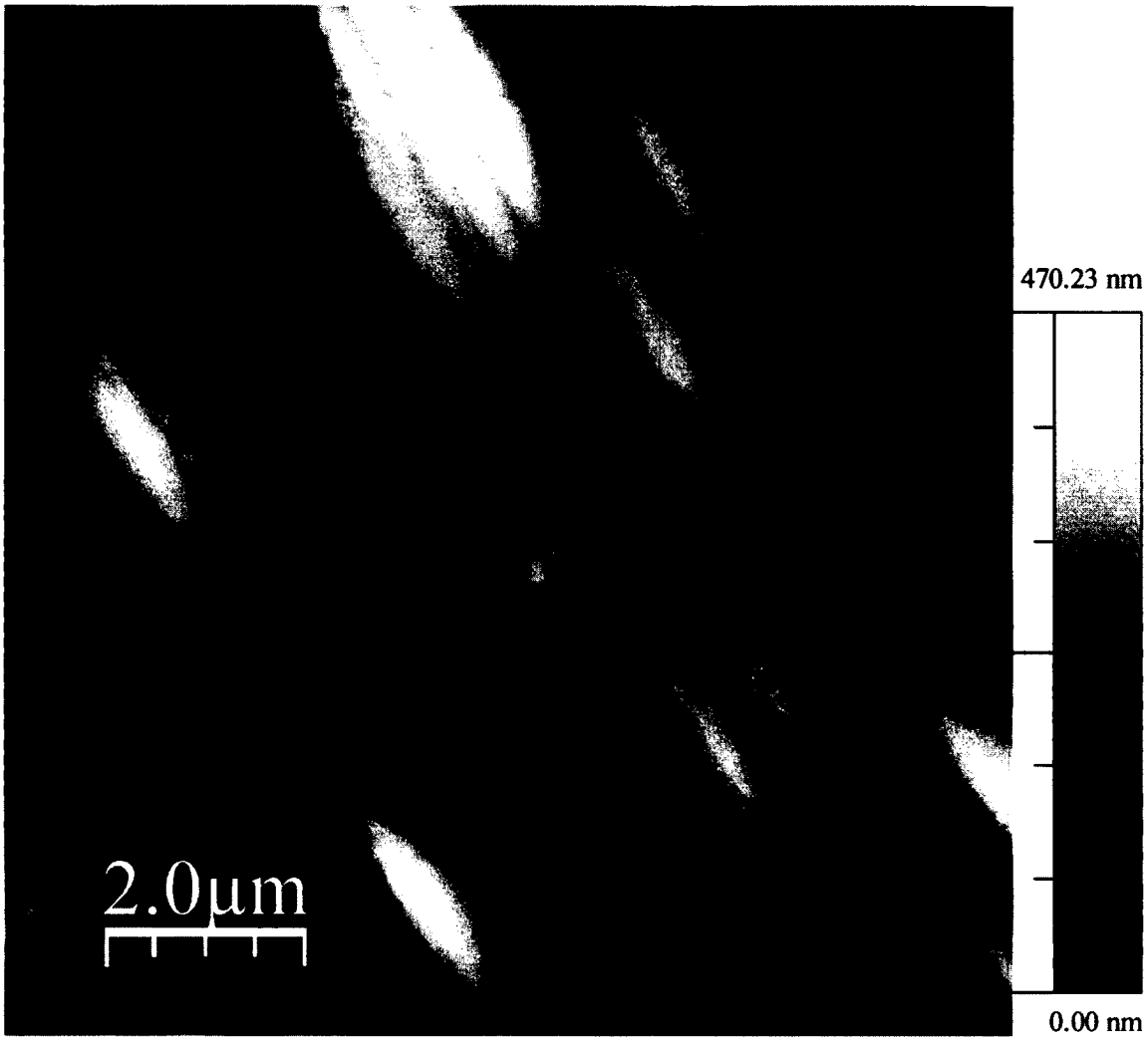

Figure 3.4: 10 x 10 μm AFM height image of digested and fixed costal cartilage taken in air.

Figure 3.5 is of another optical image taken in air during AFM scanning, but of digested and fixed costal cartilage. In the pink box in Figure 3.5, the place where AFM scanning had taken place is shown. In this figure, we can still see the round shape chondrocytes, but with the absence of the proteoglycans due to the chemical digestion process, the

image became more clear.

Figure 3.5: Optical microscopy image of digested and fixed costal cartilage.

Figure 3.6 gives us the nano-straw width distribution for the digested and fixed samples. 61 nano-straws' widths were measured. The mean value is 463 nm, and the standard

deviation is 82 nm.

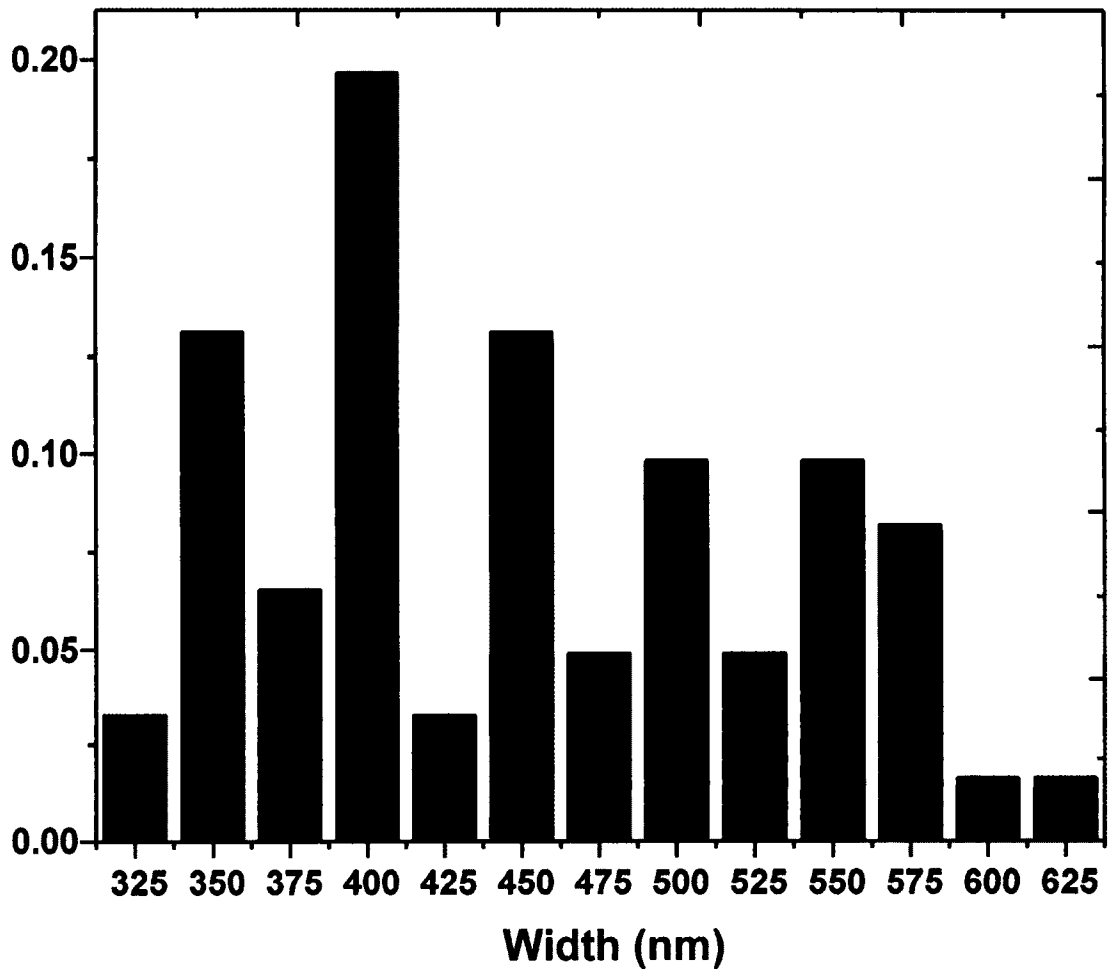

Figure 3.6: Width distribution of digested and fixed samples nano-straws.

Figure 3.7 shows fixed, homogenized and digested costal cartilage AFM topography images. With this sample, the nano-straws were released and are easier to see. A Fisher Power-Gen 35 micro homogenizer was used to blend the thin section of tissues [30]. Digestion was performed with 1 mg/ml hyaluronidase and 1 mg/ml trypsin in Sorenson's buffer at 37° C for 48 hours [30]. Figure 3.7's right hand side shows the height bar. From the AFM images, we can observe that the AFM image resolution is less than 1 nm.

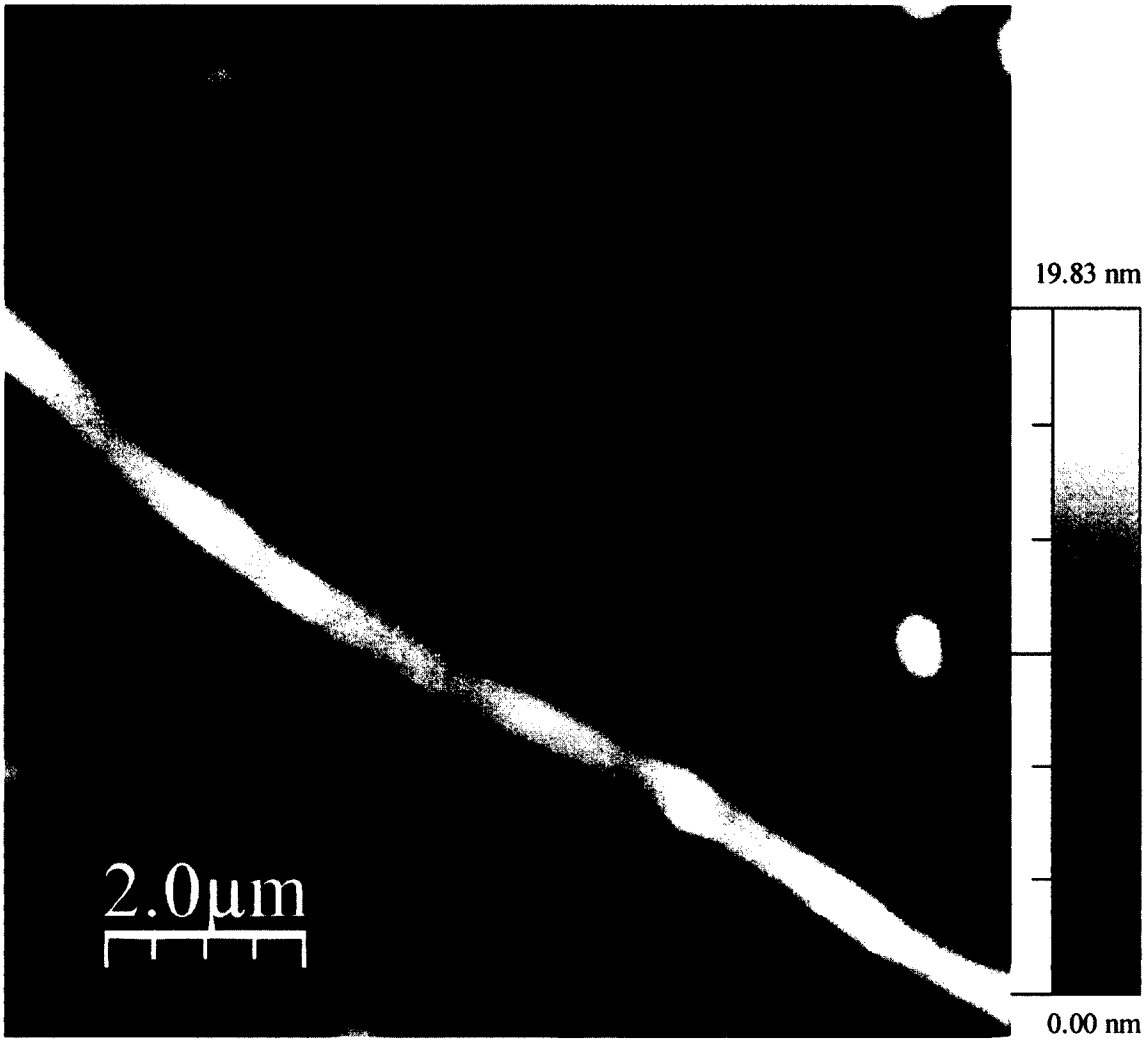

Figure 3.7: 10 x 10 μm AFM height image of homogenized and digested costal cartilage.

Figure 3.8 shows the width distribution of digested and homogenized nano-straws. The widths of 61 nano-straws were measured. The width mean value is 524 nm and the standard deviation is 130 nm. Among the 6 different samples, this sample shows the

largest width.

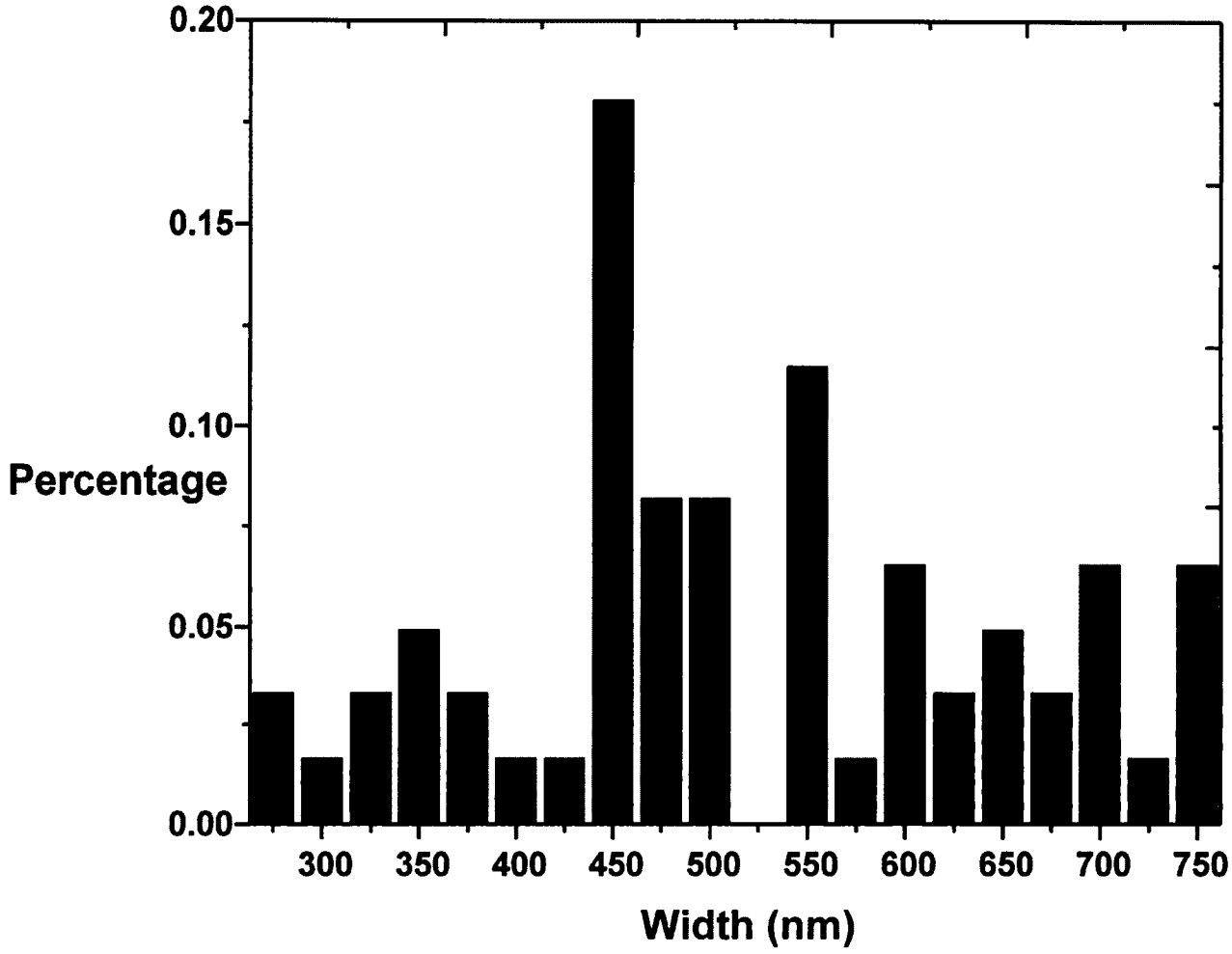

Figure 3.8: Width distribution of digested and homogenized nano-straws.

Figure 3.9 shows a 7.9 x 11.4 μm AFM image of homogenized and digested costal cartilage without fixation. The chemical treatments were performed as in the previous section. Scanning was performed in multiple areas. The height bar is to the right of the AFM image.

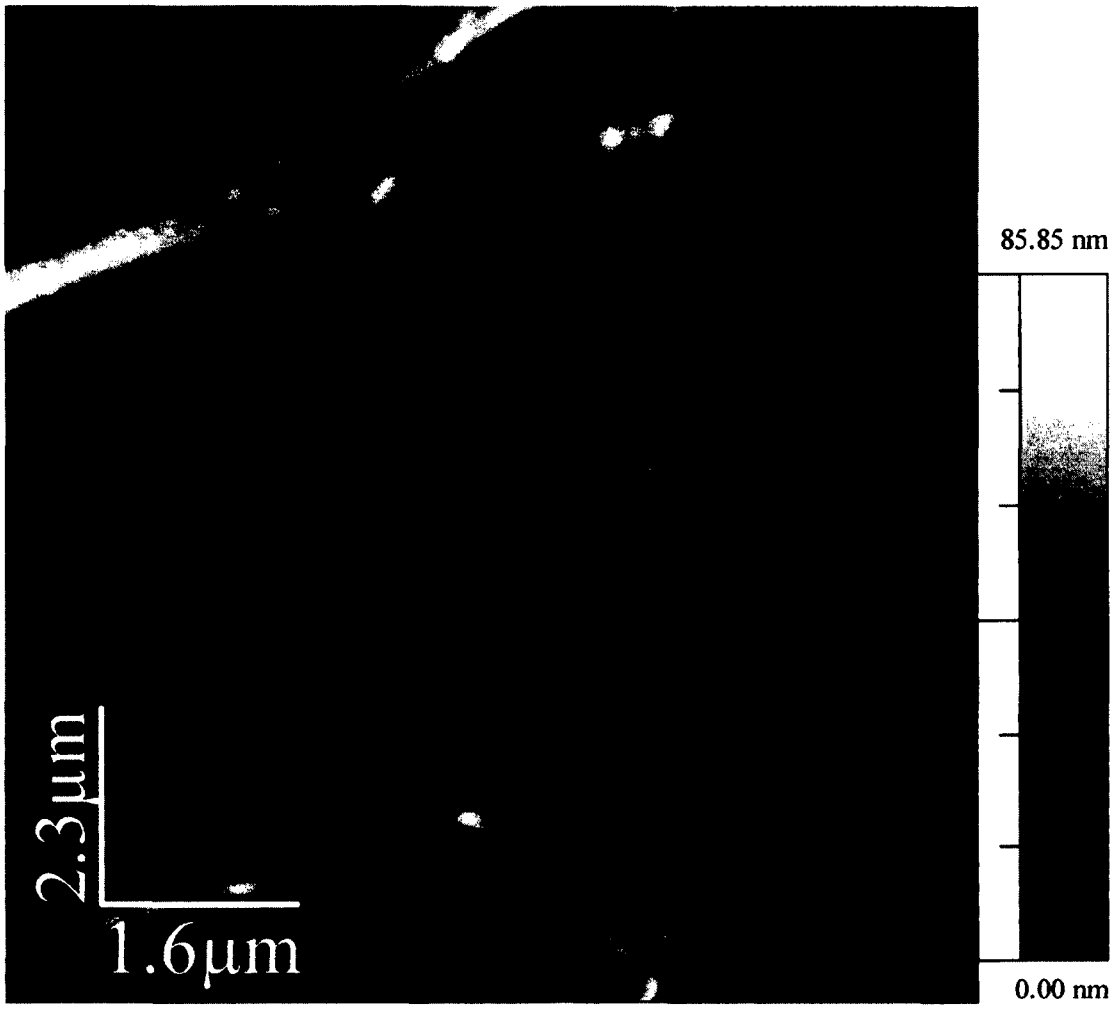

Figure 3.9: AFM height image of homogenized and digested costal cartilage without fixation.

Figure 3.10 presents the width distribution of digested, homogenized & unfixed nano-straws. Fifty eight nano-straws' widths were measured; there was a significant difference in the mean values between fixed and unfixed homogenized and digested samples. For unfixed samples, the mean value is 361 nm, and the standard deviation is 134.

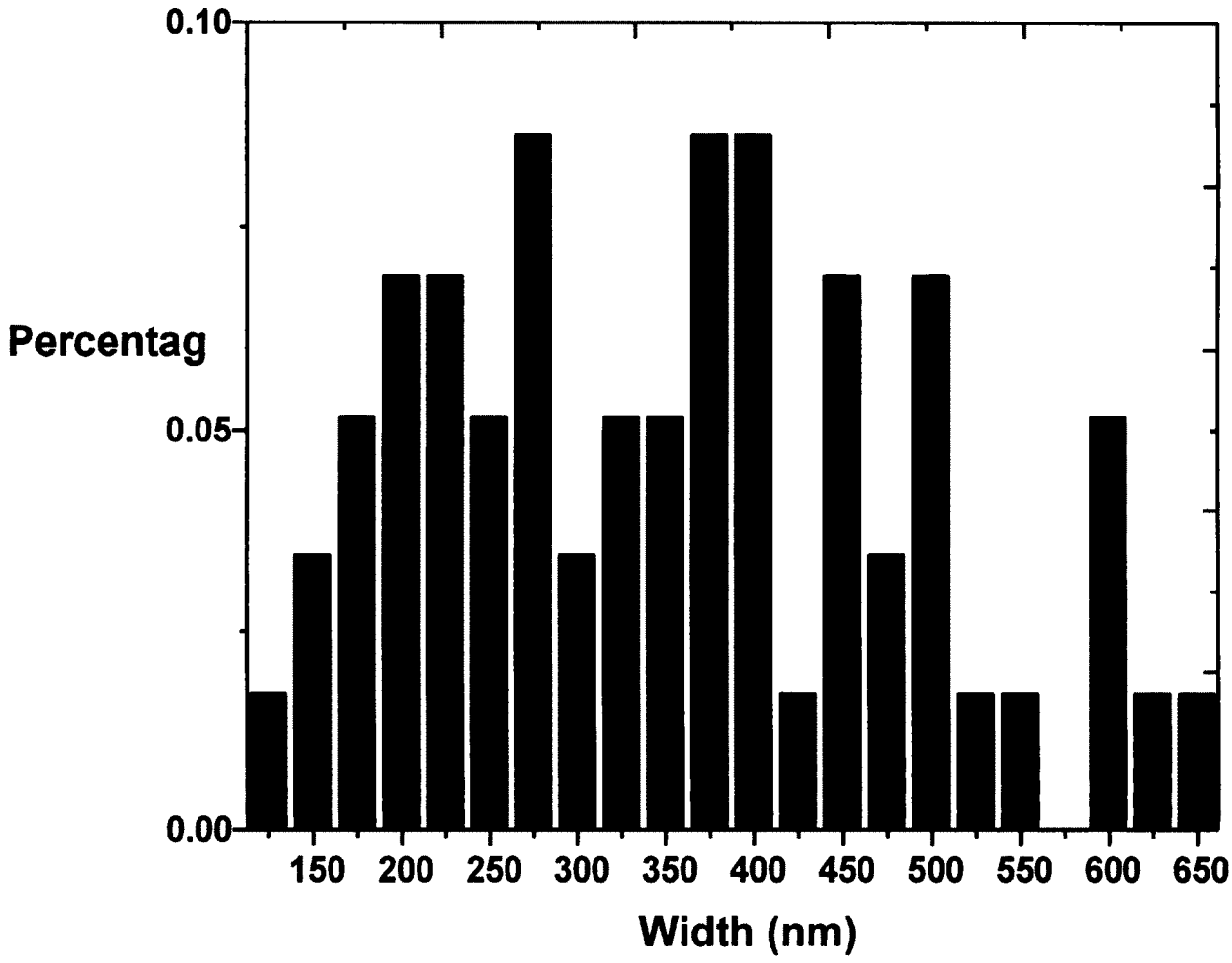

Figure 3.10: Width distribution of digested, homogenized & unfixed nano-straws.

Figure 3.11 displays 4.7 x 3.1 μm AFM height image of digested, homogenized & fixed costal cartilage taken in a phosphate buffered solution (PBS).

Figure 3.11: AFM height image of digested, homogenized & fixed costal cartilage in PBS.

Figure 3.12 shows the width distribution of digested, homogenized & unfixed nano-straws in PBS. Sixteen nano-straws' widths were measured, giving a mean value of 331 nm and a standard value of 84. These values differ significantly from those of fixed samples.

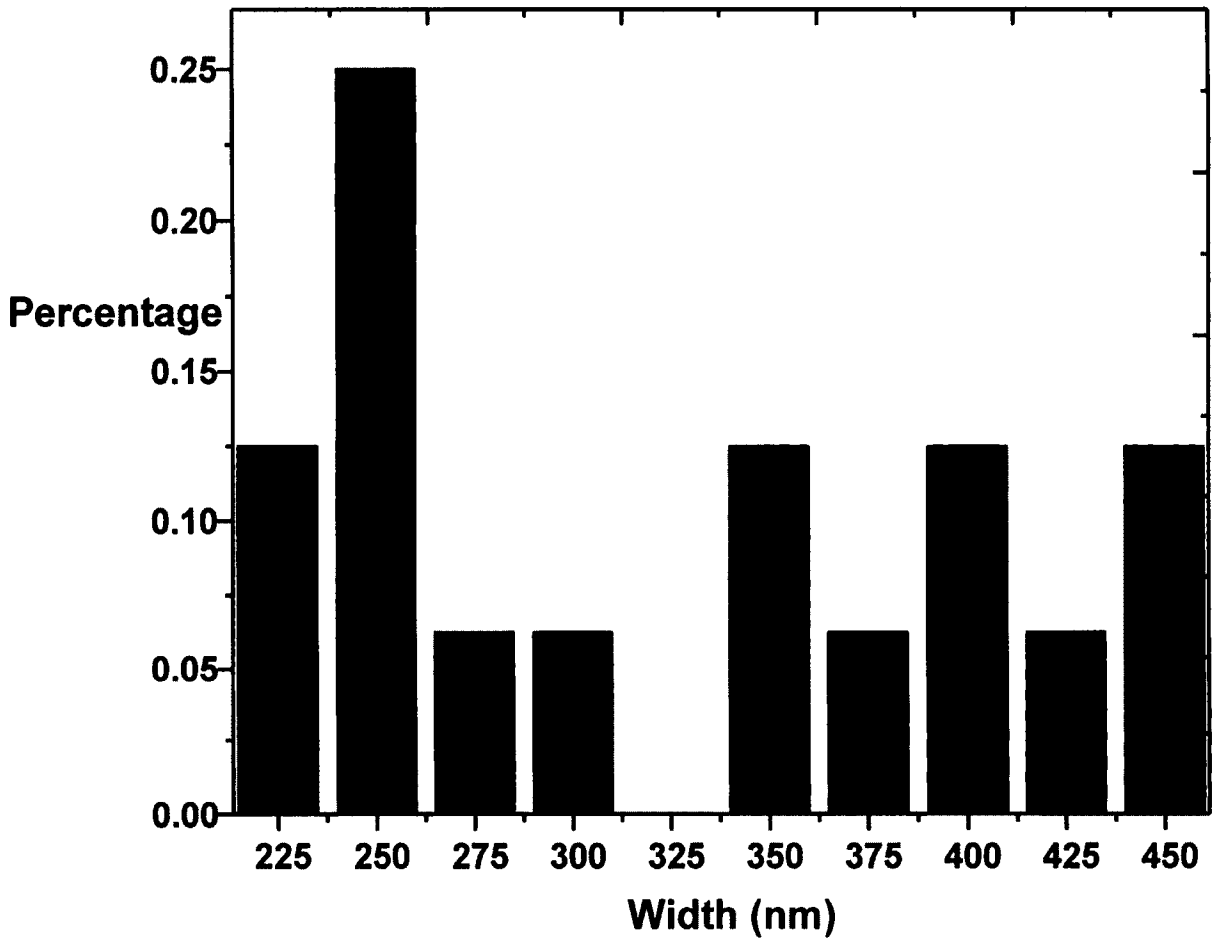

Figure 3.12: Width distribution of digested, homogenized & fixed nano-straws in PBS.

Figure 3.13 is of a 4.7 x 5.8 μm AFM height image of costal cartilage sample taken while the sample was in PBS. The samples were unfixed, homogenized and digested.

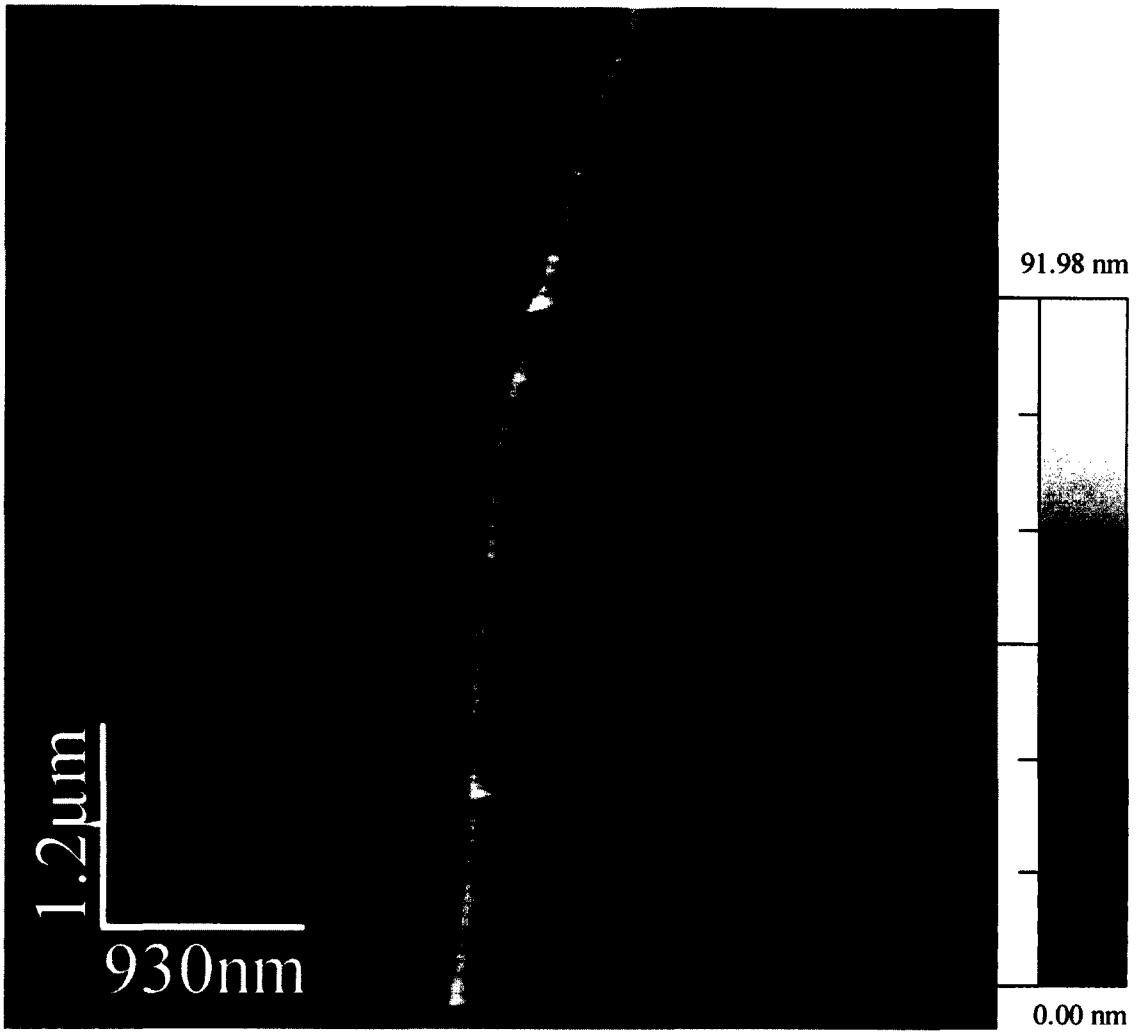

Figure 3.13: AFM height image of fixed homogenized and digested in PBS.

Figure 3.14 gives the width distribution of digested, homogenized & fixed nano-straws width distribution in PBS buffer solution. From this set, 26 nano-straw widths were measured. Within, a mean value of 410 nm and a standard deviation of ±120 nm were obtained. The mean differed from the unfixed samples.

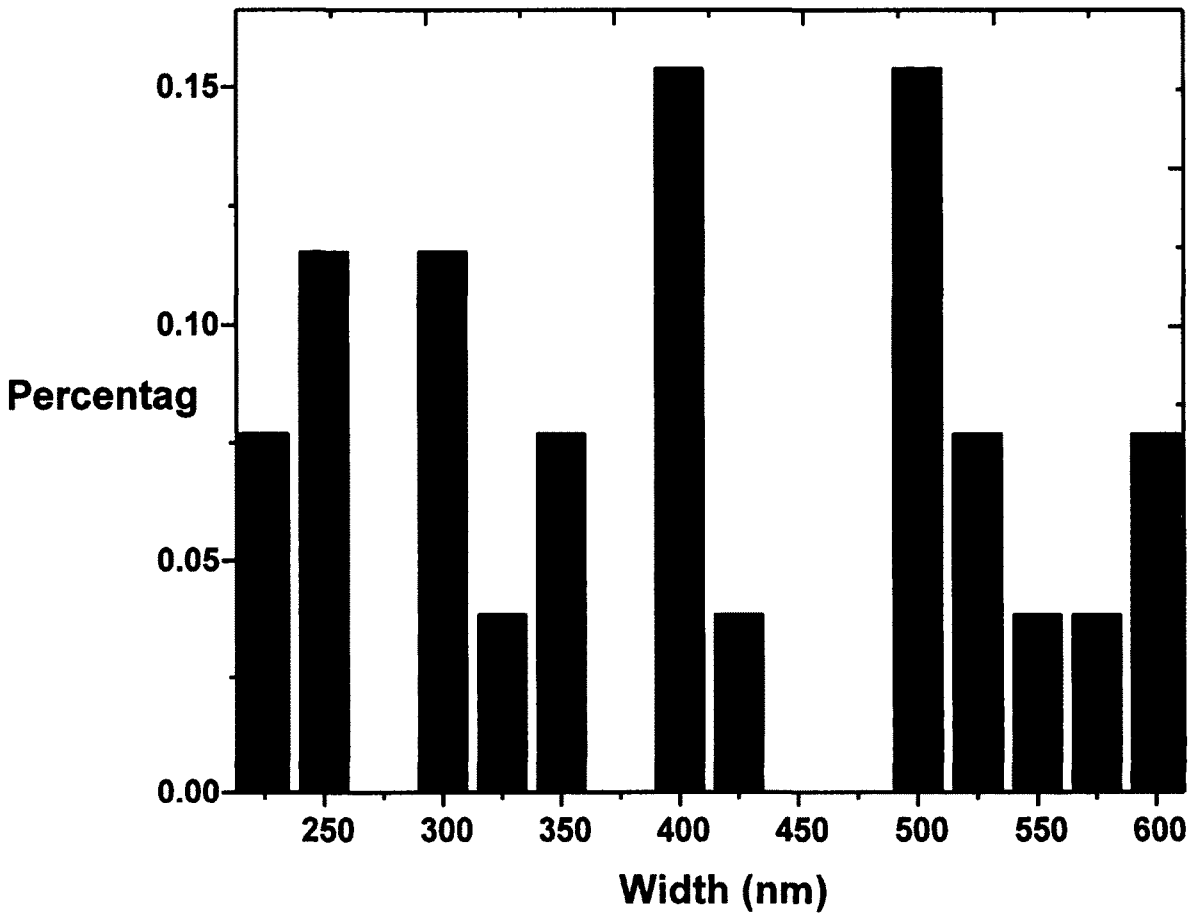

Figure 3.14: Width distribution of digested, homogenized & unfixed nano-straws in PBS.

Table 3.1: Statistical analysis of six different treatment and fixation.

P Values	Undigested & Fixed In Air	Digested & Fixed in Air	Homogenized, Digested & Fixed in Air	Homogenized, Digested & unfixed in Air	Homogenized, Digested & Fixed in Buffer	Homogenized, Digested unfixed in Buffer
Undigested	x	0.0315	0	0.0002	**0.3330**	0.0001
Digested		x	0.0012	0	0.0493	0
Homogenized & Digested			x	0	0.0001	0
Not Fixed in Air				x	**0.0993**	**0.2801**
Fixed in Buffer					x	0.0162
Not Fixed in Buffer						x

In the statistical analysis, if two sets of p values are less than 0.05, there exists a difference in the distributions that is statistically significant. P values obtained are 0.3330 for undigested and fixed nano-straws in air and digested, homogenized, and fixed straws in buffer. Both sets of data are similar. P values are 0.2801 for digested, homogenized and fixed samples in air and digested, homogenized, and unfixed samples in buffer. Statistically, they are almost the same set of data. Another set of data is statistically the same with values at 0.0993; both of them were digested and

homogenized; one set of data was in air and unfixed and another set of data was fixed in buffer. Digested and homogenized samples in air and buffer showed P is 0.0001; both sets of data are significantly different from one another. The rest of the data sets have P values lower than 0.05; they are statistically significant.

Additionally, we also observed topological features of collagen fibers that were expected based on previous literature. Figure 3.15 shows repeated D-Zone bands of collagen fibers. These types of bands are common in collagen fibers. Their size is about 67 nm in hydrated samples and 64 nm in dehydrated samples [163]. I measured D-Zone bands on homogenized and digested samples with the aid of AFM. The bands are repeated about 65 nm as we can see from Figure 3.15. My measurements are consistent with the above work.

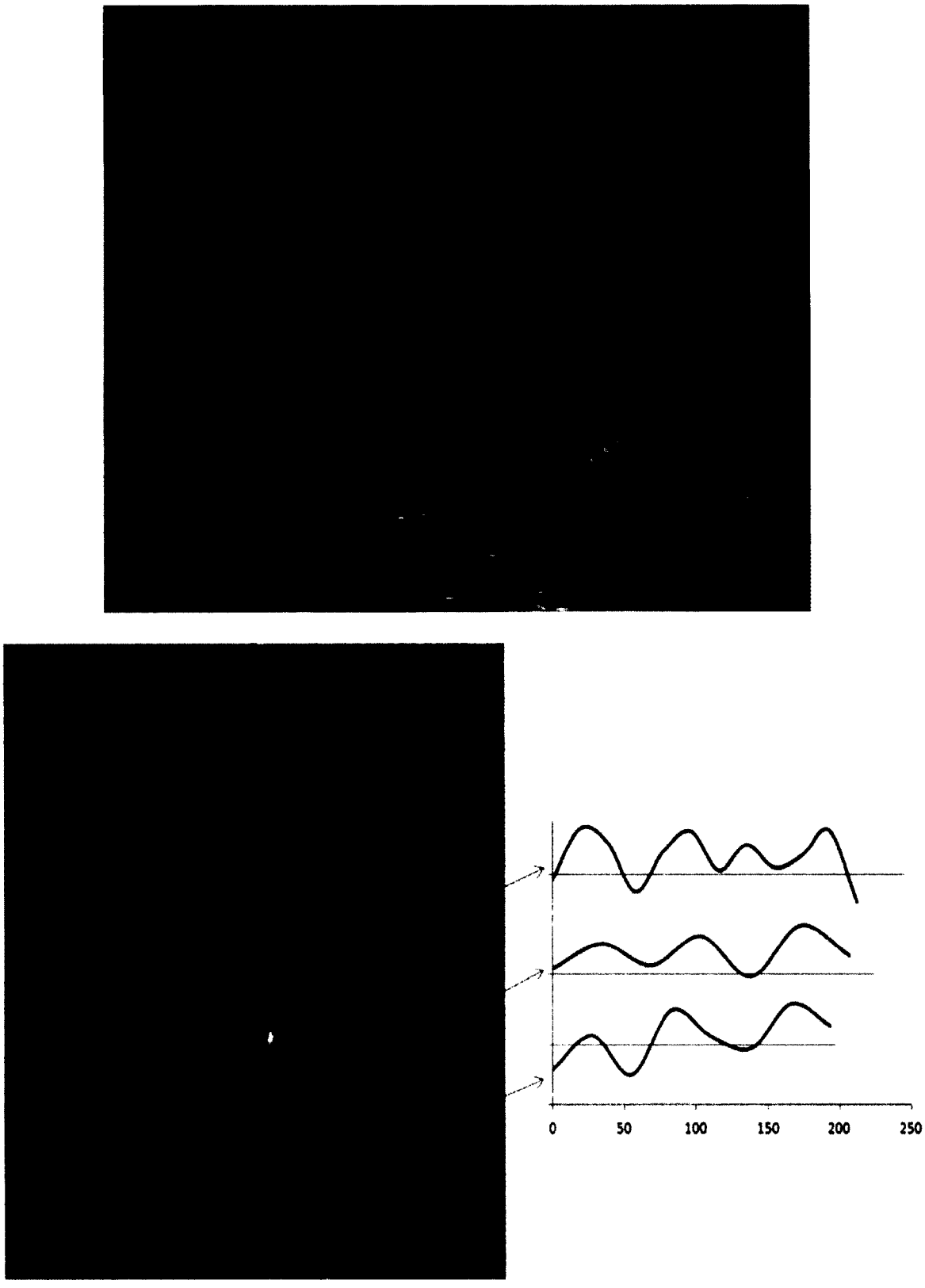

Figure 3.15: Collagen fiber band measurements using AFM.

3.4 Theory of Nano-mechanics

3.4.1 Hertz Theory

In 1882, Hertz solved the problem of a sphere indenting on to another sphere or elastic half-space. He gave the stress distribution with an indentation depth δ in the area of contact. Let us assume that an applied load is P, the sphere radius is R, the contact radius is a, and the indentation depth is δ.

From Hooke's Law we can write

$$\sigma = \varepsilon E \text{ ; Stress } \sigma \approx \frac{P}{\pi a^2} \text{ ; Strain } \varepsilon \approx \frac{a}{R}. \tag{3.1}$$

The hypotheses of the Hertz model are [164]:

1) The surfaces are frictionless.

2) No tensile stress is on the contact area.

3) There is very small strain within the elastic limits.

Two different size circles are in contact and their radiuses are R1 and R2 respectively. No pressure is being applied when the two bodies are in point contact. Now one sphere is being pressed on to the other with a load P. The center of the two spheres will shift by δ which is known as the indentation depth.

$$P = \frac{4}{3} \frac{1}{\left(\frac{1-\upsilon_1^2}{\pi E_1} + \frac{1-\upsilon_2^2}{\pi E_2} \right) \pi} \delta^{\frac{3}{2}} \sqrt{R} \tag{3.2}$$

$$\text{Let, } E^* = \frac{1}{\left(\frac{1-\upsilon_1^2}{E_1} + \frac{1-\upsilon_2^2}{E_2} \right)} \tag{3.3}$$

$$P = \frac{4}{3} E^* \delta^{\frac{3}{2}} \sqrt{R} \tag{3.4}$$

3.4.2 DMT Model

To calculate the Young's modulus, a modified Hertz model known as the Derjaguin-Muller-Toporov (DMT) model was used [165]. The DMT model gives the stress distribution with an indentation depth δ in the area of contact using the equation below:

$$F_{interaction} = \frac{4}{3} E^* \delta^{\frac{3}{2}} \sqrt{R} + F_{adh} \tag{3.5}$$

3.4.3 Adhesion Force

The adhesion force (F_{adh}) of two elastic bodies is caused by intermolecular forces, which is located outside of these two bodies. This force decreases with the increase in distances between the bodies involved.

Adhesion force plays a vital role if one of the following conditions is satisfied [166]:

1) Both surfaces of the body are smooth.
2) One of the bodies is made of soft materials.
3) On small length scales, adhesion forces have larger influences than body forces.

The adhesion force is [164]:

$$F_{adh} = -4\pi\gamma R \tag{3.6}$$

3.5 Results: Nano-mechanical Analysis of Polymeric materials Using AFM

Poly-dimethylsiloxane (PDMS) is a soft material that is widely used for creating devices through micro & nano fabrication techniques. PDMS was bought from Dow Corning. Two materials were used for PDMS fabrication: one is a base and another is a curing agent. The base and curing agent were mixed with a 10:1 (w/w) ratio. Enough was added to allow for a height of 2 cm within the petri dish that it was poured in and was then stirred to mix well. The PDMS was checked to make sure that no bubbles were in it. The mix was then stored in a clean place for 24 hours at room temperature to cure and harden. The PDMS was cut into several small pieces for 1 cm x 1 cm AFM measurements and screened for dust. One small piece was attached above the cover slip and placed into the AFM sample holder for experimentation. Nano-indentation experiments were carried out using the Nanonics AFM setup. Before experiments, the resonance frequency and quality factor of the AFM nano-probe was checked using NWS software. In this experiment, the resonance frequency was 30123 Hz which matches with the given manufacturer values. Figure 3.16 shows six different nano-indentation experimental data sets on PDMS. All six nano-indentation data sets are consistent and repeatable with each other.

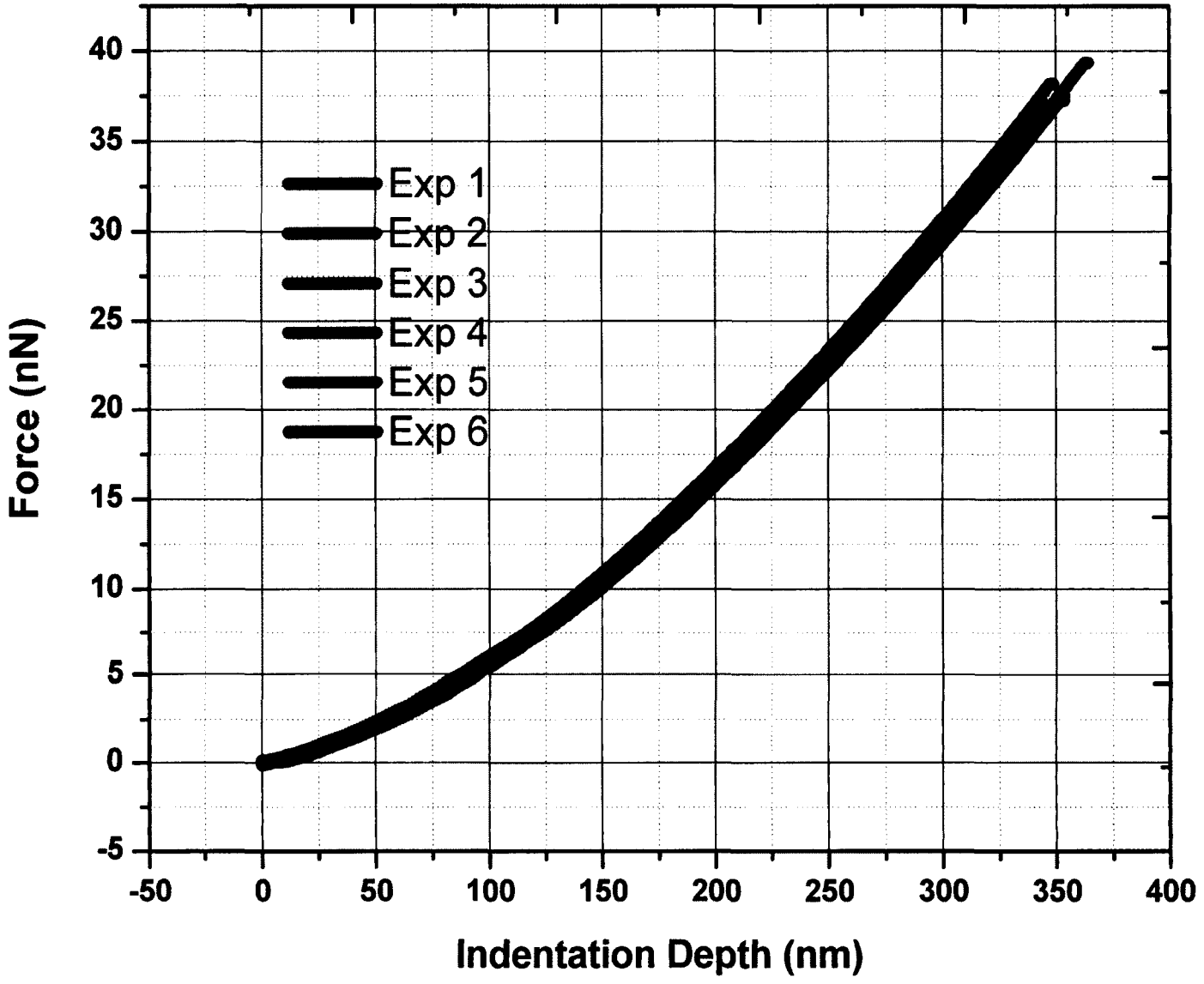

Figure 3.16: Different nano-indentation experiments on PDMS.

Figure 3.17 shows the experimental data from Figure 3.16 fitted with Hertz model. The experimental data was satisfactorily fitted using this theory.

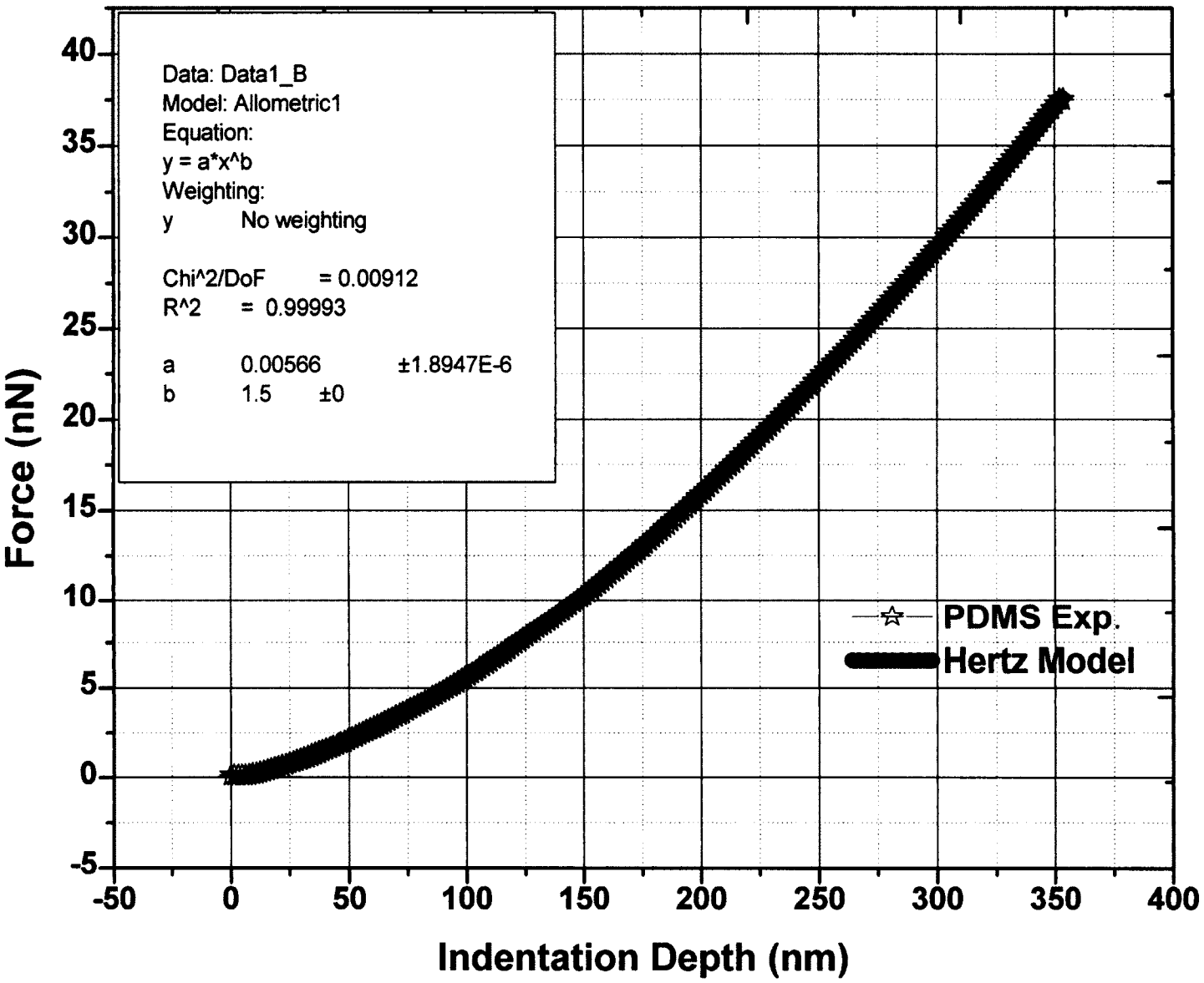

Figure 3.17: Nano-indentation experiment data on PDMS fitted with Hertz model.

Figure 3.18 shows PDMS local moduli of elasticity at different indentation depths. The Young's modulus of elasticity values for PDMS reached the bulk values after 15 nm indentation.

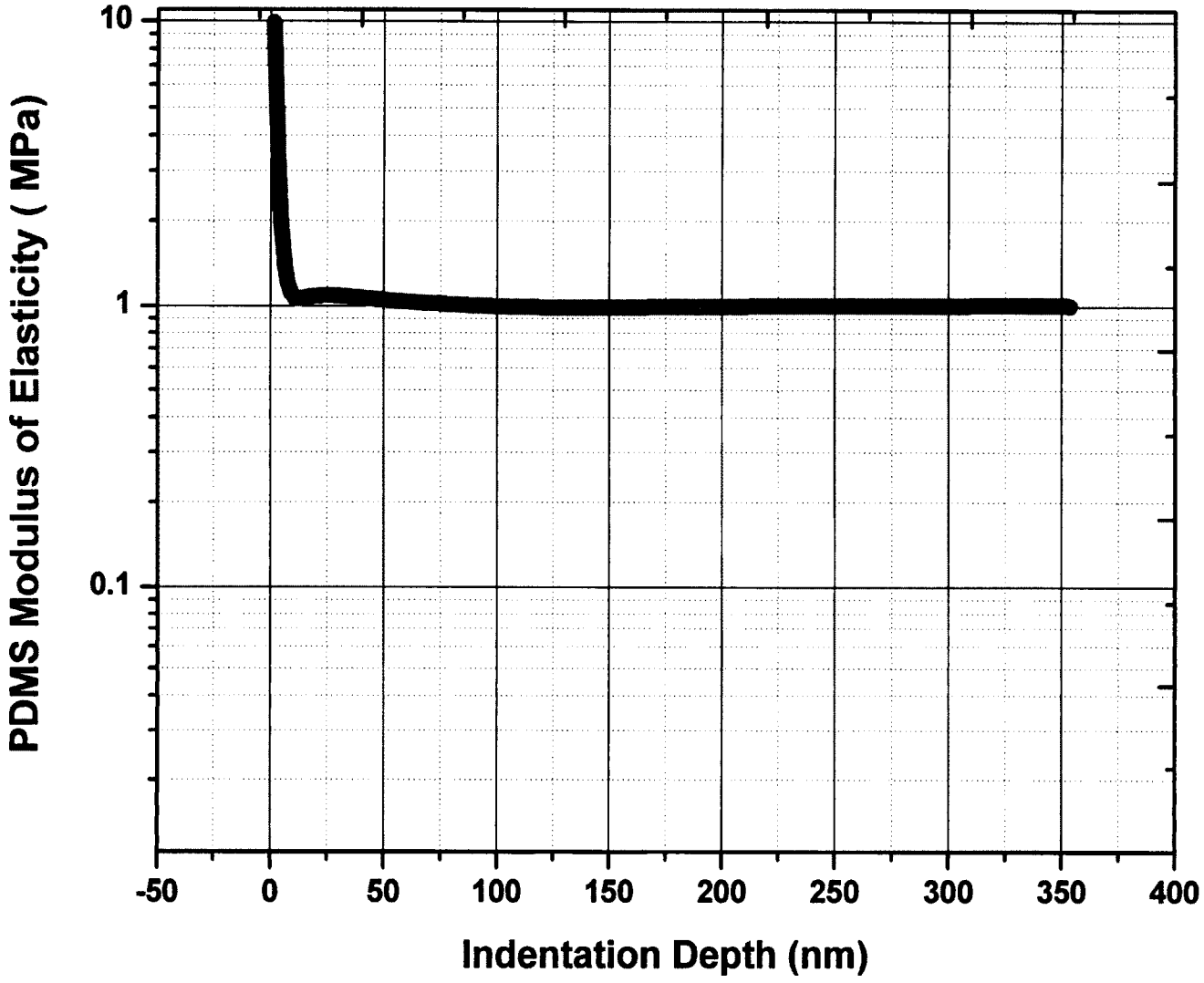

Figure 3.18: PDMS local modulus of elasticity values.

Table 3.2 shows six different PDMS experimental data sets fitted to obtain the Young's modulus of elasticity using two different models. For the Hertz model, the PDMS modulus of elasticity is 1.02 MPa, and the standard deviation is 0.02 MPa. For the DMT

model, the PDMS modulus of elasticity is 1.01 MPa, and the standard deviations is 0.02 MPa.

Table 3.2: PDMS modulus of elasticity values at different experiments.

	Hertz (MPa)	DMT (MPa)
Exp 1	1.00	1.00
Exp 2	1.05	1.04
Exp 3	1.00	0.99
Exp 4	1.00	1.01
Exp 5	1.02	1.00
Exp 6	1.04	1.03
Average	1.02 (±0.02)	1.01 (±0.02)

3.6 Results: Nano-Mechanical Analysis of Biological Tissues Using AFM

We executed nano indentation experiments on cartilages to measure the mechanical properties of the patient with pectus deformity. Initially, AFM experiments were performed on homogenized and digested fixed samples in air. AFM scanning was performed in different places on the sample surfaces. Nano-straws were found through AFM scanning. Nano-indentation experiments were then performed as shown above. Figure 3.19 shows costal cartilage nano-indentation in air and experimental data fitted with the Hertz model. The red solid line represents Hertz model fit, and the blue symbol represents experimental data. The arrow shows where nano-indentation was performed.

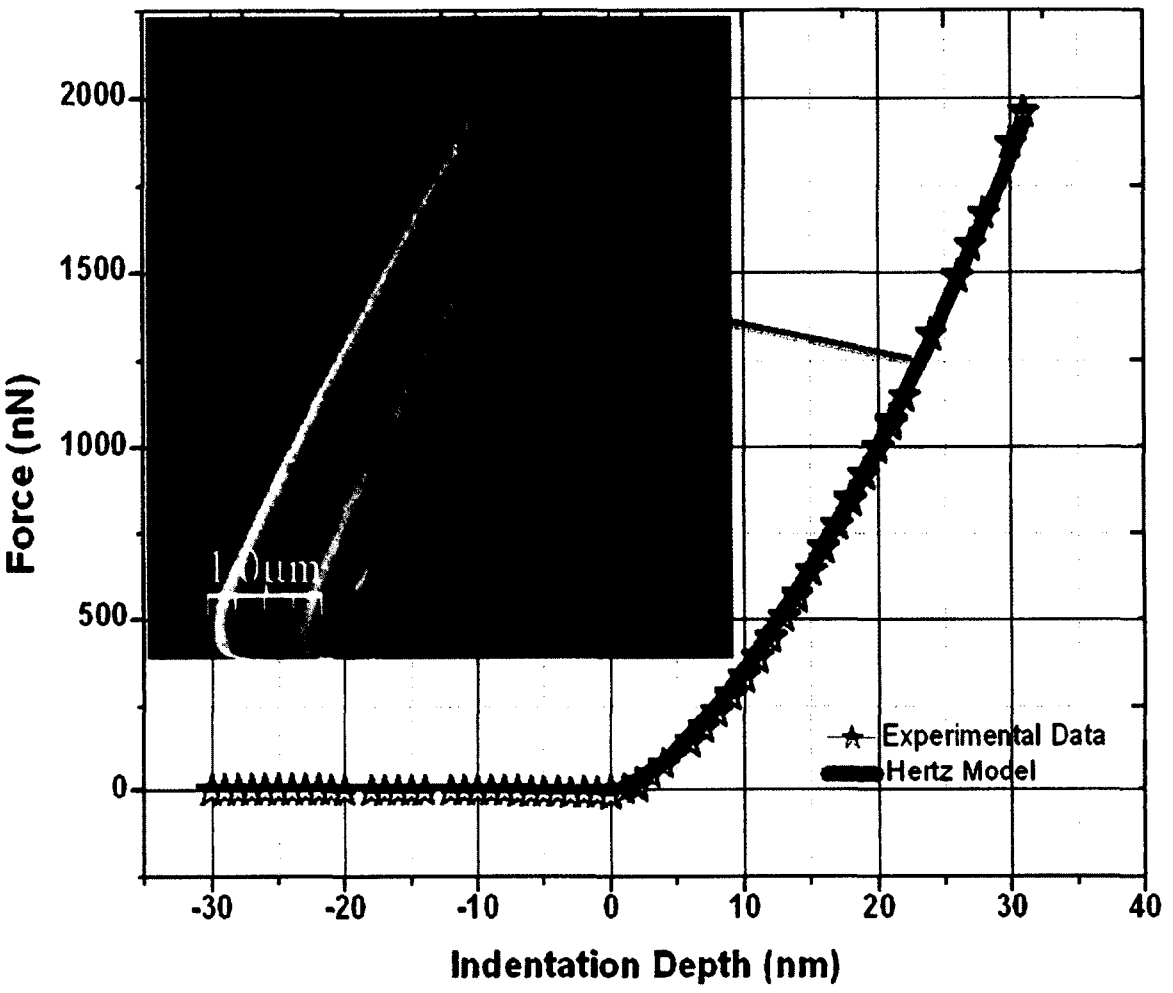

Figure 3.19: Nano-indentation experiment data on human costal cartilage at air fitted with Hertz model.

Figure 3.20 shows human costal cartilage modulus of elasticity at different indentation depths. Collagen nano-straws' modulus of elasticity reached the bulk value after 7 nm indentation.

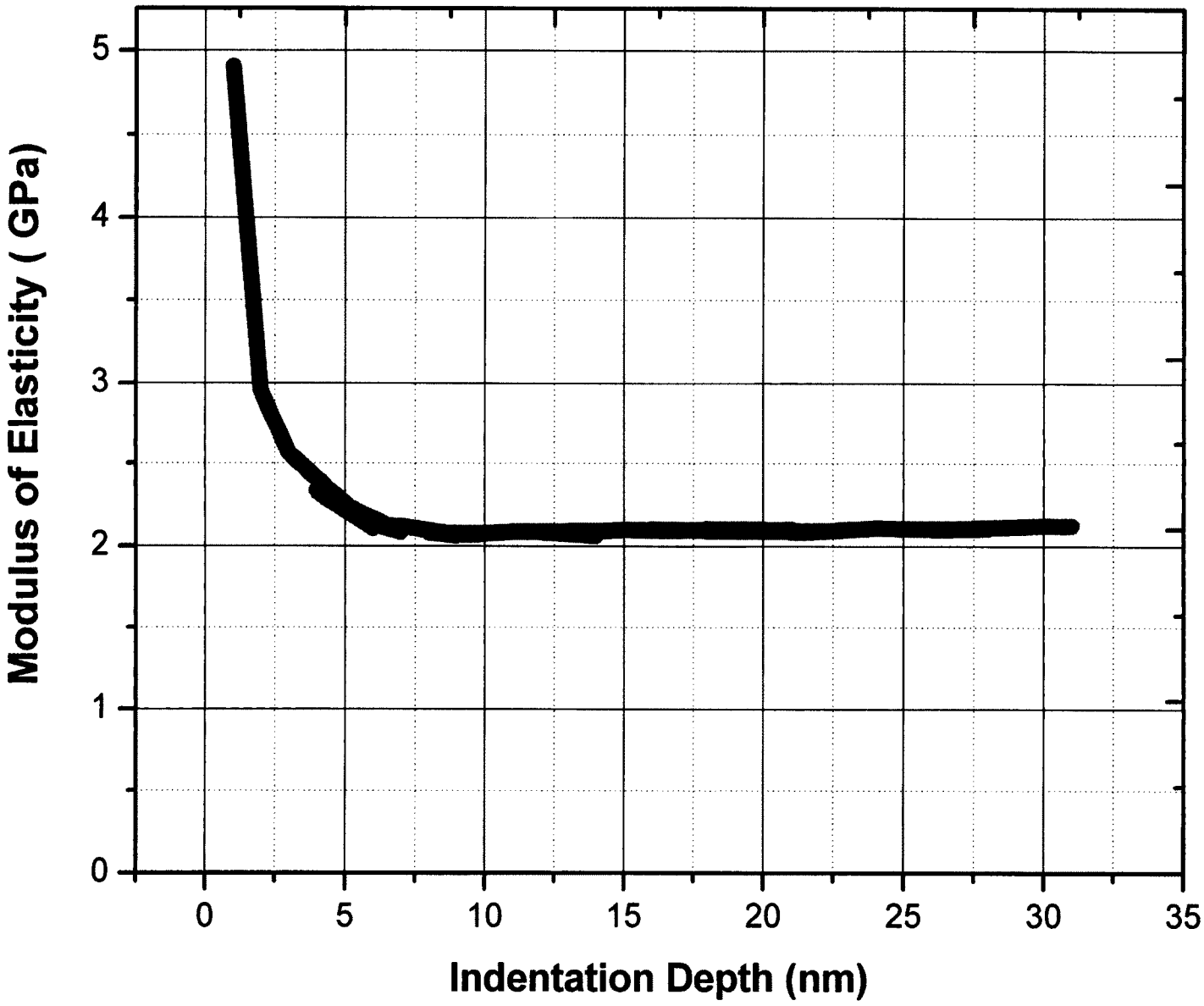

Figure 3.20: Human costal cartilages local modulus of elasticity values on air.

Table 3.3 shows modulus of elasticity values for collagen nano-straws in air obtained from fits using the Hertz and DMT models. According to the Hertz model fit, average collagen nano-straw's modulus of elasticity is 1.95 GPa, and the standard deviation is 0.26 GPa. According to the DMT model fit, average collagen nano-straw's modulus of elasticity is 2.05 GPa, and the standard deviation is 0.29 GPa.

Table 3.3: Human costal cartilage modulus of elasticity values on air at different experiments.

	Hertz (GPa)	DMT (GPa)
Exp 1	2.06	2.1
Exp 2	1.59	1.6843
Exp 3	2.21	2.3893
Exp 4	1.93	2.0323
Average	1.95 (± 0.26)	2.05 (±0.29)

AFM experiments were also performed on homogenized and digested fixed samples in PBS. Before nano-indentation experiments, AFM imaging was done in different places on the biological sample surface. Collagen nano-straws were found from AFM scanning. Then, nano-indentation experiments were performed on nano-straws. Figure 3.21 shows costal cartilage nano-indentation in PBS and experimental data fitted with the Hertz model. The red solid line represents Hertz model fit, and the blue symbol represents experimental data. The arrow shows where nano-indentation experiments were performed.

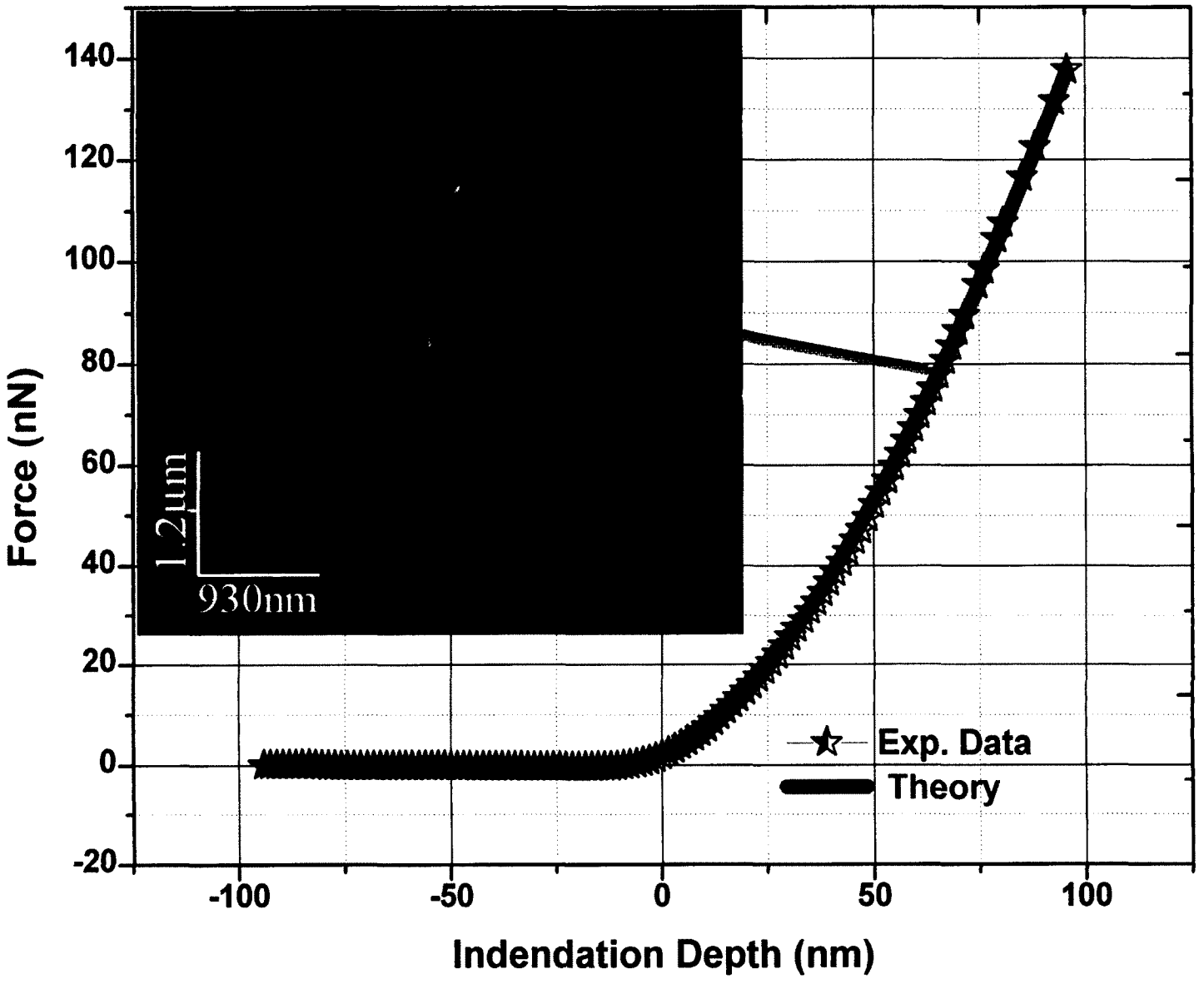

Figure 3.21: Nano-indentation experiment data on human costal cartilage in buffer fitted with Hertz model.

Figure 3.22 shows human costal cartilage modulus of elasticity at different indentation depths. In this experiment the indentation depth is about 100 nm. Collagen nano-straws' modulus of elasticity reached the bulk value after 20 nm indentation.

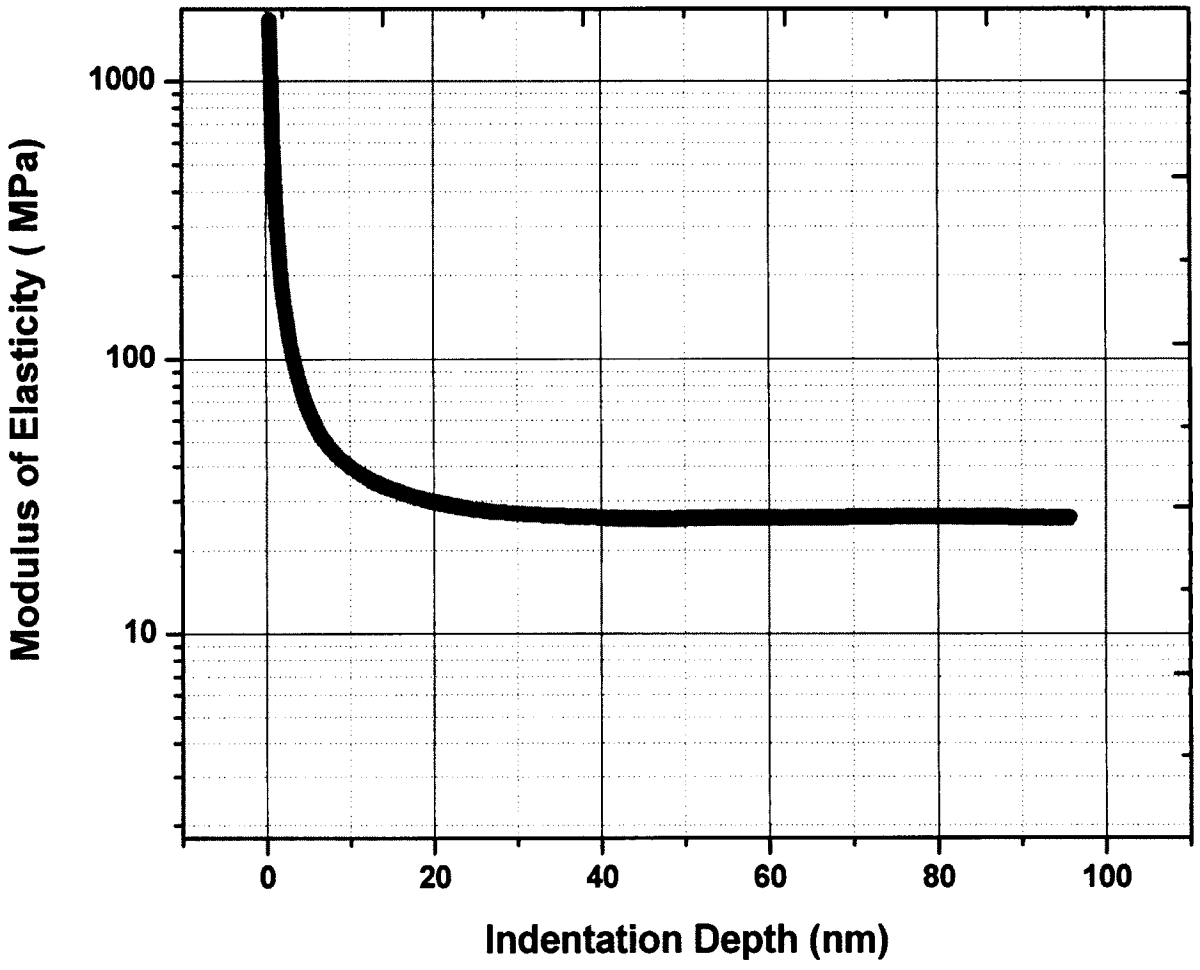

Figure 3.22: Human costal cartilages local modulus of elasticity values in buffer.

Table 3.4 shows modulus of elasticity values of collagen nano-straws using Hertz and DMT model fits when the collagen nano-straws are in PBS. In the Hertz model, the

average collagen nano-straws' modulus of elasticity is 24.44 MPa, and the standard deviation is 3.3 MPa. In the DMT model average collagen nano-straw's modulus of elasticity is 24.3 MPa, and the standard deviation is 2.55 MPa.

Table 3.4: Human costal cartilage modulus of elasticity values on buffer at different experiments.

	Hertz (MPa)	DMT (MPa)
Exp 1	21.1	21
Exp 2	20.6	22.3
Exp 3	27.4	25.2
Exp 4	26.7	27.1
Exp 5	26.4	25.9
Average	24.44 (± 3.30)	24.3 (± 2.55)

3.7 Conclusions

Costal cartilage imaging shows lots of nanostraws of unusual shape. These straws are thought to aid fluid flow from the bony rib to the sternum [30]. These nanostraws pass the length of the costal cartilage, and knowledge of their nano-structure will help model this fluid flow in the future. In our study, the samples were treated in six different ways. We measured nanostraws' diameter distributions in each case. In each case, diameter distributions are different from one case to another case due to the chemical treatment and fixation. The difference in diameter distribution can affect the nanofluids' transport calculations. Our results play an important role for nano scale measurements. We also measured Young's modulus of elasticity of nanostraws in air and physiological conditions. In the ambient condition, the nanostraws' modulus of elasticity was about 2.01 GPa. These tissues became harder, presumably due to the protein crosslinking. In physiological conditions, the costal cartilage modulus of elasticity was about 23 MPa, which is about 1000 times lower than in the ambient condition.

CHAPTER 4

NANOSECOND PULSING CELLS MORPHOLOGY, NANO-MECHANICS AND NANO-CHEMICAL ANALYSIS

4.1 Introduction

Cancer can be described as a wide range of diseases that stem from unregulated cell growth. There are many different types of cancers that affect different tissues of the body, leading to a variety of problems that often result in death. In the process of uncovering many of the mechanisms behind the behavior of some cancers and their effects on the body, in hopes of treating afflicted patients and preventing it, varying models have been used to study cancerous cells and tissues in order to predict their behavior. They range from the abstract to actual physical cell parts or whole cells to mimic cancer cell and tissue behavior. These models can entail the use of molecules used by the cancerous and normally functioning versions of the cells to the actual cancerous cells themselves to be studied in vitro or in vivo. These models rely on experimental characterization of the cancer cells and their constituents. AFM is used to in the study of biological cell's ultrastructure mapping and their mechanical properties measurements [167-173].

In our work, we study the leukemia cancer cell line referred to as a Jurkat cancer cell. Jurkat cells, themselves, are a line of immortalized T-lymphocyte cells and are believed to be give insight into the inner working of leukemia cells. For our work, we use Atomic Force Microscopy to map the modulus of elasticity and the cell membrane surface charge density. These may differ between healthy and cancerous cells [174]; mapping these

qualities and quantities can be helpful in the creation of biomedical devices, medications, and techniques that can take advantage of these qualitative and quantitative differences. [175-179].

Electroporation (EP) is the creation of pores in a biological membrane through applying an electrical field across it. With careful application, the effects of electroporation can be temporary and beneficial, but this relies on properly monitoring the electric field strength, number of pulses, and the duration of each pulse [180-181]. Normally, the pulses do not last more than 100 us, and sub-kV/cm voltages are used, allowing for non-lethal, but large heterogeneous pores to form in the plasma membrane (182-189).

This study involves the use of AFM to explore how cellular morphology, surface charge density, and membrane elasticity of Jurkat cells changed with the application of a single 60 nanosecond pulse electric field (NsPEF) between 15kV/cm and 60 kV/cm field strengths, while also finding and calculating the Young's modulus for membrane elasticity through force indentation measurements. Using a tip and cells on silica in a 0.01 M KCL solution, we were able to measure the interfacial forces between them while also predicting both surface charge densities of Jurkat cell and silica surfaces.

We found that single low field strength NsPEFs could not breakdown the Jurkat cells' cytoskeletons or produce major morphological changes. Force measurements and Young's modulus calculations revealed a decrease in the elasticity of the Jurkat cells. The most important finding is that differential pulsing conditions reduced the cells' surface

charge density. Contrary to the effect of the single low field strength NsPEF, exposure of the Jurkat cells to the high field strength NsPEF resulted in fibrilliar actin disruption, a significant decrease in elasticity, reduction in charge density and major morphological changes.

Our data suggests that cellular morphology depends mainly on the stability of the actin cytoskeleton while the actin cytoskeleton's integrity influences the cell's elasticity and biochemical makeup along the cellular surface. Both the structure and physics from the chemical properties of biological cells immensely influence their electrostatic force; we were able to investigate this through the use of atomic force microscopy through measuring both surfaces' forces between the AFM's tip and Jurkat cells under different pulsing conditions but also the interfacial forces in ionic concentrations while the AFM tip came near the Jurkat cells.

We used a force separation curve to observe the local molecular forces of the biological cells under hydration with AFM. In this, the interaction forces between the AFM tip and surface are measured in terms of the force by distance, as the tip is approaching, contacting, and retreating from a given sample surface. This process can be exploited to yield many properties as they relate to the mechanical, chemical and biological properties of the cell, especially those of the electrochemical variety which the surface charge density is used to express, all of which need to be in certain values for proper cell function [190-191]. The AFM is very useful for this task in which picoNewton scale measurements are desired.

The effects of NsPEF involve the creation of compact and identical nanopores within the plasma membrane, organelle membranes, and the nuclear envelope [192-193]. NsPEFs that are greater than 10 kV/cm are considered high voltage, and even short pulses of short duration can cause cellular effects that differ from conventional EP. These NsPEFs make the cell membrane permeable without the need for propridium iodide [194], as opposed to conventional EP, and have been found to promote intracellular calcium uptake into the cytoplasm from intracellular stores and the extracellular environment [195-196]. Pulse durations shorter than the cell membrane charging time are responsible for the nanopore formation and intracellular structural penetration. Cell death is brought on by the permeabilization of both external and internal membranes which is thought to be the primary mechanism [197-198]. It was observed that NsPEFs generate damage to chromosomes and telomeres and disrupt the actin cytoskeleton, which is a factor in cell death [199-200].

The nature of pore formation in NsPEF subjected cells has been investigated before [201-202] without revealing the morphological changes or overall membrane elasticity and charge density changes across the cell surface. Here, Atomic Force Microscopy (AFM) was used to map the cellular morphology and measure changes in the elasticity and surface chemistry of these cells.

4.2 Methods

4.2.1 Silica Sample Preparation

A large silica wafer from Montco Silicon Technologies (San Jose, CA, USA) was used to produce the sample surfaces after being cut into 1 cm by 1 cm squares, followed by sonication with 1 M KOH from Acros Organics, New Jersey, USA for approximately 15 minutes. Afterward, these samples were rinsed with DI water for 2-3 minutes and sonicated with acetone for 15 minutes. The samples were then sonicated in isopropanol from Fisher Scientific Education (Pittsburg, PA, USA) for 15 minutes, before being rinsed with isopropanol and deionized water for 2-3 minutes. The samples were then dried with an air gun and placed on a heating plate for 3 minutes at 120 °C. They were then kept in clean boxes to protect against dust deposition. Prior to experimentation, the silica sample surfaces were kept above the sample holder for microscopic samples, to be analyzed by AFM fused silica probes bought from Nanonics in Israel.

4.2.2 Cell Culture

Jurkat E6-1 clones from ATCC were cultured in RPMI 1640 media from Atlanta Biologicals with 2 mM of L-glutamine, 50 IU/mL penicillin, and 50 mg/mL streptomycin from Gibco at 37 degrees Celsius and 5% CO2 in air.

4.2.3 Cell Electroporation and Preparation

Jurkat cells were placed in curvettes from Biosmith with 1 mm gaps and then exposed to one NsPEF of 60 nanoseconds with pulse strengths of 0, 15, and 60 kV/cm. The Jurkat cells were immediately fixed post-exposure with 4% paraformaldehyde and then

transferred to poly-L-lysine coated coverslips from Sigma-Aldrich, before being washed in PBS and imaged through AFM.

4.2.4 Atomic Force Microscopy

We used a Multiview-400 multiple probe AFM from Nanonics Imaging to obtain height, phase, and Near Field Scanning Optical Microscopy images. NWS and WSxM 5.0 imaging and processing software respectively were used for interfacing with the fixed cells on the AFM stage through the use of a 20 nm parabolic quartz tip in tapping mode and processing images obtained [160]. The tapping mode involves cantilever oscillation which allows for soft characterizations as the AFM scans. The cantilever's spring constant is 2600 uN/um, with a resonance frequency of 33.97 kHz. Image calibration was performed using a standard silicon grid and further verified with a profilometer.

4.3 Cancer Cells Nano meachanics

The Derjaguin-Muller-Toporov (DMT) model was used to calculate the Young's modulus as described below [62].

$$F_{tip} = \frac{4}{3} E^* \delta^{\frac{3}{2}} \sqrt{R} + F_{adh} \tag{4.1}$$

F_{adh} is the adhesion force between the AFM tip and the sample; R is the AFM tip radius; δ is the indentation depth; E^* is the relative young modulus. The relative young modulus can be written as

$$E^* = \frac{1}{\left(\frac{1-\upsilon_{tip}^2}{E_{tip}} + \frac{1-\upsilon_{sample}^2}{E_{sample}} \right)} \tag{4. 2}$$

E_{tip} is the young modulus of the AFM tip, E_{sample} is the young modulus of the Jurkat cells. υ_{tip} and υ_{sample} is the Poisson ratio of the AFM tip and Jurkat cells.

An algorithm, based on the least square fitting method, was developed to measure the cellss Young's modulus; it was verified with Matlab CFtool, and both gave the same results. CFtool is used to fit data with different models and visualize the curves and surfaces as well as automatic processing. The experimental data was fitted with equation 1 using our Matlab code. The equation has two fitting parameters: one is the adhesion force and two is the relative Young's modulus. The adhesion force is the constant force between tip and sample. From the relative Young's modulus, using equation 2, we measured Jurkat cells' modulus of elasticity. The student's t-test was used for statistical analysis, with a p value of <0.05 indicating a significant result.

Figure 4.1 is an AFM image of two Jurkat cells which display a height characterization with height scale bar shown to the right of the picture. At their height, they measure roughly 2.38 microns while their diameters were measuring about 10-12 microns across. These are Jurkat cells that did not receive electrical pulses.

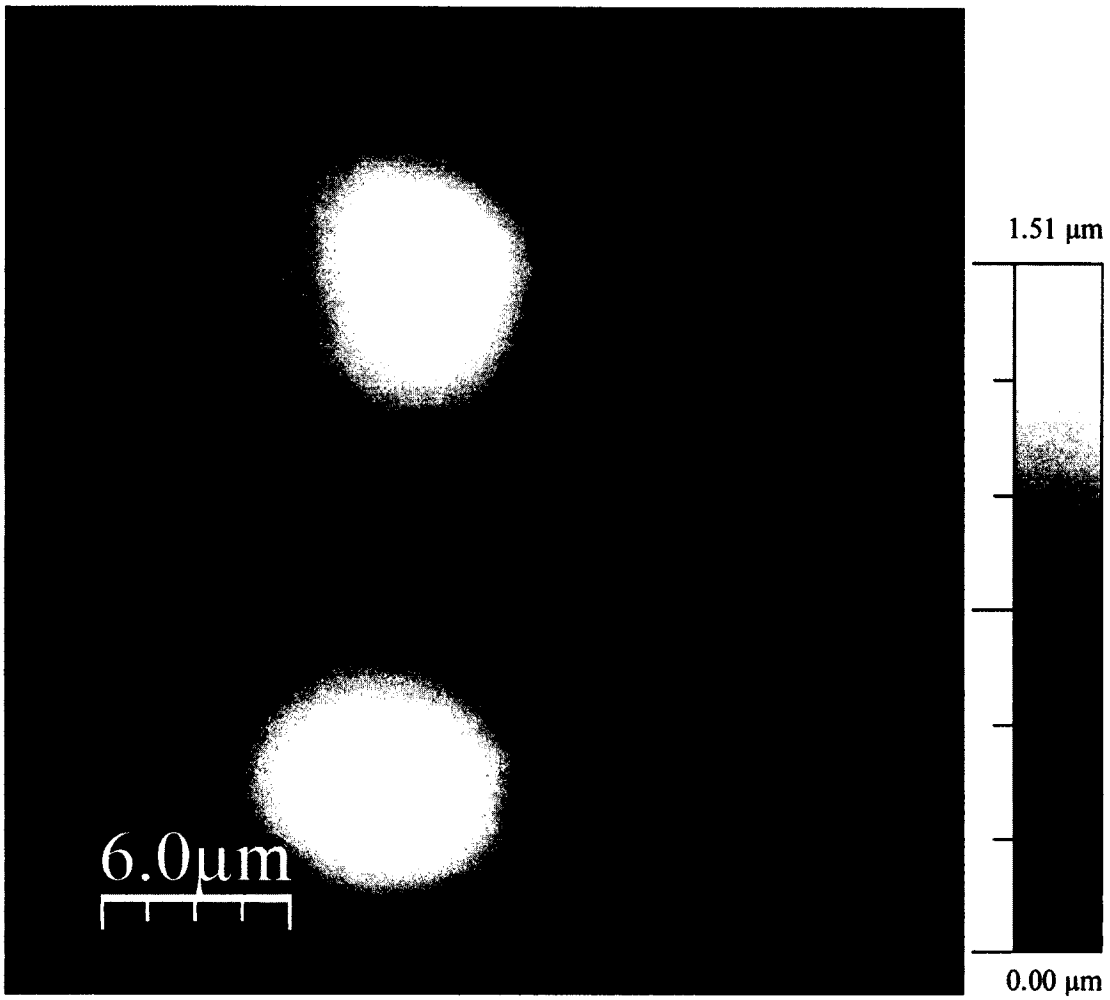

Figure 4.1: 30 x 30 µm Non Pulsed Jurkat cells AFM height image.

Figure 4.2 shows AFM nano-indentation on non-pulsed Jurkat cells. The mechanical contact force was applied above the Jurkat cells, and the indentation depth is about 100 nm. The blue symbols in the figure below show experimental data, and the red solid line represents the fit using theory.

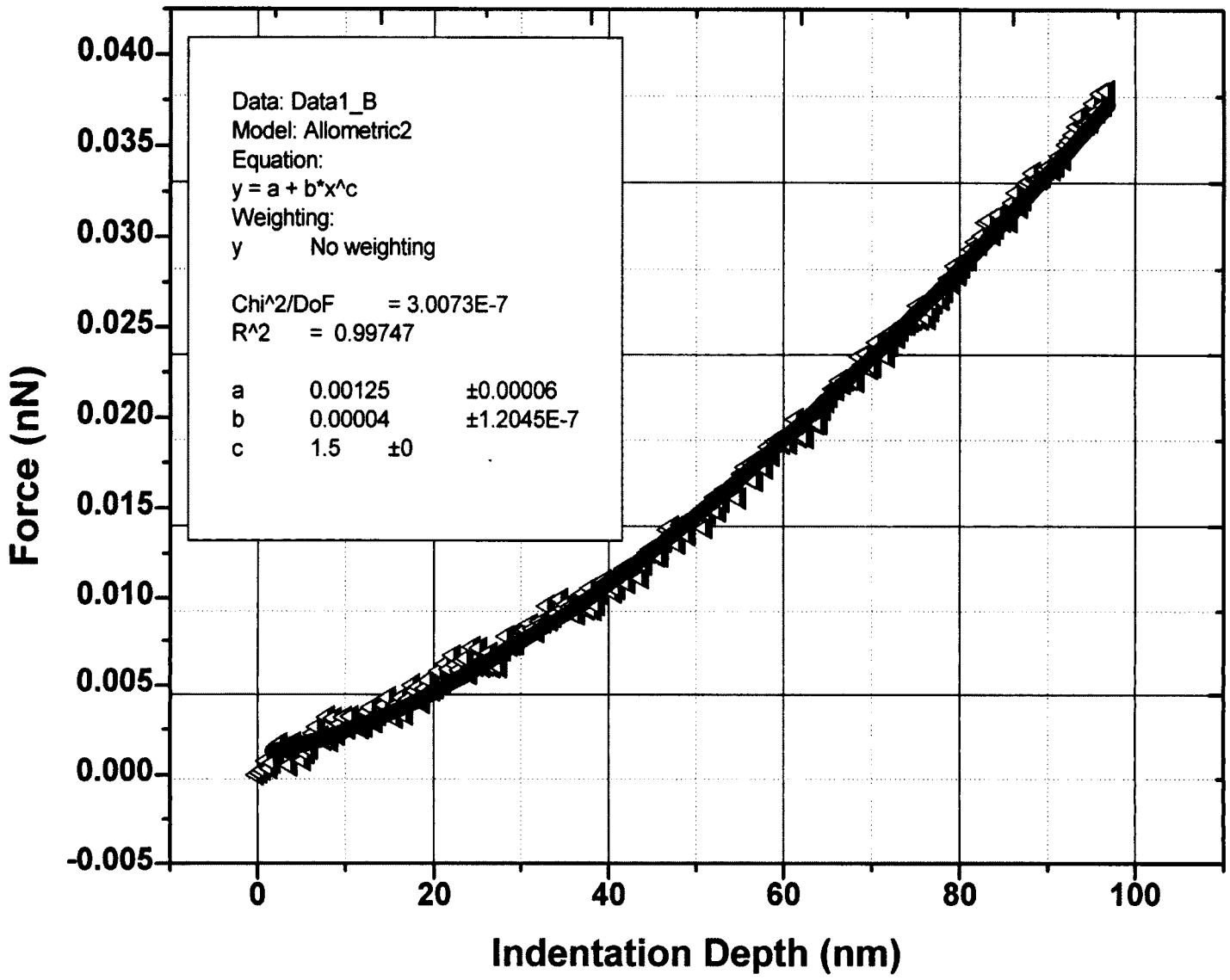

Figure 4.2: Nano-indentation experiment data on non pulsed Jurkat cell and fitted with DMT Model.

Figure 4.3 shows non pulsed Jurkat cells local moduli of elasticity at different indentation depths. The modulus of elasticity values reached bulk values after 35 nm indentation.

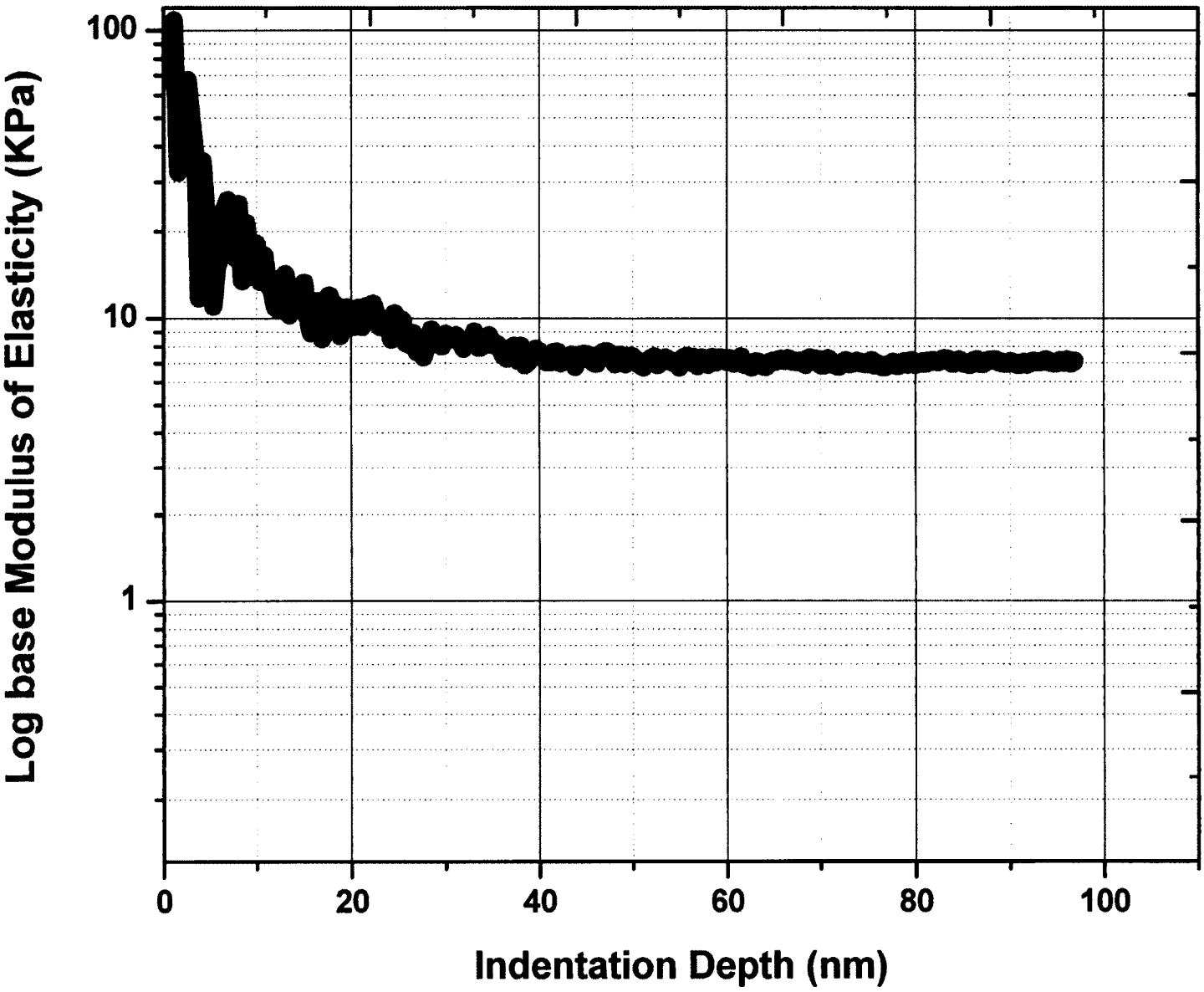

Figure 4.3: Non pulsed Jurkat cell local modulus of elasticity values.

As listed in Table 4.1 below, as with the curves above, the experimental values fit well with the model values. The non-pulsed Jurkat cells modulus of elasticity is about 7.27 kPa.

Table 4.1: Non pulsed Jurkat cells modulus of elasticity values at different experiments.

	DMT (KPa)
Exp 1	6.73
Exp 2	8.51
Exp 3	6.59
Average	7.27667 (±1.070)

Figure 4.4 shows an AFM image of a Jurkat cell which displays a height characterization. At their height, they measure roughly 2.84 microns while their diameters were measuring about 6-8 microns across. These are Jurkat cells that received electrical pulses; the electrical pulsing condition is 15 Kv/cm.

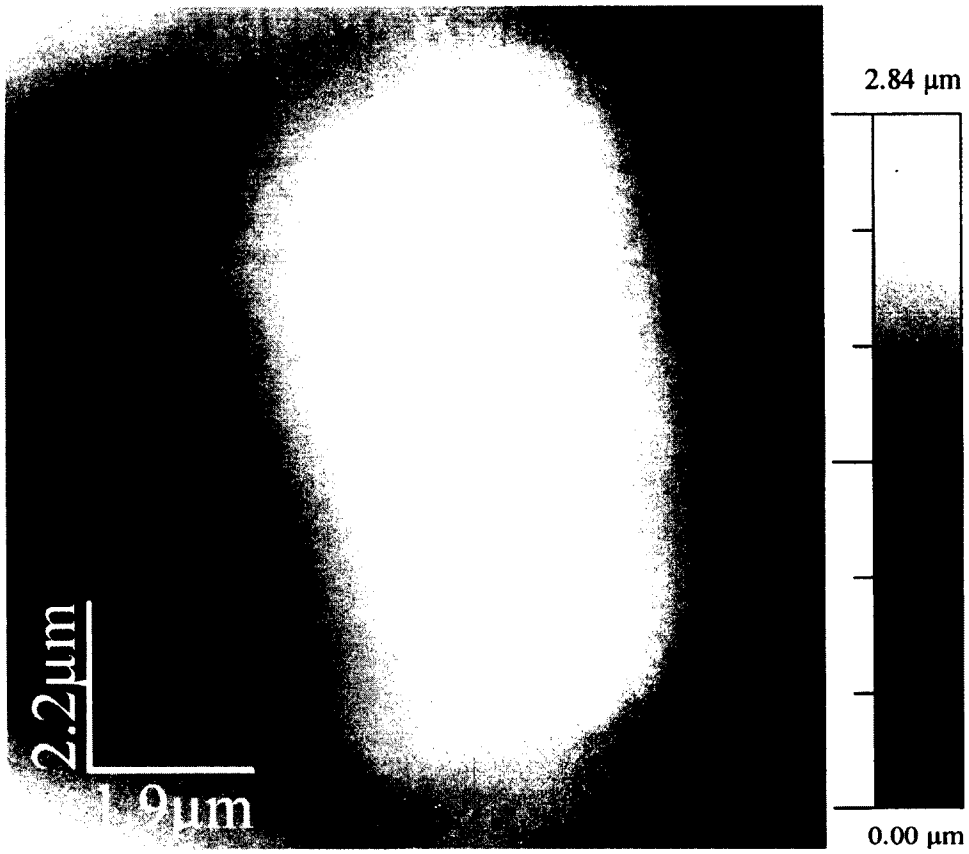

Figure 4.4: 9.3 x 11.1 µm Pulsed Jurkat cell (15kv/cm) AFM height image.

Figure 4.5 shows AFM nano-indentation plot on pulsed Jurkat cells. The mechanical contact force was applied above the Jurkat cells and the indentation depth is about 120 nm. The blue symbols in the figure below show experimental data, and the red solid line represents the theoretical data. From the following figure, we can say that the experimental data has a good fit with theoretical fit.

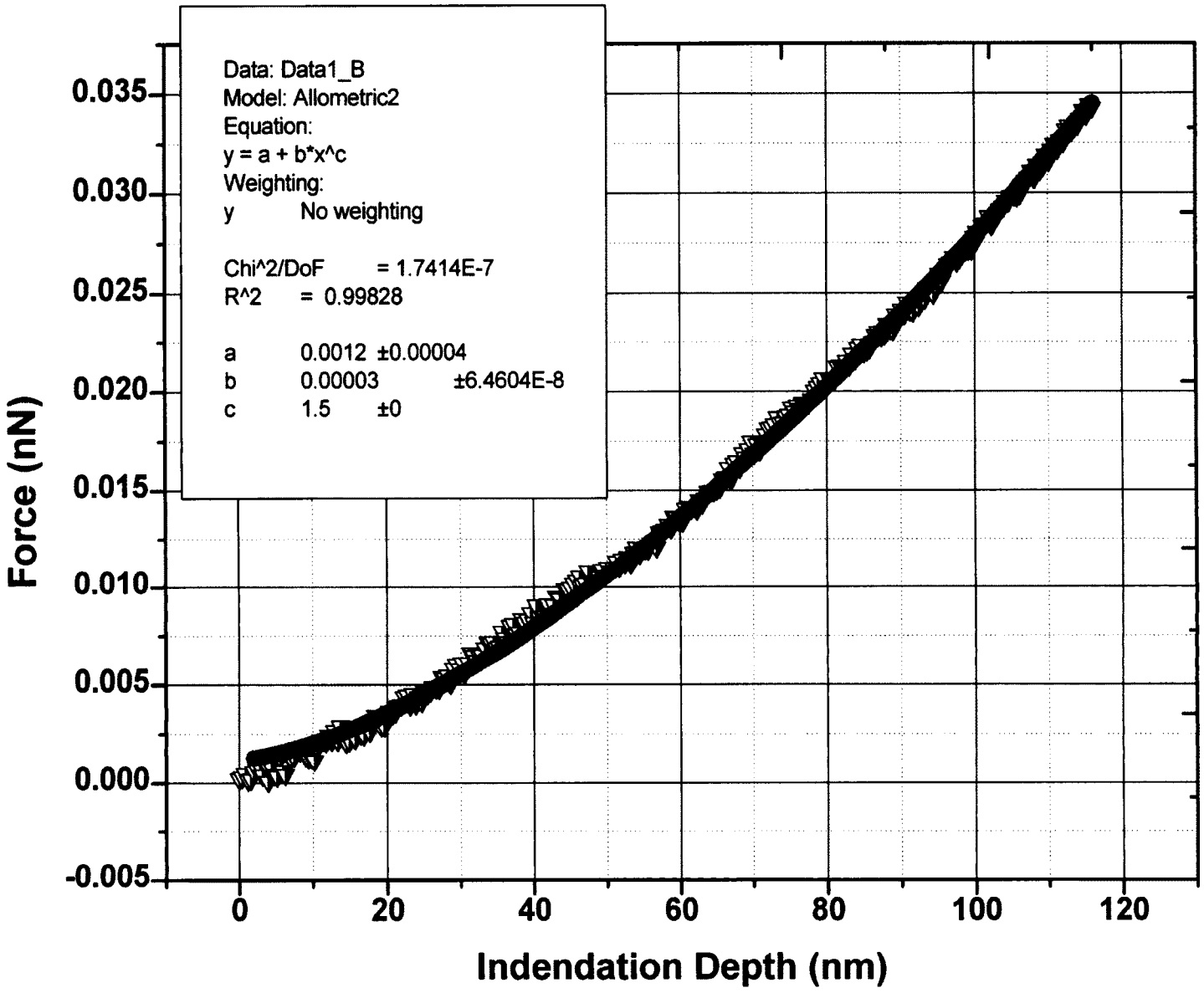

Figure 4.5: Nano-indentation experiment data on pulsed Jurkat cell (15/cm) and fitted with DMT Model.

Table 4.2 below shows the experimental values and the model values. The pulsed Jurkat cells (15 Kv/cm) modulus of elasticity is about 3.58 KPa for the DMT model. The modulus of elasticity is reduced for pulsed cells compared to non-pulsed cells. The reason for the reduced modulus of elasticity is presumably that the cells' membranes have broken down.

Table 4.2: Pulsed Jurkat cells (15 Kv/cm) modulus of elasticity values at different experiments.

	DMT (KPa)
Exp 1	4.74
Exp 2	2.49
Exp 3	2.9782
Exp 4	4.1323
Average	3.58513 (±1.03292)

Figure 4.6 is an AFM image of a Jurkat cell which displays height characterization. Their height measures roughly 4.09 microns. The electrical pulsing condition is for the cell shown below is 60 Kv/cm.

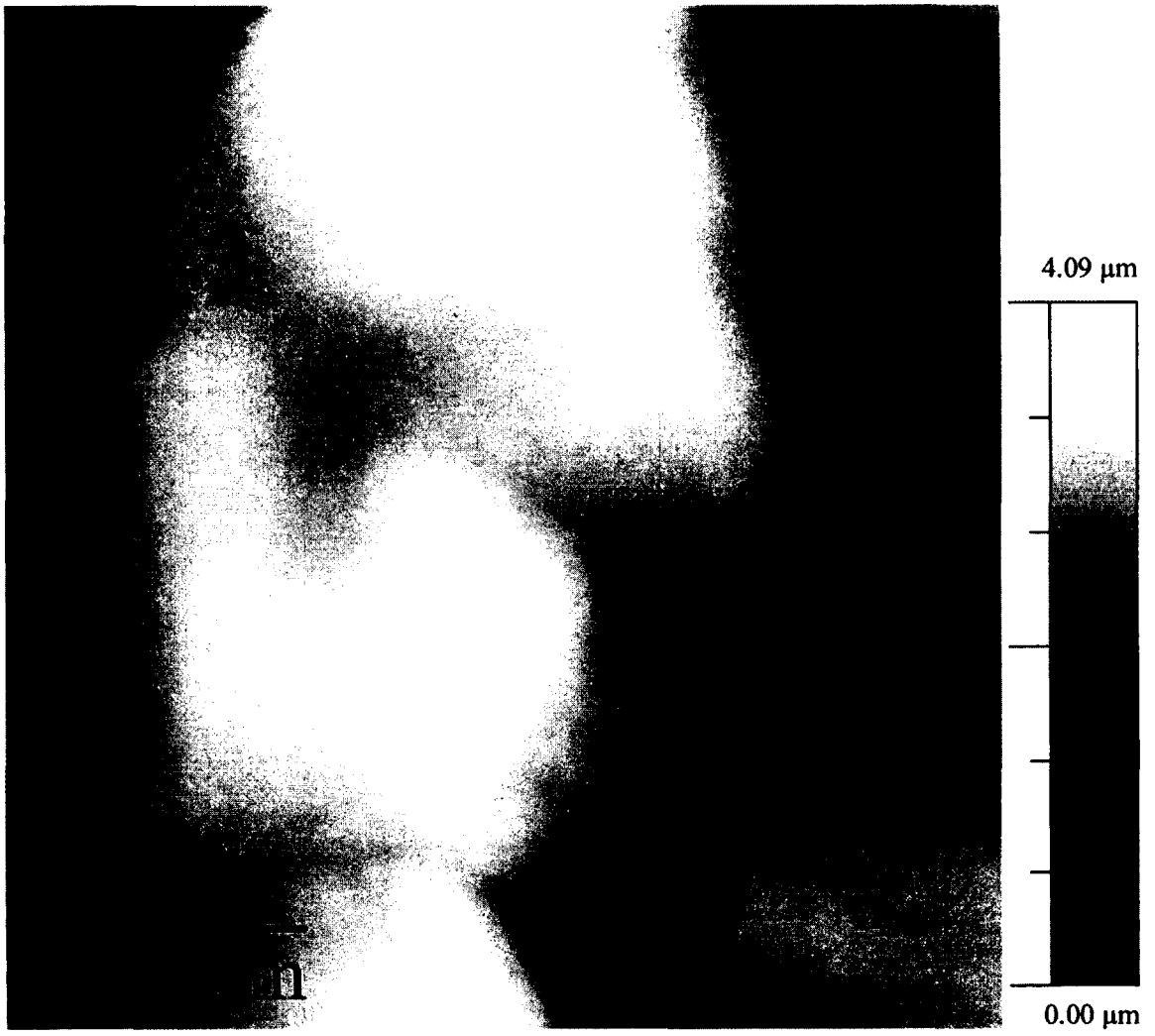

Figure 4.6: 10.9 x 16.4 μm Pulsed Jurkat cells (60kv/cm) AFM height image.

Figure 4.7 shows AFM nano-indentation on pulsed Jurkat cells. The indentation experiments were carried out above the Jurkat cells, and the indentation depth is about 100 nm. The blue symbols in the figure below show experimental data, and the red solid line represents the theoretical fit.

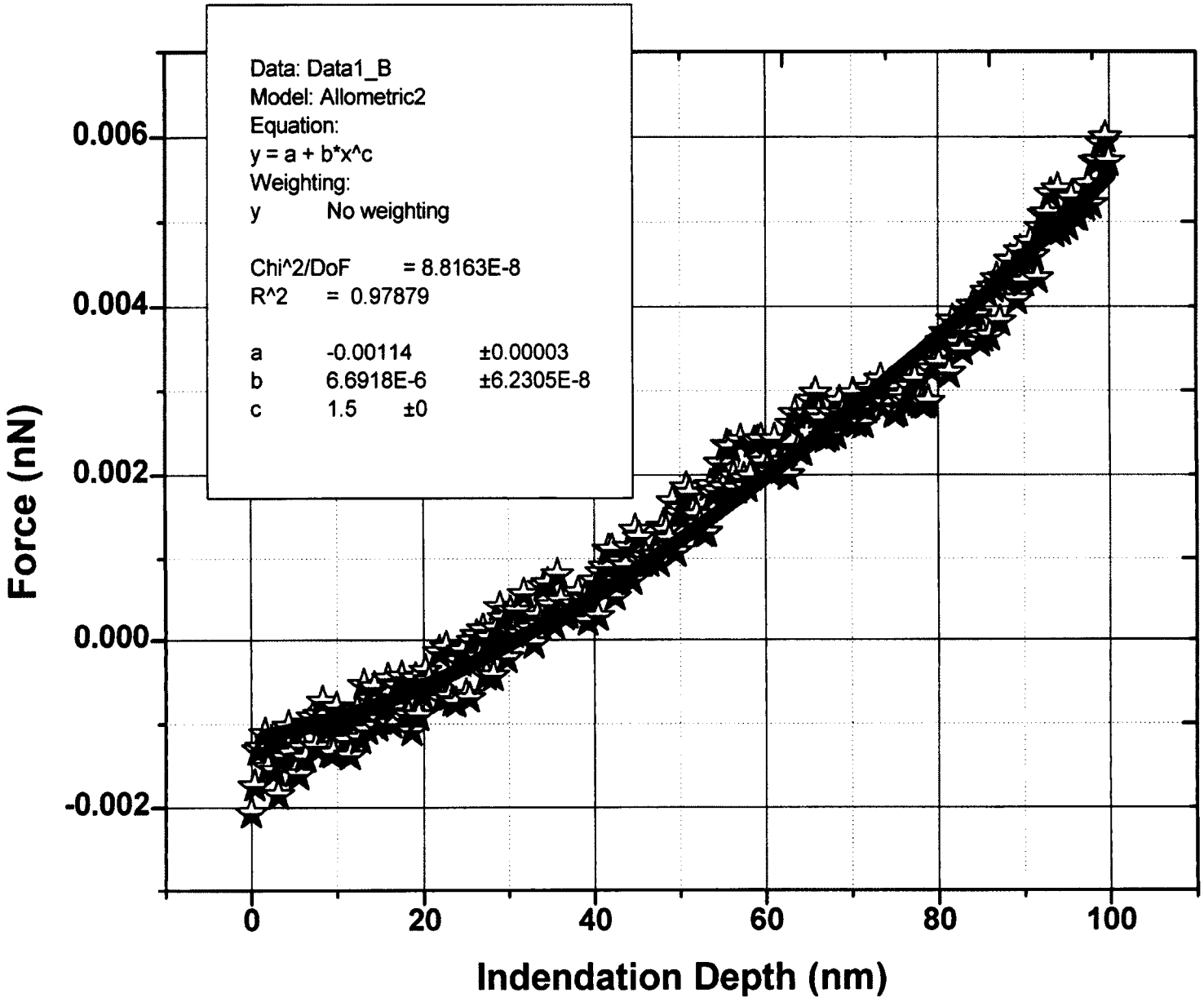

Figure 4.7: Nano-indentation experiment data on pulsed Jurkat cell (60 kv/cm) and fitted with DMT Model.

Table 4.3 below shows experimental values and model fits. Pulsed Jurkat cells (60 Kv/cm) modulus of elasticity is about 1.09 KPa for the DMT model and 1.20 KPa for Hertz model. The modulus of elasticity is reduced for pulsed cells compared to non-pulsed cells.

Table 4.3: Pulsed Jurkat cells (60 kv/cm) modulus of elasticity values at different experiments.

	DMT (KPa)
Exp 1	1.06
Exp 2	0.711
Exp 3	1.50
Average	1.09033 (±0.39537)

All three nano indentation curves are shown in Figure 4.8. We found a 53% decrease in the Young's modulus when Jurkat cells were exposed to 15 kV/cm. However, the application of a 60 kV/cm nsPEF resulted in an 85% decrease of the Young's modulus at the maximum indentation depth when compared to 0 kV/cm. Figure 4.9 shows Young's modulus in cells pulsed for 60 ns at 0, 15, and 60 kV/cm.

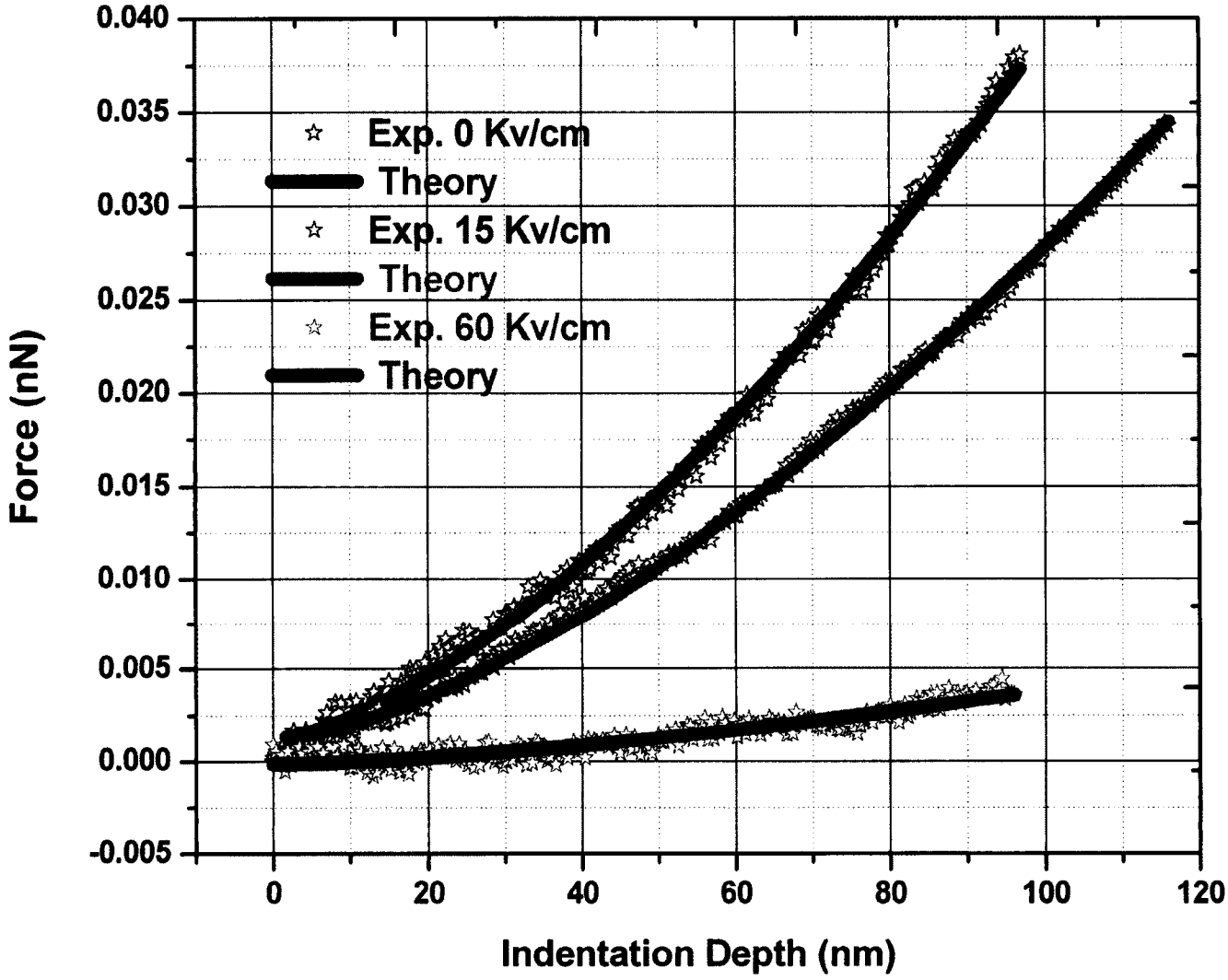

Figure 4.8: Comparison of all 3 nano indentation measurements between AFM probe and Jurkat cells.

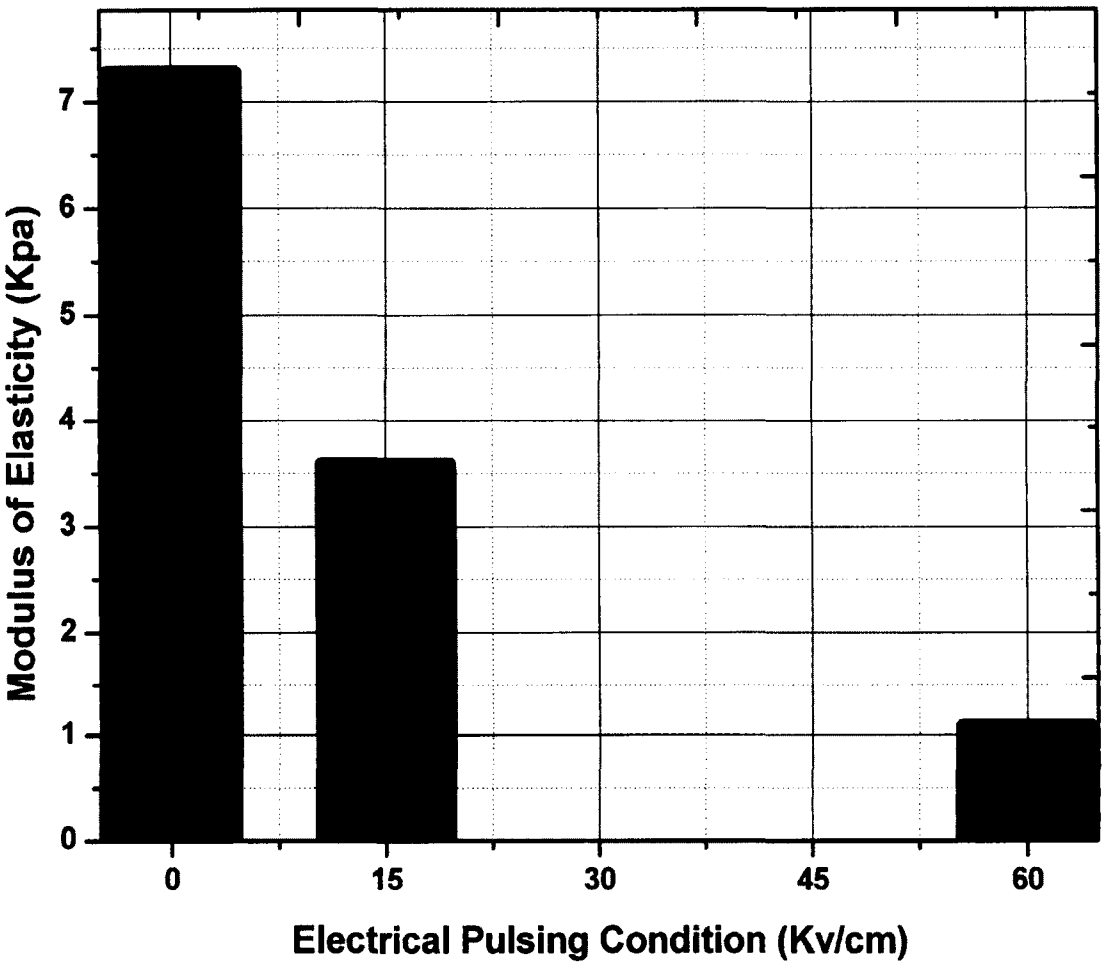

Figure 4.9: Young's modulus in cells pulsed for 60 ns at 0, 15, and 60 kV/cm (n = 3 for all conditions).

4.4 Surface Charge Density Mapping

We next considered the electrostatic force between the AFM tip and the cell surface. The electrostatic force to be encountered is represented by the equation below, which is based on prior work by Parsegia et al. [203].

$$F_{EDL} = \frac{2\pi R\lambda_D}{\varepsilon\varepsilon_0}\left[2\sigma_s\sigma_t e^{-x/\lambda_D} + (\sigma_s^2 + \sigma_t^2)e^{-2x/\lambda_D}\right] \tag{4.3}$$

R is the AFM tip radius, ε is the dielectric constant of the medium, ε_0 is the vacuum permittivity, σ_s surface charge density of sample, σ_t surface charge density of tip and λ_D is the Debye length, which can be written in the following equation

$$\lambda_D = \sqrt{\frac{\varepsilon\varepsilon_0 k_B T}{2ce^2}} \tag{4.4}$$

k_B is the Boltzmann constant, T is the temperature, c is the concentration and e is the charge.

An algorithm, based on the least square fitting method, was developed to compute the biological cells' and AFM probe's surface charge density. The experimental data was fitted with Equation 1 using our Matlab code. Equation 3 has two fitting parameters; one is the AFM probe charge density and the second is the cells' surface charge density. A student's t-test was used for statistical analysis, with a p value of <0.05 indicating a significant result.

4.5 Results

NsPEFs are known to create nanopores when applied to cell membranes, and this phenomenon has been extensively studied computationally and experimentally with regards to the size, density, and lifespan of the pores. However, the membrane and cytoskeletal integrity of the cells, post-exposure to high energy/ low duration electrical fields, is not well documented.

AFM and NSOM were used in our study to visualize morphological changes caused by applying the differing NsPEFs (Figure 4.10). Pore formation can generate many changes, but the cytoskeleton is likely to be affected as well in order for such drastic changes to have occurred to the cells' morphology. We had to test the applicability of the electrostatic force theory with force distance curves as used by AFM; to do this we developed our own Matlab code to fit the theory and experimentally tested this through measurements of the surface force between the AFM tip and the control silica surface within a 0.01 M KCl solution. This match is exhibited in Equation 4.3 and the results can be seen in Figure 4.11 along with the fitting of theoretical results. From these results, the Debye length was independently computed with the use of Equation 4.4. During the

AFM probe's approach to silica through all electrical pulsing conditions, continuously increasing repulsive forces were constantly observed which were found to be a result of similarly charged particles meeting. The surface charge density of Jurkat cells at 0, 15 and 60 kV/cm in 0.01 M KCL solution was -0.00852 (±0.00671) C/cm^2, -0.00159 (±0.00195) C/cm^2 and 0.00216 (±0.00043) C/cm^2.

The 0 kV/cm case can be taken as the control. In comparison, an 81% decrease in the charge density was found when Jurkat cells were exposed to a field strength of 15 kV/cm (Figure 4.16); this was overshadowed by a starker change as was seen through a 125% decrease in the charge density at surface force measurements through the application of a 60 kV/cm field strength NsPEF (Figure 4.16).

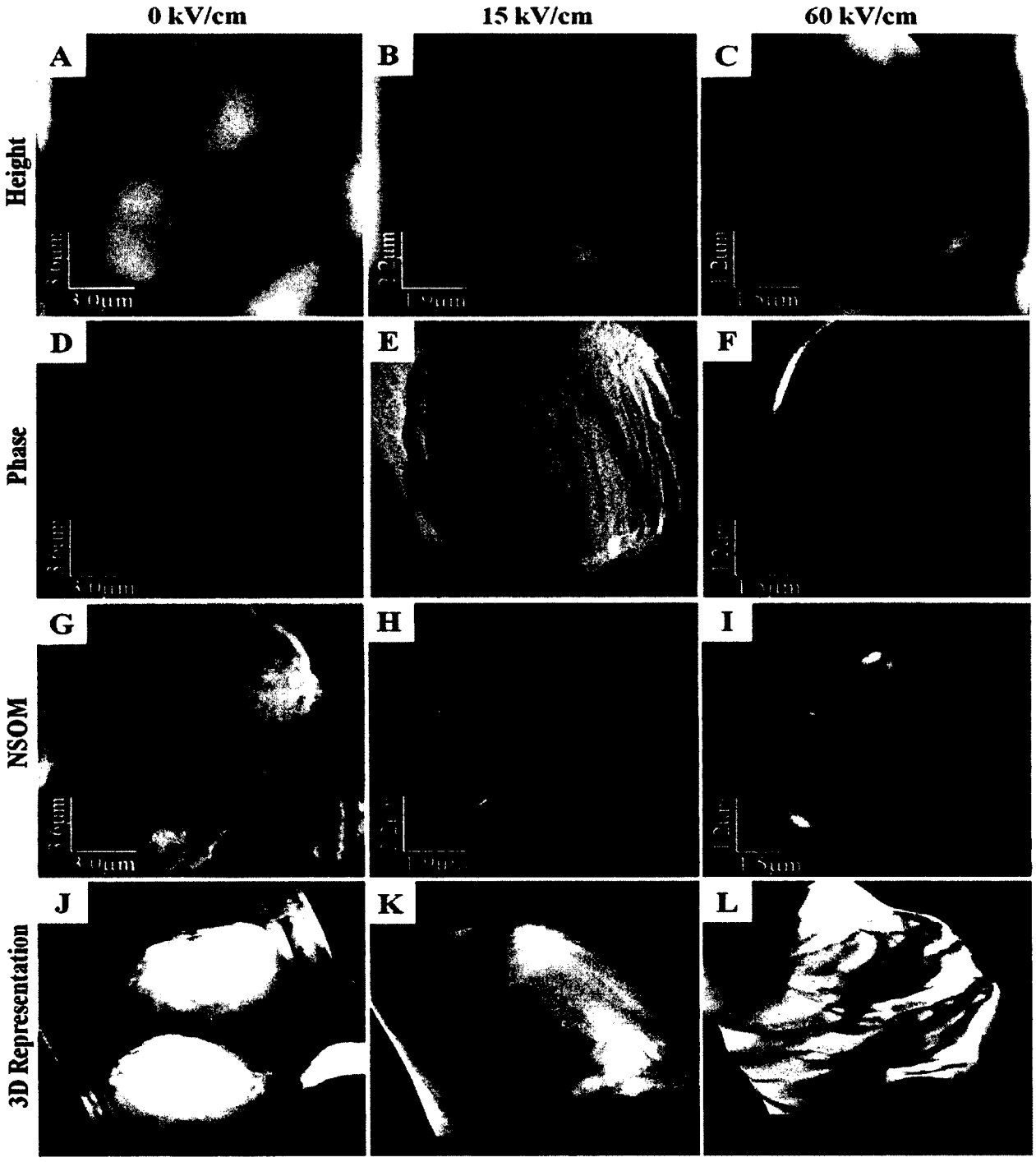

Figure 4.10: Atomic Force Microscopy (AFM) and near-field scanning optical microscopy (NSOM) of Jurkat cells exposed to nanosecond pulsed electric fields (nsPEFs). (A-C) AFM height images of cells exposed to 0, 15, and 60 kV/cm nsPEFs, respectively. (D-F) AFM phase images of Jurkat cells exposed to 0, 15, and 60 kV/cm nsPEFs, respectively. (G-I) NSOM images of Jurkat cells exposed to 0, 15, and 60 kV/cm nsPEFs, respectively. (J-L) Three-dimensional representations based on AFM height measurements of Jurkat cells exposed to 0, 15, and 60 kV/cm nsPEFs, respectively.

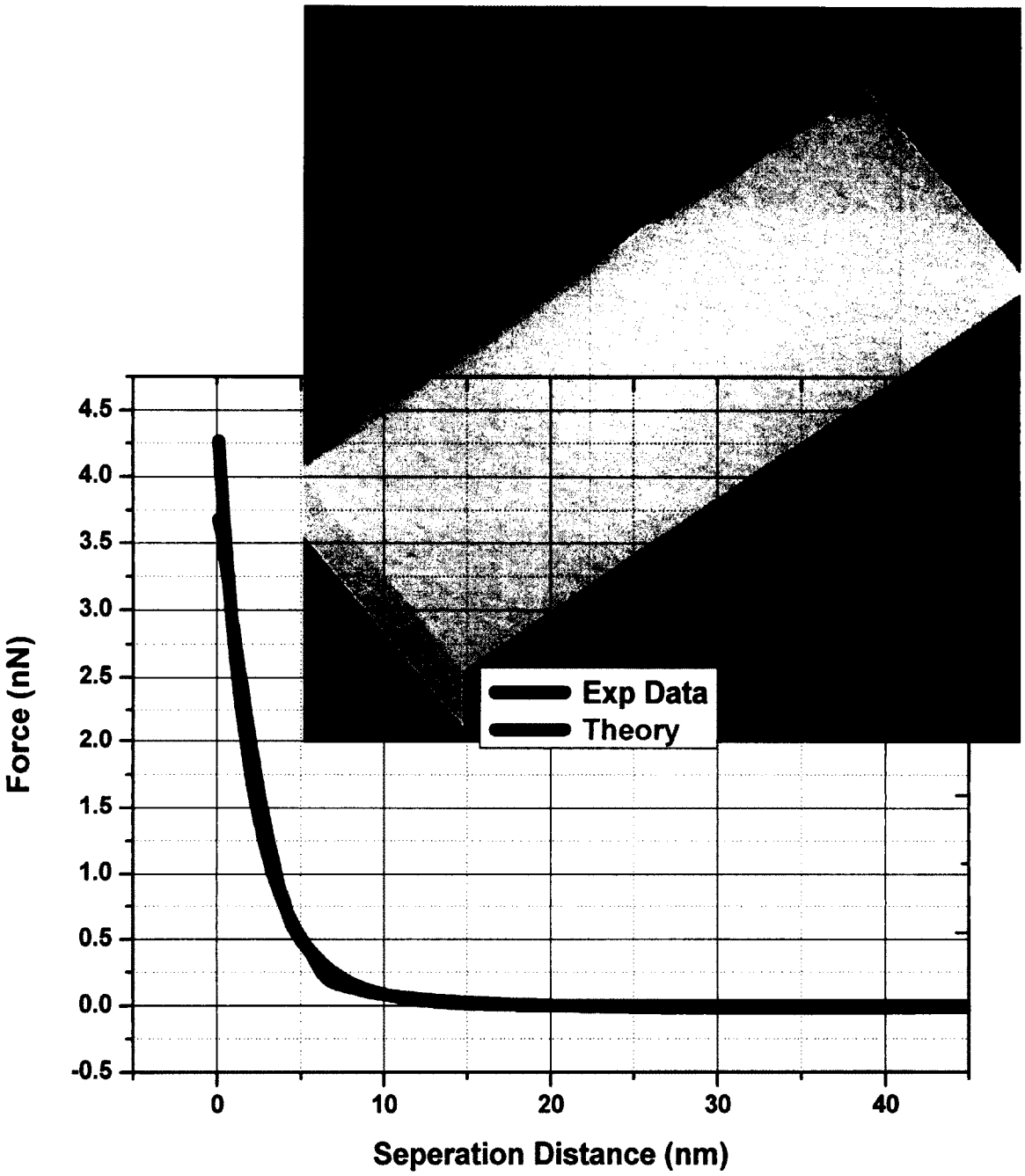

Figure 4.11: Surface force measurements between AFM probe and silica in 0.01 M KCL solution.

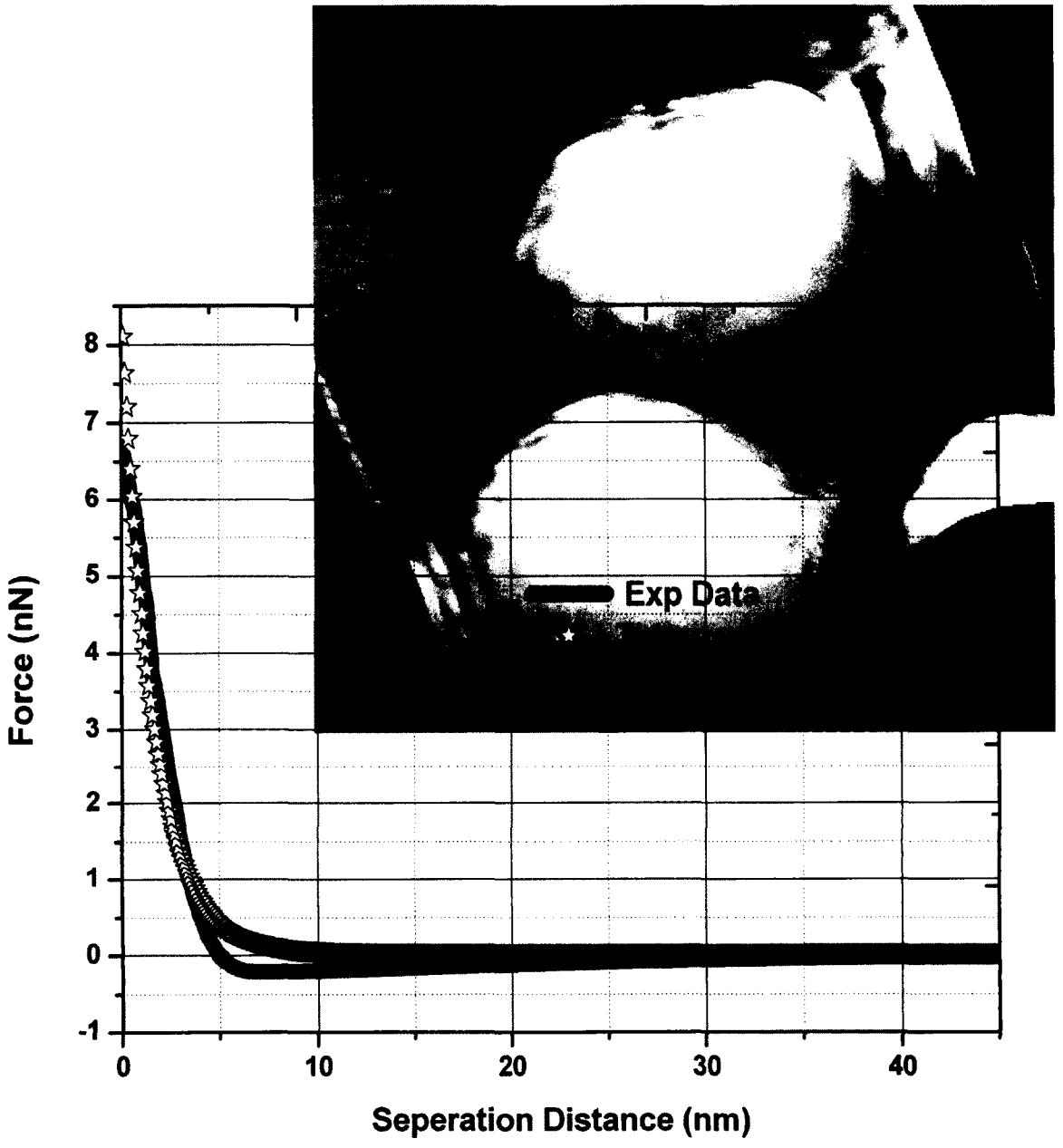

Figure 4.12: Surface force measurements between AFM probe and Jurkat cells (0 Kv/cm).

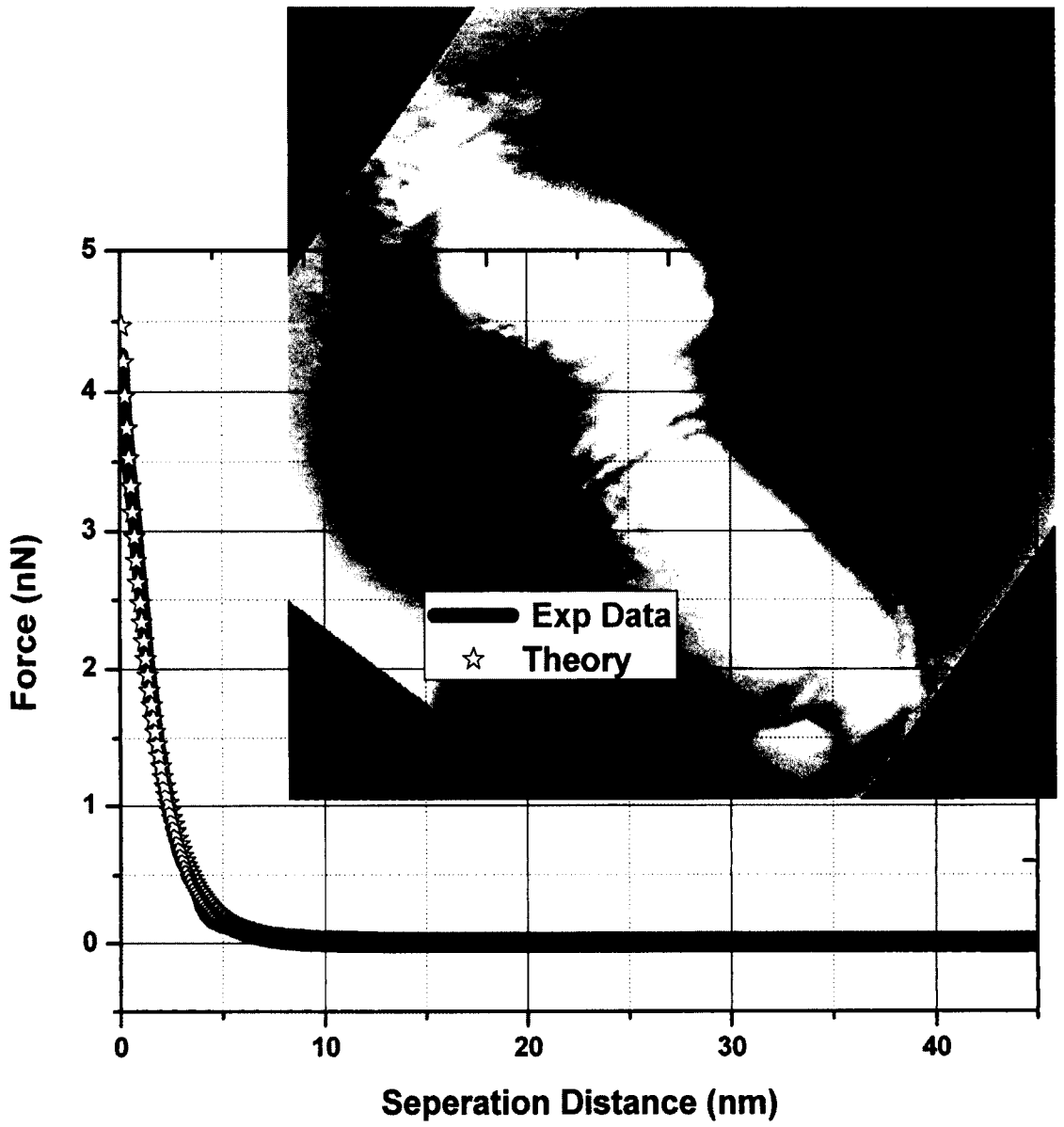

Figure 4.13: Surface force measurements between AFM probe and Jurkat cells (15 Kv/cm).

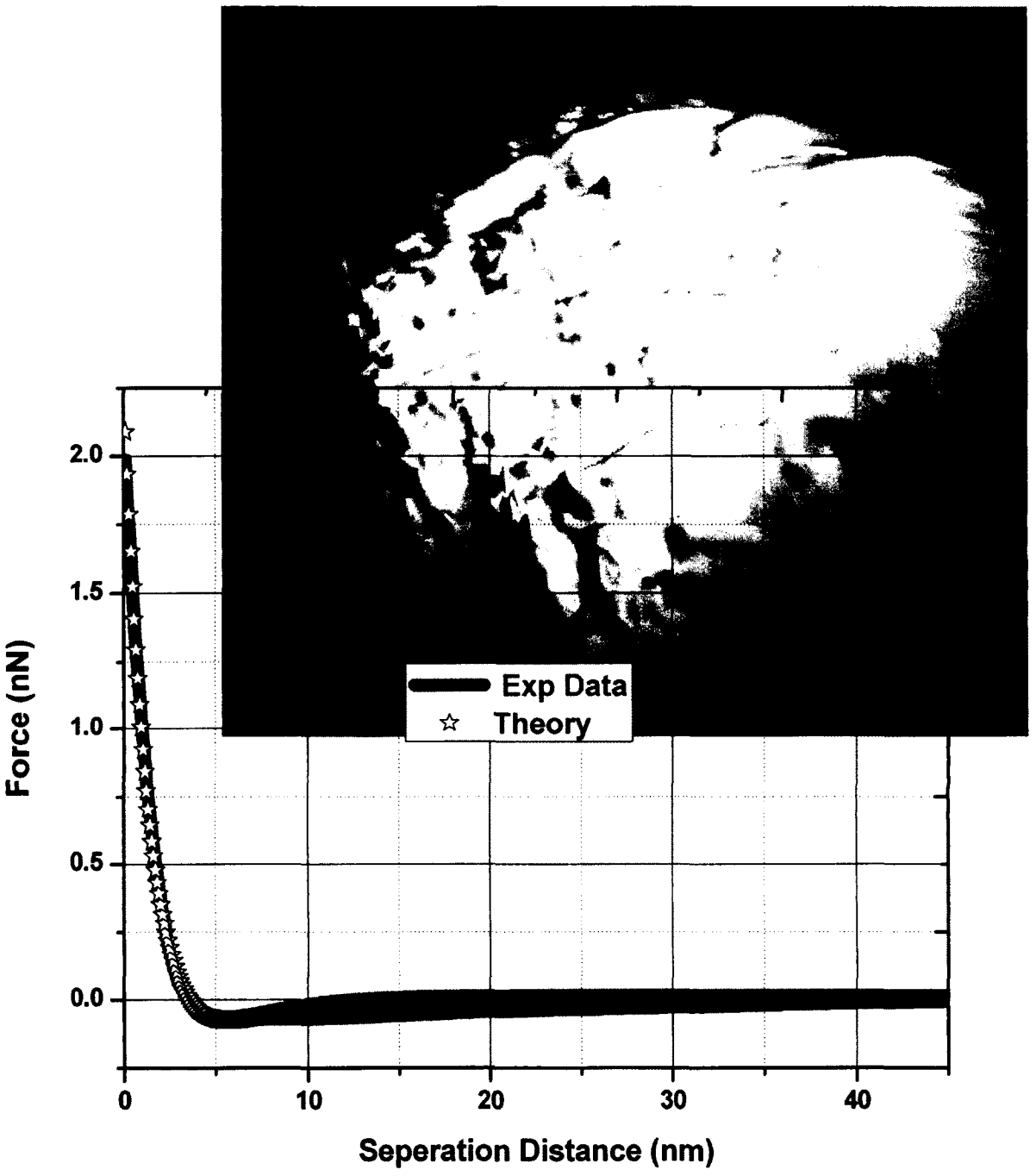

Figure 4.14: Surface force measurements between AFM probe and Jurkat cells (60Kv/cm).

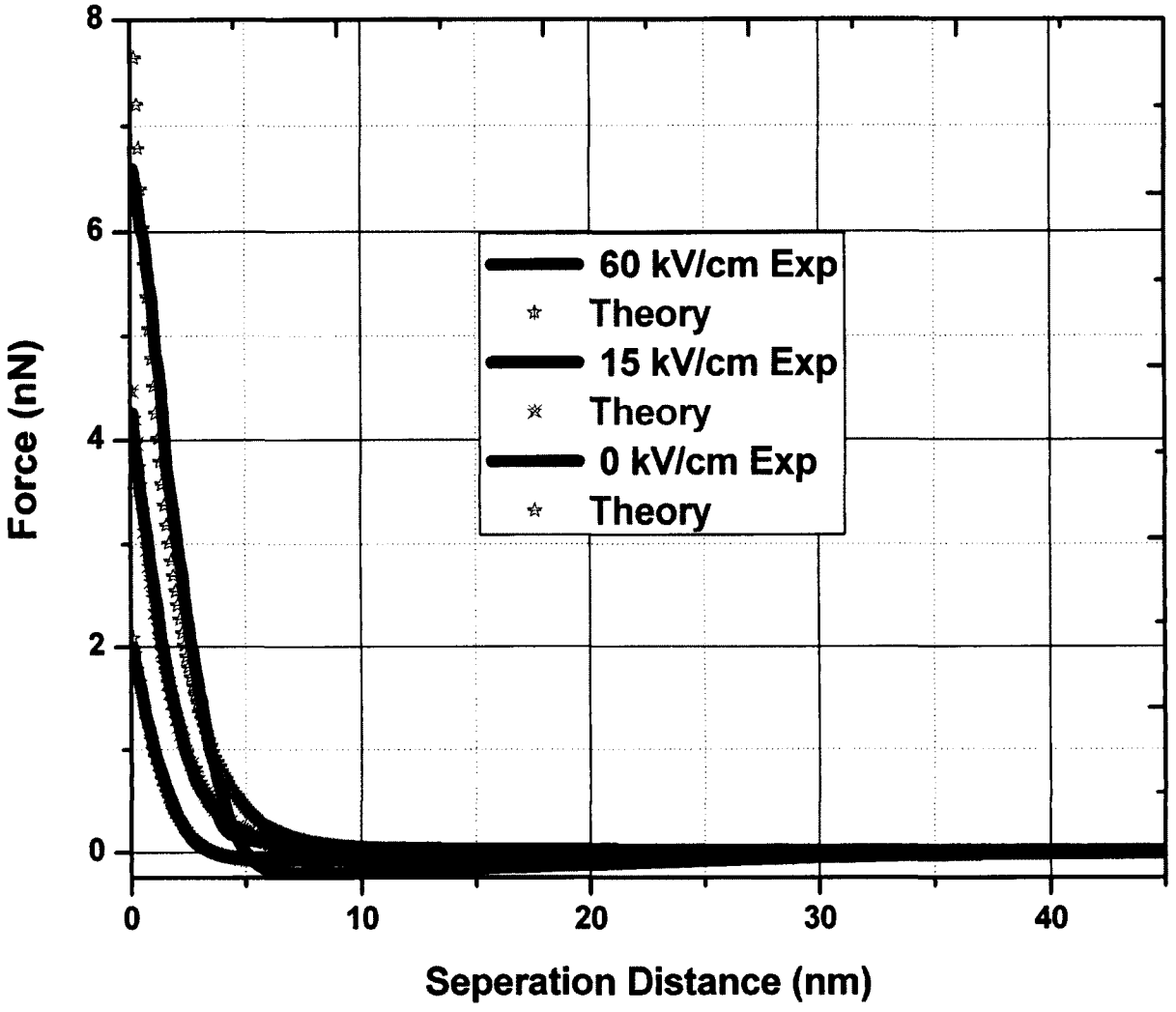

Figure 4.15: Comparison of all 3 surface force measurements between AFM probe and Jurkat cells.

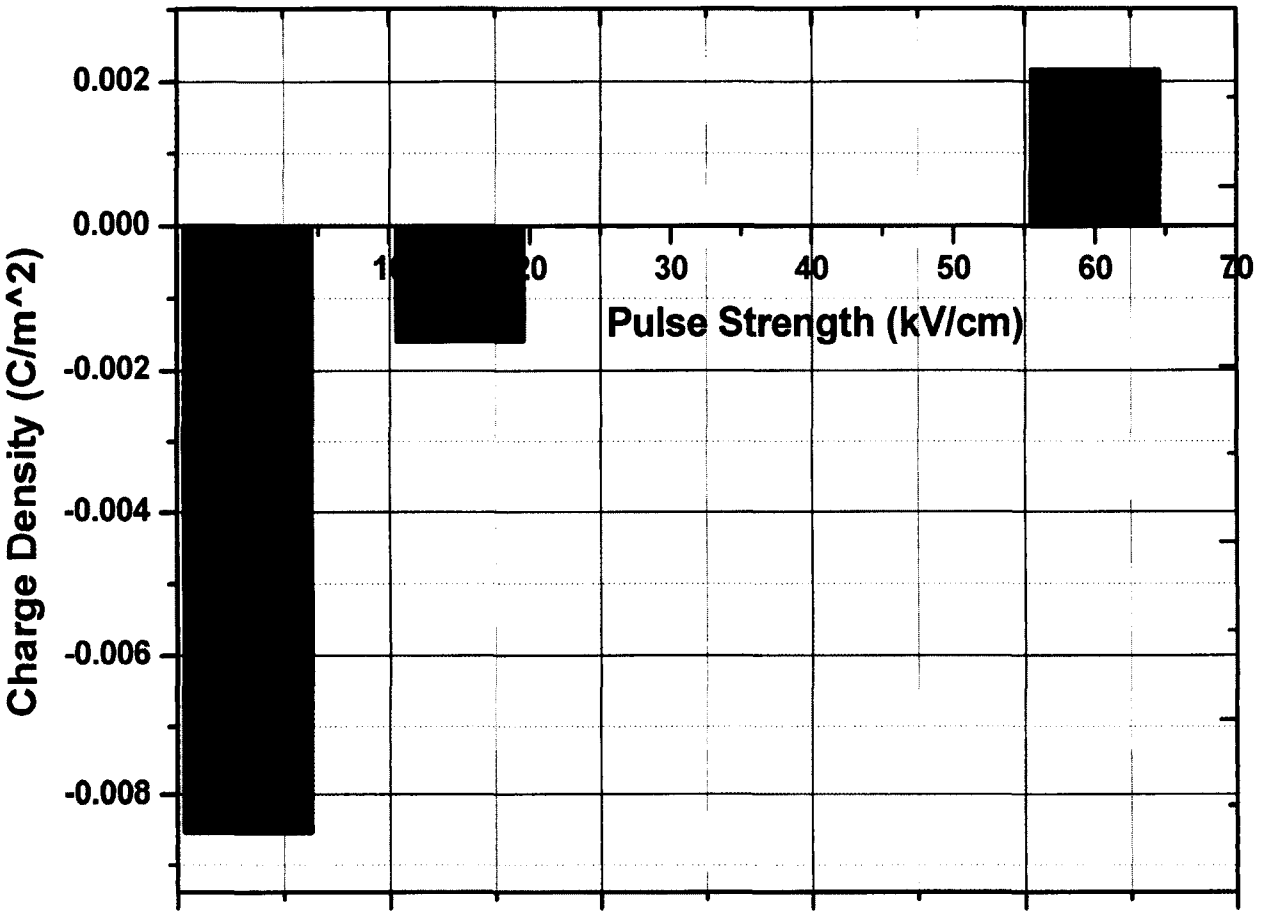

Figure 4.16: Surface charge density measurements in cells pulsed for 60 ns at 0, 15, and 60 kV/cm (n = 3 for all conditions).

4.6 Discussion

In this study, we explored how NsPEFs influence cellular morphology, surface charge density, and elasticity, through the use of AFM. NSOM was used to image the cellular morphology and was complimented through the inclusion of height and phase imaging through AFM.

The AFM was our main investigational tool due to its ability to image and measure interaction forces between the tip and the cell. This allowed us to infer that highly hydrophobic cells have a large negatively charged surface density that differed under different electrical pulsing conditions. Jurkat cells are an immortalized line of human T-lymphocytes that were chosen due to their ability to grow in a suspension as well as their round morphology, which allows for ease in observing morphological changes; small changes could easily be observed within them post-stress as shown through exposure to a low field strength NsPEF which gave the cells more oval morphology. This finding is significant in that it highlights a strength of AFM in its ability to detect these changes wherein simple staining could not; it was demonstrated in Figure 1E in Dutta et al. [204] that phalloidin staining failed to show significant changes in actin cytoskeletal morphology under low strength NsPEF exposure even though the cell's elasticity was reduced by 53%. In contrast, high field strength NsPEFs were able to affect the cellular morphology drastically, through disrupting the actin cytoskeleton and reducing the elasticity another 22% more than that achieved with the low field strength NsPEF. It is possible that the extensive morphological and charge density changes across the cell surface, as well as the elasticity changes caused by the high field strength NsPEFs, are

due to depolymerization and disruption of the organization of the actin filaments and the cell cortex.

In conclusion, our data demonstrate that NsPEFs significantly change the cell membrane through changes in membrane elasticity and surface charge density. Low field strength NsPEFs generated a significant change in membrane elasticity and charge density, but an insignificant change in cell morphology. High field strength NsPEFs generated a significant change in membrane elasticity, surface charge density and cell morphology. Under both NsPEF regimes, surface charge density increased, but this occurred more with the high field strength NsPEF. The observed effects seem to be a result of long lasting permeabilization of the membrane of the cells that were fixed immediately after the NsPEF pulsing which generated potentially irreversible effects that depend on the cytoskeleton to some degree. The membrane interfaces with, and owes it stability to, the cytoskeleton, which would disrupt the membrane if it itself was destabilized as was the case with high field strength NsPEFs (Figure 1L). This work is supported by our prior findings which describe the relationship of actin destabilization and reduced cell survival [160]. All of this was accomplished through AFM, allowing for the visualization and testing of the effect destabilization of the actin cytoskeleton on the morphological changes as induced though differing regimes of NsPEF pulsing.

CHAPTER 5

CONCLUSIONS

In this dissertation, I used AFM as a primary tool for nano scale imaging, nano-indentation, surface charge potential and density mapping, as well as interfacial force measurements. AFM imaging was done in both air and liquid environments with short and long probes. The long probe was made by attaching a long needle at the end of the cantilever used. Both types of probes were also used for nano-indentation experiments, and long probes were used for interfacial force measurements. By using AFM, I have done nano indentation on PDMS, human costal cartilage in both ambient and PBS buffer conditions, and pulsed and non-pulsed Jurkat cells. Interfacial forces have been measured between an AFM nano probe and silica surface under different ionic concentrations. Van der Waals forces were also investigated between the AFM nano probe and silica surface within DI water. Nano scale AFM imagings were performed on silica surfaces, human costal cartilage samples with different chemical treatments in both ambient and PBS buffer conditions, and pulsed and non pulsed Jurkat cells.

Human costal cartilage samples were extracted from a patient. These samples were chemically treated and fixed over poly lysine cover slips. Six different sets of data show different P values that came from ANOVA tests performed on the samples. Two different sets of data are statistically different from each other, when P value is less than 0.005. The largest mean diameter of collagen nanostraws was 524 nm for digested and homogenized fixed samples in air, and the smallest mean diameter of collagen nanostraws was 331 nm for digested and homogenized unfixed samples in PBS buffer.

These diameter variations of different types of samples are due to chemical treatment. Hence, fluid flow through these collagen nanostraws can affect transport phenomena.

The AFM nano-indenter was applied to the above collagen nanostraws in environmental and PBS buffer conditions. The indenter was indented in various sample surfaces with very small deformation and from this deformation we can extract materials' properties. This nanoindenter technique was so powerful that it was able to sense pico-newton level force with exact nanometer scale positioning. The cartilage samples studied were abundant in type 11 collagen. In air, the collagen nanostraws' modulus of elasticity was higher due to protein cross linking. In PBS buffer, collagen nanostraws' magnitude of mechanical properties was lower than that in air because fluid was passing through these nanostraws.

A cancerous line of white blood cells called Jurkat cells were studied via AFM. Cancer cells' morphology and mechanical properties are different from those of healthy cells. AFM can discover each local change at each cellular layer. The Cancer cell's membrane can be broken down by using either electric pulsing or drugs. Jurkat cells were treated with nano second electrical pulsing at different conditions. At first, I performed AFM topography images for non pulsed Jurkat cells. From the cells' height profile, they are about 8-12 microns in diameter. When nano-indenter techniques were applied, these cells went through small deformation. I have extracted global mechanical properties using the Matlab program; local mechanical properties were also extracted at every indentation depth. The non pulsed Jurkat cells' Young modulus of elasticity was 7.27667 (±1.070) KPa. In this experimental case, the indentation depth was 100 nm, and the maximum

force was about 40 pN. Cells were pulsed in two different conditions; one was 15 Kv/cm and another one was 60 Kv/cm. In each condition, AFM scanning was performed on these pulsed cells. From AFM topography and morphology images, we can see the change of the cell's membrane at nanometer scale. The pulsed cell's membrane was broken down due to the electrical pulsing; consequently, their local mechanical properties changed at each condition. For the case of 15 Kv/cm, the Jurkat cells' modulus of elasticity was 3.82 (±1.682) KPa. In this case, the maximum force was 35 pN, and the indentation depth was 120 nm. For the case of 60 Kv/cm, the Jurkat cells' modulus of elasticity was 1.20667 (±0.49662) KPa. In this case, the maximum force was 6 pN, and the indentation depth was 100 nm. From AFM images, we can see that pulsed and non pulsed cells' topography images were not the same.

Bioelectrochemical analyses on Cancer cells were also performed with AFM in salt concentrations. Cells were electrically pulsed in different pulsing conditions. Before measuring interfacial force, we imaged these cells and observed morphological change in three different conditions. After that, force versus separation distance measurements were performed in physiological conditions. These experimental curves were fitted with the DLVO theory. The magnitude of the force decreased as electrical pulsing intensity increased due to the cells' membrane and cytoskeleton break down. The surface charge mapping shows an 81% reduction of charge density in 15 kV/cm pulsing conditions and a 125% reduction of charge density in 60 kV/cm pulsing conditions.

Nano & micron size particles were attached at the end of the nano-needle of the AFM probe for surface force measurements between an AFM probe and silica surface in different ionic concentrations. The experimental results were fitted with the DLVO theory to determine the surface charge densities of the interacting objects. We are able to measure pN level force in solutions at 50 nm separation distance. Our experimental results are in qualitative agreement with the theory at different ionic concentrations. The surface charge density increases with an increase in the ionic concentration. This AFM unique tool was also used to measure materials' local properties like the Hamakar constant. The surface forces were measured between AFM nano tip and silica surface in DI water. The experimental results were in very good agreement with the Van Der Waals theory. Hamaker constant was determined from these experimental results.

REFERENCES

[1] G. Binnig, C. F. Quate, and C. Gerber, "Atomic Force Microscope," *Physical Review Letters,* vol. 56, pp. 930-933, Mar 3 1986.

[2] M. Alderighi, V. Ierardi, F. Fuso, M. Allegrini, and R. Solaro, "Size effects in nanoindentation of hard and soft surfaces," *Nanotechnology,* vol. 20, Jun 10 2009.

[3] J. Ren, S. Y. Yu, N. Gao, and Q. Z. Zou, "Indentation quantification for in-liquid nanomechanical measurement of soft material using an atomic force microscope: Rate-dependent elastic modulus of live cells," *Physical Review E,* vol. 88, Nov 18 2013.

[4] Y. X. Zhu, Z. X. Dong, U. C. Wejinya, S. Jin, and K. M. Ye, "Determination of mechanical properties of soft tissue scaffolds by atomic force microscopy nanoindentation," *Journal of Biomechanics,* vol. 44, pp. 2356-2361, Sep 2 2011.

[5] S. R. Cohen and E. Kalfon-Cohen, "Dynamic nanoindentation by instrumented nanoindentation and force microscopy: a comparative review," *Beilstein Journal of Nanotechnology,* vol. 4, pp. 815-833, Nov 29 2013.

[6] A. San Paulo and R. Garcia, "Amplitude, deformation and phase shift in amplitude modulation atomic force microscopy: a numerical study for compliant materials," *Surface Science,* vol. 471, pp. 71-79, Jan 10 2001.

[7] Y. Martin, C. C. Williams, and H. K. Wickramasinghe, "Atomic Force Microscope Force Mapping and Profiling on a Sub 100-a Scale," *Journal of Applied Physics,* vol. 61, pp. 4723-4729, May 15 1987.

[8] M. L. Shuler and J. H. Sung, "Introduction to the Special Issue on Micro- and Nanofabrication Techniques," *Annals of Biomedical Engineering,* vol. 40, pp. 1209-1210, Jun 2012.

[9] R. Garcia and A. San Paulo, "Attractive and repulsive tip-sample interaction regimes in tapping-mode atomic force microscopy," *Physical Review B,* vol. 60, pp. 4961-4967, Aug 15 1999.

[10] B. Anczykowski, D. Kruger, and H. Fuchs, "Cantilever dynamics in quasinoncontact force microscopy: Spectroscopic aspects," *Physical Review B,* vol. 53, pp. 15485-15488, Jun 15 1996.

[11] D. Rugar and P. Hansma, "Atomic Force Microscopy," *Physics Today,* vol. 43, pp. 23-30, Oct 1990.

[12] C. B. Prater, H. J. Butt, and P. K. Hansma, "Atomic Force Microscopy," *Nature,* vol. 345, pp. 839-840, Jun 28 1990.

[13] T. Fujii, H. Yamada, and K. Nakayama, "Atomic Force Microscopy," *Journal of Electron Microscopy,* vol. 39, pp. 197-197, Jun 1990.

[14] G. Bar, Y. Thomann, R. Brandsch, H. J. Cantow, and M. H. Whangbo, "Factors affecting the height and phase images in tapping mode atomic force microscopy. Study of phase-separated polymer blends of poly(ethene-co-styrene) and poly(2,6-dimethyl-1,4-phenylene oxide)," *Langmuir,* vol. 13, pp. 3807-3812, Jul 9 1997.

[15] R. S. McLean and B. B. Sauer, "Tapping-mode AFM studies using phase detection for resolution of nanophases in segmented polyurethanes and other block copolymers," *Macromolecules,* vol. 30, pp. 8314-8317, Dec 29 1997.

[16] C. L. Cheung, J. H. Hafner, and C. M. Lieber, "Carbon nanotube atomic force microscopy tips: Direct growth by chemical vapor deposition and application to high-resolution imaging," *Proceedings of the National Academy of Sciences of the United States of America,* vol. 97, pp. 3809-3813, Apr 11 2000.

[17] D. Klinov and S. Magonov, "True molecular resolution in tapping-mode atomic force microscopy with high-resolution probes," *Applied Physics Letters,* vol. 84, pp. 2697-2699, Apr 5 2004.

[18] J. Martinez, T. D. Yuzvinsky, A. M. Fennimore, A. Zettl, R. Garcia, and C. Bustamante, "Length control and sharpening of atomic force microscope carbon nanotube tips assisted by an electron beam," *Nanotechnology,* vol. 16, pp. 2493-2496, Nov 2005.

[19] E. S. Snow, P. M. Campbell, and J. P. Novak, "Single-wall carbon nanotube atomic force microscope probes," *Applied Physics Letters,* vol. 80, pp. 2002-2004, Mar 18 2002.

[20] T. E. Schaffer, "Calculation of thermal noise in an atomic force microscope with a finite optical spot size," *Nanotechnology,* vol. 16, pp. 664-670, Jun 2005.

[21] S. Vahabi, B. Nazemi Salman, and A. Javanmard, "Atomic force microscopy application in biological research: a review study," *Iran J Med Sci,* vol. 38, pp. 76-83, Jun 2013.

[22] F. J. Giessibl, "Advances in atomic force microscopy," *Reviews of Modern Physics,* vol. 75, pp. 949-983, Jul 2003.

[23] D. J. Muller, "AFM: a nanotool in membrane biology," *Biochemistry,* vol. 47, pp. 7986-7998, Aug 5 2008.

[24] F. Variola, "Atomic force microscopy in biomaterials surface science," *Physical Chemistry Chemical Physics,* vol. 17, pp. 2950-2959, 2015.

[25] M. Stolz, R. Raiteri, A. U. Daniels, M. R. VanLandingham, W. Baschong, and U. Aebi, "Dynamic elastic modulus of porcine articular cartilage determined at two different levels of tissue organization by indentation-type atomic force microscopy," *Biophysical Journal,* vol. 86, pp. 3269-3283, May 2004.

[26] A. J. Heim, T. J. Koob, and W. G. Matthews, "Low strain nanomechanics of collagen fibrils," *Biomacromolecules,* vol. 8, pp. 3298-3301, Nov 2007.

[27] A. J. Heim, W. G. Matthews, and T. J. Koob, "Determination of the elastic modulus of native collagen fibrils via radial indentation," *Applied Physics Letters,* vol. 89, Oct 30 2006.

[28] L. Yang, K. O. Van der Werf, C. F. C. Fitie, M. L. Bennink, P. J. Dijkstra, and J. Feijen, "Mechanical properties of native and cross-linked type I collagen fibrils," *Biophysical Journal,* vol. 94, pp. 2204-2211, Mar 15 2008.

[29] L. Yang, C. F. C. Fitie, K. O. van der Werf, M. L. Bennink, P. J. Dijkstra, and J. Feijen, "Mechanical properties of single electrospun collagen type I fibers," *Biomaterials,* vol. 29, pp. 955-962, Mar 2008.

[30] M. Stacey, D. Dutta, W. Cao, A. Asmar, H. Elsayed-Ali, R. Kelly, *et al.*, "Atomic force microscopy characterization of collagen 'nanostraws' in human costal cartilage," *Micron,* vol. 44, pp. 483-487, Jan 2013.

[31] M. P. E. Wenger, L. Bozec, M. A. Horton, and P. Mesquida, "Mechanical properties of collagen fibrils," *Biophysical Journal,* vol. 93, pp. 1255-1263, Aug 2007.

[32] D. J. Taatjes, B. E. Sobel, and R. C. Budd, "Morphological and cytochemical determination of cell death by apoptosis," *Histochemistry and Cell Biology,* vol. 129, pp. 33-43, Jan 2008.

[33] S. Suresh, "Nanomedicine - Elastic clues in cancer detection," *Nature Nanotechnology,* vol. 2, pp. 748-749, Dec 2007.

[34] S. Suresh, J. Spatz, J. P. Mills, A. Micoulet, M. Dao, C. T. Lim, *et al.*, "Connections between single-cell biomechanics and human disease states: gastrointestinal cancer and malaria," *Acta Biomaterialia,* vol. 1, pp. 15-30, Jan 2005.

[35] Q. S. Li, G. Y. Lee, C. N. Ong, and C. T. Lim, "AFM indentation study of breast cancer cells," *Biochem Biophys Res Commun,* vol. 374, pp. 609-13, Oct 3 2008.

[36] M. Labardi, P. G. Gucciardi, and M. Allegrini, "Force gradient versus distance curves studied by atomic force microscopy," *Micro/Nanotribology and Its Applications,* vol. 330, pp. 129-134, 1997.

[37] M. M. Islam, M. T. Alam, and T. Ohsaka, "Electrical Double-Layer Structure in Ionic Liquids: A Corroboration of the Theoretical Model by Experimental Results," *Journal of Physical Chemistry C,* vol. 112, pp. 16568-16574, Oct 2008.

[38] W. A. Ducker, T. J. Senden, and R. M. Pashley, "Measurement of Forces in Liquids Using a Force Microscope," *Langmuir,* vol. 8, pp. 1831-1836, Jul 1992.

[39] Y. Q. Li, N. J. Tao, J. Pan, A. A. Garcia, and S. M. Lindsay, "Direct Measurement of Interaction Forces between Colloidal Particles Using the Scanning Force Microscope," *Langmuir,* vol. 9, pp. 637-641, Mar 1993.

[40] M. Prica, S. Biggs, F. Grieser, and T. W. Healy, "Effect of calcination temperature on the electrokinetic properties of colloidal zirconia," *Colloids and Surfaces a-Physicochemical and Engineering Aspects,* vol. 119, pp. 205-213, Dec 16 1996.

[41] S. Veeramasuneni, M. R. Yalamanchili, and J. D. Miller, "Measurement of interaction forces between silica and alpha-alumina by atomic force microscopy," *Journal of Colloid and Interface Science,* vol. 184, pp. 594-600, Dec 25 1996.

[42] S. Veeramasuneni, M. R. Yalamanchili, and J. D. Miller, "Interactions between dissimilar surfaces in high ionic strength solutions as determined by atomic force microscopy," *Colloids and Surfaces a-Physicochemical and Engineering Aspects,* vol. 131, pp. 77-87, Jan 1 1998.

[43] K. Hu and A. J. Bard, "Characterization of adsorption of sodium dodecyl sulfate on charge-regulated substrates by atomic force microscopy force measurements," *Langmuir,* vol. 13, pp. 5418-5425, Oct 1 1997.

[44] Y. Kanda, T. Nakamura, and K. Higashitani, "AFM studies of interaction forces between surfaces in alcohol-water solutions," *Colloids and Surfaces a-Physicochemical and Engineering Aspects,* vol. 139, pp. 55-62, Jul 31 1998.

[45] C. J. Chin, S. Yiacoumi, and C. Tsouris, "Influence of metal ion sorption on colloidal surface forces measured by atomic force microscopy," *Environmental Science & Technology,* vol. 36, pp. 343-348, Feb 1 2002.

[46] A. V. Nguyen, J. Nalaskowski, and J. D. Miller, "A study of bubble-particle interaction using atomic force microscopy," *Minerals Engineering,* vol. 16, pp. 1173-1181, Nov 2003.

[47] P. D. I. Fletcher, "Some new directions in colloid science," *Self-Assembly,* pp. 3-10, 2003.

[48] J. Lyklema, "Fundamentals of Interface and Colloid Science, Vol IV: Particulate Colloids," *Fundamentals of Interface and Colloid Science, Vol Iv: Particulate Colloids,* vol. 4, pp. 1-654, 2005.

[49] J. Klein, "Forces between Mica Surfaces Bearing Adsorbed Macromolecules in Liquid-Media," *Journal of the Chemical Society-Faraday Transactions I,* vol. 79, pp. 99-&, 1983.

[50] J. L. Parker, P. M. Claesson, J. H. Wang, and H. K. Yasuda, "Surface Forces between Plasma Polymer-Films," *Langmuir,* vol. 10, pp. 2766-2773, Aug 1994.

[51] J. L. Parker, H. K. Christenson, and B. W. Ninham, "Device for Measuring the Force and Separation between 2 Surfaces down to Molecular Separations," *Review of Scientific Instruments,* vol. 60, pp. 3135-3138, Oct 1989.

[52] D. Tabor and R. H. Winterton, "Surface forces: direct measurement of normal and retarded van der Waals forces," *Nature,* vol. 219, pp. 1120-1, Sep 14 1968.

[53] B. G. Samojla, "Surface Tendon Force Measurements in Determining Muscle-Contraction Properties," *Journal of the American Podiatric Medical Association,* vol. 78, pp. 1-10, Jan 1988.

[54] L. R. Dix, C. Toprakcioglu, and R. J. Davies, "Surface Force Measurements for Poly-L-Lysine - Effect of Ionic-Strength," *Colloids and Surfaces,* vol. 31, pp. 147-149, May 1988.

[55] P. J. Bryant, H. S. Kim, R. H. Deeken, and Y. C. Cheng, "Surface Force Measurements on Picometer and Piconewton Scales," *Journal of Vacuum Science & Technology a-Vacuum Surfaces and Films,* vol. 8, pp. 3502-3505, Jul-Aug 1990.

[56] E. Moy and A. W. Neumann, "Surface-Tension Values from Direct Force Measurements - Comments," *Journal of Colloid and Interface Science,* vol. 139, pp. 591-592, Oct 15 1990.

[57] D. Guzonas, D. Boils, and M. L. Hair, "Surface Force Measurements of Polystyrene-Block-Poly(Ethylene Oxide) Adsorbed from a Nonselective Solvent on Mica," *Macromolecules,* vol. 24, pp. 3383-3387, May 27 1991.

[58] S. Dhoot, E. D. Goddard, D. S. Murphy, and M. Tirrell, "Surface Force Measurements on Cationic Polymer Hyaluronic-Acid Mixtures on Mica," *Colloids and Surfaces,* vol. 66, pp. 91-96, Sep 28 1992.

[59] J. L. Parker, P. M. Claesson, and P. Attard, "Bubbles, Cavities, and the Long-Ranged Attraction between Hydrophobic Surfaces," *Journal of Physical Chemistry,* vol. 98, pp. 8468-8480, Aug 25 1994.

[60] L. S. Dorobantu, S. Bhattacharjee, J. M. Foght, and M. R. Gray, "Analysis of Force Interactions between AFM Tips and Hydrophobic Bacteria Using DLVO Theory," *Langmuir,* vol. 25, pp. 6968-6976, Jun 16 2009.

[61] W. A. Ducker, Z. G. Xu, and J. N. Israelachvili, "Measurements of Hydrophobic and Dlvo Forces in Bubble-Surface Interactions in Aqueous-Solutions," *Langmuir,* vol. 10, pp. 3279-3289, Sep 1994.

[62] R. M. Pashley, "Dlvo and Hydration Forces between Mica Surfaces in Li+,Na+,K+,and Cs+ Electrolyte-Solutions - a Correlation of Double-Layer and Hydration Forces with Surface Cation-Exchange Properties," *Journal of Colloid and Interface Science,* vol. 83, pp. 531-546, 1981.

[63] R. M. Pashley and J. N. Israelachvili, "Dlvo and Hydration Forces between Mica Surfaces in Mg-2+, Ca-2+, Sr-2+, and Ba-2+ Chloride Solutions," *Journal of Colloid and Interface Science,* vol. 97, pp. 446-455, 1984.

[64] R. H. Yoon and L. Q. Mao, "Application of extended DLVO theory .4. Derivation of flotation rate equation from first principles," *Journal of Colloid and Interface Science,* vol. 181, pp. 613-626, Aug 10 1996.

[65] Y. Ai, J. Liu, B. K. Zhang, and S. Qian, "Field Effect Regulation of DNA Trans location through a Nanopore," *Analytical Chemistry,* vol. 82, pp. 8217-8225, Oct 1 2010.

[66] H. Daiguji, P. D. Yang, and A. Majumdar, "Ion transport in nanofluidic channels," *Nano Letters,* vol. 4, pp. 137-142, Jan 2004.

[67] Y. H. He, M. Tsutsui, C. Fan, M. Taniguchi, and T. Kawai, "Gate Manipulation of DNA Capture into Nanopores," *Acs Nano,* vol. 5, pp. 8391-8397, Oct 2011.

[68] C. Hsu, T. W. Lo, D. J. Lee, and J. P. Hsu, "Electrophoresis of a Charge-Regulated Zwitterionic Particle: Influence of Temperature and Bulk Salt Concentration," *Langmuir,* vol. 29, pp. 2427-2433, Feb 19 2013.

[69] X. Z. Jin and N. R. Aluru, "Gated transport in nanofluidic devices," *Microfluidics and Nanofluidics,* vol. 11, pp. 297-306, Sep 2011.

[70] J. Matovic, N. Adamovic, F. Radovanovic, Z. Jaksic, and U. Schmid, "Field effect transistor based on ions as charge carriers," *Sensors and Actuators B-Chemical,* vol. 170, pp. 137-142, Jul 31 2012.

[71] K. P. Singh and M. Kumar, "Effect of gate length and dielectric thickness on ion and fluid transport in a fluidic nanochannel," *Lab on a Chip,* vol. 12, pp. 1332-1339, 2012.

[72] I. Larson, C. J. Drummond, D. Y. C. Chan, and F. Grieser, "Direct force measurements between silica and alumina," *Langmuir,* vol. 13, pp. 2109-2112, Apr 2 1997.

[73] O. I. Vinogradova, G. E. Yakubov, and H. J. Butt, "Forces between polystyrene surfaces in water-electrolyte solutions: Long-range attraction of two types?," *Journal of Chemical Physics,* vol. 114, pp. 8124-8131, May 8 2001.

[74] M. L. Fielden, R. A. Hayes, and J. Ralston, "Surface and capillary forces affecting air bubble-particle interactions in aqueous electrolyte," *Langmuir,* vol. 12, pp. 3721-3727, Jul 24 1996.

[75] L. Meagher and V. S. J. Craig, "Effect of Dissolved-Gas and Salt on the Hydrophobic Force between Polypropylene Surfaces," *Langmuir,* vol. 10, pp. 2736-2742, Aug 1994.

[76] H. K. Christenson, J. F. Fang, B. W. Ninham, and J. L. Parker, "Effect of Divalent Electrolyte on the Hydrophobic Attraction," *Journal of Physical Chemistry,* vol. 94, pp. 8004-8006, Oct 18 1990.

[77] J. L. Parker, "Surface Force Measurements in Surfactant Systems," *Progress in Surface Science,* vol. 47, pp. 205-271, Nov 1994.

[78] E. Kokkoli and C. F. Zukoski, "Effect of solvents on interactions between hydrophobic self-assembled monolayers," *Journal of Colloid and Interface Science,* vol. 209, pp. 60-65, Jan 1 1999.

[79] J. Drelich, J. Long, and A. Yeung, "Determining surface potential of the bitumen-water interface at nanoscale resolution using atomic force microscopy," *Canadian Journal of Chemical Engineering,* vol. 85, pp. 625-634, Oct 2007.

[80] J. M. Duan, "Interfacial forces between silica surfaces measured by atomic force microscopy," *Journal of Environmental Sciences-China,* vol. 21, pp. 30-34, 2009.

[81] B. V. Zhmud, A. Meurk, and L. Bergstrom, "Evaluation of surface ionization parameters from AFM data," *Journal of Colloid and Interface Science,* vol. 207, pp. 332-343, Nov 15 1998.

[82] A. L. Weisenhorn, P. Maivald, H. J. Butt, and P. K. Hansma, "Measuring Adhesion, Attraction, and Repulsion between Surfaces in Liquids with an Atomic-Force Microscope," *Physical Review B,* vol. 45, pp. 11226-11232, May 15 1992.

[83] G. Huttl, D. Beyer, and E. Muller, "Investigation of electrical double layers on SiO2 surfaces by means of force vs. distance measurements," *Surface and Interface Analysis,* vol. 25, pp. 543-547, Jun-Jul 1997.

[84] X. Y. Lin, F. Creuzet, and H. Arribart, "Atomic-Force Microscopy for Local Characterization of Surface Acid-Base Properties," *Journal of Physical Chemistry,* vol. 97, pp. 7272-7276, Jul 15 1993.

[85] L. Meagher, "Direct Measurement of Forces between Silica Surfaces in Aqueous Cacl2 Solutions Using an Atomic Force Microscope," *Journal of Colloid and Interface Science,* vol. 152, pp. 293-295, Aug 1992.

[86] M. W. Rutland and T. J. Senden, "Adsorption of the Poly(Oxyethylene) Nonionic Surfactant C12e5 to Silica - a Study Using Atomic Force Microscopy," *Langmuir,* vol. 9, pp. 412-418, Feb 1993.

[87] G. Toikka, R. A. Hayes, and J. Ralston, "Adhesion of iron oxide to silica studied by atomic force microscopy," *Journal of Colloid and Interface Science,* vol. 180, pp. 329-338, Jun 25 1996.

[88] T. J. Senden and C. J. Drummond, "Surface-Chemistry and Tip Sample Interactions in Atomic-Force Microscopy," *Colloids and Surfaces a-Physicochemical and Engineering Aspects,* vol. 94, pp. 29-51, Jan 2 1995.

[89] G. P. Dube and H. K. Dasgupta, "The London-van der Waals force between two particles in the form of discs," *Comptes Rendus Hebdomadaires Des Seances De L Academie Des Sciences,* vol. 209, pp. 340-342, 1939.

[90] J. N. Israelachvili, "Intermolecular and Surface Forces, 3rd Edition," *Intermolecular and Surface Forces, 3rd Edition,* pp. 1-674, 2011.

[91] H. J. Butt, B. Cappella, and M. Kappl, "Force measurements with the atomic force microscope: Technique, interpretation and applications," *Surface Science Reports,* vol. 59, pp. 1-152, Oct 2005.

[92] K. Umeda, N. Oyabu, K. Kobayashi, Y. Hirata, K. Matsushige, and H. Yamada, "High-Resolution Frequency-Modulation Atomic Force Microscopy in Liquids Using Electrostatic Excitation Method," *Applied Physics Express,* vol. 3, 2010.

[93] K. P. D. J. Karunanayake and Y. Hoshino, "Electrostatic force acting on conductive ball between electrodes," *Journal of Electrostatics,* vol. 68, pp. 91-95, Feb 2010.

[94] F. Johann, A. Hoffmann, and E. Soergel, "Impact of electrostatic forces in contact-mode scanning force microscopy," *Physical Review B,* vol. 81, Mar 1 2010.

[95] J. Kim, W. Jasper, R. L. Barker, and J. P. Hinestroza, "Application of Electrostatic Force Microscopy on Characterizing an Electrically Charged Fiber," *Fibers and Polymers,* vol. 11, pp. 775-781, Aug 2010.

[96] E. Chung, S. Yiacoumi, I. Lee, and C. Tsouris, "The Role of the Electrostatic Force in Spore Adhesion," *Environmental Science & Technology,* vol. 44, pp. 6209-6214, Aug 15 2010.

[97] K. Kikunaga, K. Toosaka, T. Kamohara, K. Sakai, and K. Nonaka, "A Study of Electrostatic Charge on Insulating Film by Electrostatic Force Microscopy," *Proceedings of the 13th International Conference on Electrostatics: Electrostatics 2011,* vol. 301, 2011.

[98] S. J. Chen and S. S. Pan, "A force measurement system based on an electrostatic sensing and actuating technique for calibrating force in a micronewton range with a resolution of nanonewton scale," *Measurement Science & Technology,* vol. 22, Apr 2011.

[99] C. H. Clausen, M. Dimaki, S. P. Panagos, E. Kasotakis, A. Mitraki, W. E. Svendsen, *et al.*, "Electrostatic Force Microscopy of Self-Assembled Peptide Structures," *Scanning,* vol. 33, pp. 201-207, Jul-Aug 2011

[100] C. H. Clausen, M. Dimaki, S. P. Panagos, E. Kasotakis, A. Mitraki, W. E. Svendsen, *et al.*, "Electrostatic Force Microscopy of Self-Assembled Peptide Structures," *Scanning,* vol. 33, pp. 201-207, Jul-Aug 2011.

[101] C. Riedel, A. Alegria, G. A. Schwartz, R. Arinero, J. Colmenero, and J. J. Saenz, "On the use of electrostatic force microscopy as a quantitative subsurface characterization technique: A numerical study," *Applied Physics Letters,* vol. 99, Jul 11 2011.

[102] D. S. Ginger, R. Giridharagopal, G. Rayermann, O. Reid, D. Moore, and G. Z. Shao, "Time-resolved electrostatic force microscopy on conjugated polymer blends," *Abstracts of Papers of the American Chemical Society,* vol. 242, Aug 28 2011.

[103] U. Zaghloul, B. Bhushan, F. Coccetti, P. Pons, and R. Plana, "Kelvin probe force microscopy-based characterization techniques applied for electrostatic MEMS/NEMS devices and bare dielectric films to investigate the dielectric and substrate charging phenomena," *Journal of Vacuum Science & Technology A,* vol. 29, Sep 2011.

[104] W. Gao, S. Goto, K. Hosobuchi, S. Ito, and Y. Shimizu, "A noncontact scanning electrostatic force microscope for surface profile measurement," *Cirp Annals-Manufacturing Technology,* vol. 61, pp. 471-474, 2012.

[105] S. Alvo, P. Lambert, M. Gauthier, and S. Regnier, "A van der Waals Force-Based Adhesion Model for Micromanipulation," *Adhesion Aspects in Mems/Nems,* pp. 77-90, 2010.

[106] G. V. Dedkov, A. A. Kanametov, and E. G. Dedkova, "Electrostatic and van der Waals forces in the air contact between the atomic force microscope probe and a conducting surface," *Technical Physics,* vol. 54, pp. 1801-1807, Dec 2009.

[107] M. S. Tomas, "Surface enhanced van der Waals force," *Physica Scripta,* vol. T135, Jul 2009.

[108] G. Palasantzas, V. B. Svetovoy, and P. J. van Zwol, "Influence of ultrathin water layer on the van der Waals/Casimir force between gold surfaces," *Physical Review B,* vol. 79, Jun 2009.

[109] J. Polesel-Maris, H. Guo, T. Zambelli, and S. Gauthier, "Mapping van der Waals forces with frequency modulation dynamic force microscopy," *Nanotechnology,* vol. 17, pp. 4204-4211, Aug 28 2006.

[110] A. K. Mohapatra and C. S. Unnikrishnan, "Measurement of the van der Waals force using reflection of cold atoms from magnetic thin-film atom mirrors," *Europhysics Letters,* vol. 73, pp. 839-845, Mar 2006.

[111] A. Ramezani, A. Alasty, and J. Akbari, "Influence of van der Waals force on the pull-in parameters of cantilever type nanoscale electrostatic actuators," *Proceedings of the 8th Biennial Conference on Engineering Systems Design and Analysis, Vol 3,* pp. 43-49, 2006.

[112] X. Q. He, S. Kitipornchai, C. M. Wang, and K. M. Liew, "Modeling of van der Waals force for infinitesimal deformation of multi-walled carbon nanotubes treated as cylindrical shells," *International Journal of Solids and Structures,* vol. 42, pp. 6032-6047, Nov 2005.

[113] S. Y. Buhmann, H. T. Dung, T. Kampf, L. Knoll, and D. G. Welsch, "Atoms near magnetodielectric bodies: van der Waals energy and the Casimir-Polder force," *Optics and Spectroscopy,* vol. 99, pp. 466-474, Sep 2005.

[114] N. Liu, Y. L. Bai, M. F. Xia, and F. J. Ke, "Combined effect of surface tension, gravity and van der Waals force induced by a non-contact probe tip on the shape of liquid surface," *Chinese Physics Letters,* vol. 22, pp. 2012-2015, Aug 2005.

[115] S. Kogan, "van der Waals force noise: Quantum theory of fluctuations," *Physical Review B,* vol. 72, Aug 2005.

[116] A. Vilinska and K. H. Rao, "Surface thermodynamics and extended DLVO theory of Leptospirillum ferrooxidans cells' adhesion on sulfide minerals," *Minerals & Metallurgical Processing,* vol. 28, pp. 151-158, Aug 2011.

[117] L. Boinovich, "DLVO forces in thin liquid films beyond the conventional DLVO theory," *Current Opinion in Colloid & Interface Science,* vol. 15, pp. 297-302, Oct 2010.

[118] M. L. Sushko and A. L. Shluger, "DLVO theory for like-charged polyelectrolyte and surface interactions," *Materials Science & Engineering C-Biomimetic and Supramolecular Systems,* vol. 27, pp. 1090-1095, Sep 2007.

[119] J. M. Sharp and R. B. Dickinson, "Direct evaluation of DLVO theory for predicting long-range forces between a yeast cell and a surface," *Langmuir,* vol. 21, pp. 8198-8203, Aug 30 2005.

[120] H. D. Yaros, J. Newman, and C. J. Radke, "Evaluation of DLVO theory with disjoining-pressure and film-conductance measurements of common-black films stabilized with sodium dodecyl sulfate," *Journal of Colloid and Interface Science,* vol. 262, pp. 442-455, Jun 15 2003.

[121] S. Croll, "DLVO theory applied to TiO2 pigments and other materials in latex paints," *Progress in Organic Coatings,* vol. 44, pp. 131-146, Apr 2002.

[122] T. Missana and A. Adell, "On the applicability of DLVO theory to the prediction of clay colloids stability," *Journal of Colloid and Interface Science,* vol. 230, pp. 150-156, Oct 1 2000.

[123] Z. Adamczyk and P. Weronski, "Application of the DLVO theory for particle deposition problems," *Advances in Colloid and Interface Science,* vol. 83, pp. 137-226, Dec 1 1999.

[124] B. W. Ninham, "On progress in forces since the DLVO theory," *Advances in Colloid and Interface Science,* vol. 83, pp. 1-17, Dec 1 1999.

[125] N. V. Churaev, "The DLVO theory in Russian colloid science," *Advances in Colloid and Interface Science,* vol. 83, pp. 19-32, Dec 1 1999.

[126] S. Atalay, M. Barisik, A. Beskok, and S. Z. Qian, "Surface Charge of a Nanoparticle Interacting with a Flat Substrate," *Journal of Physical Chemistry C,* vol. 118, pp. 10927-10935, May 22 2014.

[127] Z. H. Xu, R. Chi, T. Difeo, and J. A. Finch, "Surface forces between sphalerite and silica particles in aqueous solutions," *Journal of Adhesion Science and Technology,* vol. 14, pp. 1813-1827, 2000.

[128] J. A. Last, P. Russell, P. F. Nealey, and C. J. Murphy, "The Applications of Atomic Force Microscopy to Vision Science," *Investigative Ophthalmology & Visual Science,* vol. 51, pp. 6083-6094, Dec 2010.

[129] N. Jalili and K. Laxminarayana, "A review of atomic force microscopy imaging systems: application to molecular metrology and biological sciences," *Mechatronics,* vol. 14, pp. 907-945, Oct 2004.

[130] E. A-Hassan, W. F. Heinz, M. D. Antonik, N. P. D'Costa, S. Nageswaran, C. A. Schoenenberger, *et al.*, "Relative microelastic mapping of living cells by atomic force microscopy," *Biophysical Journal,* vol. 74, pp. 1564-1578, Mar 1998.

[131] K. D. Costa, A. J. Sim, and F. C. P. Yin, "Non-Hertzian approach to analyzing mechanical properties of endothelial cells probed by atomic force microscopy," *Journal of Biomechanical Engineering-Transactions of the Asme,* vol. 128, pp. 176-184, Apr 2006.

[132] K. D. Costa and F. C. P. Yin, "Analysis of indentation: Implications for measuring mechanical properties with atomic force microscopy," *Journal of Biomechanical Engineering-Transactions of the Asme,* vol. 121, pp. 462-471, Oct 1999.

[133] M. D'Acunto, G. Ciardelli, P. Narducci, A. Rechichi, and P. Giusti, "Phospholipid-polyurethane adhesion force observed by atomic force microscopy," *Materials Letters,* vol. 59, pp. 1627-1633, Jun 2005.

[134] E. M. Darling, S. Zauscher, J. A. Block, and F. Guilak, "A thin-layer model for viscoelastic, stress-relaxation testing of cells using atomic force microscopy: Do cell properties reflect metastatic potential?," *Biophysical Journal,* vol. 92, pp. 1784-1791, Mar 1 2007.

[135] E. M. Darling, S. Zauscher, and F. Guilak, "Viscoelastic properties of zonal articular chondrocytes measured by atomic force microscopy," *Osteoarthritis and Cartilage,* vol. 14, pp. 571-579, Jun 2006.

[136] H. Haga, M. Nagayama, K. Kawabata, E. Ito, T. Ushiki, and T. Sambongi, "Time-lapse viscoelastic imaging of living fibroblasts using force modulation mode in AFM," *Journal of Electron Microscopy,* vol. 49, pp. 473-481, 2000.

[137] G. E. Kempson, M. A. R. Freeman, and S. A. V. Swanson, "Determination of a Creep Modulus for Articular Cartilage from Indentation Tests on Human Femoral Head," *Journal of Biomechanics,* vol. 4, pp. 239-&, 1971.

[138] W. M. Lai, J. S. Hou, and V. C. Mow, "A Triphasic Theory for the Swelling and Deformation Behaviors of Articular-Cartilage," *Journal of Biomechanical Engineering-Transactions of the Asme,* vol. 113, pp. 245-258, Aug 1991.

[139] A. F. Mak, "Unconfined Compression of Hydrated Viscoelastic Tissues - a Biphasic Poroviscoelastic Analysis," *Biorheology,* vol. 23, pp. 371-383, 1986.

[140] J. M. Mattice, A. G. Lau, M. L. Oyen, and R. W. Kent, "Spherical indentation load-relaxation of soft biological tissues," *Journal of Materials Research,* vol. 21, pp. 2003-2010, Aug 2006.

[141] M. Radmacher, R. W. Tilmann, and H. E. Gaub, "Imaging Viscoelasticity by Force Modulation with the Atomic Force Microscope," *Biophysical Journal,* vol. 64, pp. 735-742, Mar 1993.

[142] C. Y. Zhang and Y. W. Zhang, "Effects of membrane pre-stress and intrinsic viscoelasticity on nanoindentation of cells using AFM," *Philosophical Magazine,* vol. 87, pp. 3415-3435, 2007.

[143] P. Lemoine and J. M. McLaughlin, "Nanomechanical measurements on polymers using contact mode atomic force microscopy," *Thin Solid Films,* vol. 339, pp. 258-264, Feb 8 1999.

[144] D. J. Taatjes, A. S. Quinn, and E. G. Bovill, "Imaging of collagen type III in fluid by atomic force microscopy," *Microscopy Research and Technique,* vol. 44, pp. 347-352, Mar 1 1999.

[145] M. Stolz, R. Gottardi, R. Raiteri, S. Miot, I. Martin, R. Imer, *et al.*, "Early detection of aging cartilage and osteoarthritis in mice and patient samples using atomic force microscopy," *Nature Nanotechnology,* vol. 4, pp. 186-192, Mar 2009.

[146] S. Tripathy and E. J. Berger, "Quasi-linear viscoelastic properties of costal cartilage using atomic force microscopy," *Computer Methods in Biomechanics and Biomedical Engineering,* vol. 15, pp. 475-486, 2012.

[147] K. A. Athanasiou, M. P. Rosenwasser, J. A. Buckwalter, T. I. Malinin, and V. C. Mow, "Interspecies Comparisons of Insitu Intrinsic Mechanical-Properties of Distal Femoral Cartilage," *Journal of Orthopaedic Research,* vol. 9, pp. 330-340, May 1991.

[148] R. Crockett, S. Roos, P. Rossbach, C. Dora, W. Born, and H. Troxler, "Imaging of the surface of human and bovine articular cartilage with ESEM and AFM," *Tribology Letters,* vol. 19, pp. 311-317, Aug 2005.

[149] B. Y. Guo, D. H. Liao, X. Y. Li, Y. J. Zeng, and Q. H. Yang, "Age and gender related changes in biomechanical properties of healthy human costal cartilage," *Clinical Biomechanics,* vol. 22, pp. 292-297, Mar 2007.

[150] W. C. Hayes, L. M. Keer, G. Herrmann, and L. F. Mockros, "A mathematical analysis for indentation tests of articular cartilage," *J Biomech,* vol. 5, pp. 541-51, Sep 1972.

[151] R. Y. Hori and L. F. Mockros, "Indentation tests of human articular cartilage," *J Biomech,* vol. 9, pp. 259-68, 1976.

[152] K. Hu, P. Radhakrishnan, R. V. Patel, and J. J. Mao, "Regional structural and viscoelastic properties of fibrocartilage upon dynamic nanoindentation of the articular condyle," *Journal of Structural Biology,* vol. 136, pp. 46-52, Oct 2001.

[153] A. Lau, M. L. Oyen, R. W. Kent, D. Murakami, and T. Torigaki, "Indentation stiffness of aging human costal cartilage," *Acta Biomaterialia,* vol. 4, pp. 97-103, Jan 2008.

[154] T. Lyyra, J. Jurvelin, P. Pitkanen, U. Vaatainen, and I. Kiviranta, "Indentation Instrument for the Measurement of Cartilage Stiffness under Arthroscopic Control," *Medical Engineering & Physics,* vol. 17, pp. 395-399, Jul 1995.

[155] A. F. Mak, W. M. Lai, and V. C. Mow, "Biphasic Indentation of Articular-Cartilage .1. Theoretical-Analysis," *Journal of Biomechanics,* vol. 20, pp. 703-714, 1987.

[156] M. A. Lopez, A. R. Shah, J. G. Westine, K. O'Grady, and D. M. Toriumi, "Analysis of the physical properties of costal cartilage in a porcine model," *Archives of Facial Plastic Surgery,* vol. 9, pp. 35-39, Jan-Feb 2007.

[157] R. K. Korhonen, M. S. Laasanen, J. Toyras, J. Rieppo, J. Hirvonen, H. J. Helminen, *et al.*, "Comparison of the equilibrium response of articular cartilage in unconfined compression, confined compression and indentation," *Journal of Biomechanics,* vol. 35, pp. 903-909, Jul 2002.

[158] C. Herberhold, S. Faber, T. Stammberger, M. Steinlechner, R. Putz, K. H. Englmeier, *et al.*, "In situ measurement of articular cartilage deformation in intact femoropatellar joints under static loading," *Journal of Biomechanics,* vol. 32, pp. 1287-1295, Dec 1999.

[159] P. A. Parmar, L. W. Chow, J. P. St-Pierre, C. M. Horejs, Y. Y. Peng, J. A. Werkmeister, *et al.*, "Collagen-mimetic peptide-modifiable hydrogels for articular cartilage regeneration," *Biomaterials,* vol. 54, pp. 213-225, Jun 2015.

[160] N. A. Zelenski, H. A. Leddy, J. Sanchez-Adams, J. Z. Zhang, P. Bonaldo, W. Liedtke, *et al.*, "Type VI Collagen Regulates Pericellular Matrix Properties, Chondrocyte Swelling, and Mechanotransduction in Mouse Articular Cartilage," *Arthritis & Rheumatology,* vol. 67, pp. 1286-1294, May 2015.

[161] D. Armani, C. Liu, and N. Aluru, "Re-configurable fluid circuits by PDMS elastomer micromachining," *Mems '99: Twelfth Ieee International Conference on Micro Electro Mechanical Systems, Technical Digest,* pp. 222-227, 1999.

[162] J. E. Sader and S. P. Jarvis, "Accurate formulas for interaction force and energy in frequency modulation force spectroscopy," *Applied Physics Letters,* vol. 84, pp. 1801-1803, Mar 8 2004.

[163] J. P. R. O. Orgel, J. D. S. Antonio, and O. Antipova, "Molecular and structural mapping of collagen fibril interactions," *Connective Tissue Research,* vol. 52, pp. 2-17, Feb 2011.

[164] D. Maugis, "On the contact and adhesion of rough surfaces," *Journal of Adhesion Science and Technology,* vol. 10, pp. 161-175, 1996.

[165] B. V. Derjaguin, V. M. Muller, and Y. P. Toporov, "Effect of Contact Deformations on Adhesion of Particles," *Journal of Colloid and Interface Science,* vol. 53, pp. 314-326, 1975.

[166] V. L. Popov, "Contact Mechanics and Friction: Physical Principles and Applications," *Contact Mechanic and Friction: Physical Principles and Applications,* pp. 1-362, 2010.

[167] Z. L. Zhou, C. X. Zheng, S. Li, X. F. Zhou, Z. H. Liu, Q. T. He, *et al.*, "AFM nanoindentation detection of the elastic modulus of tongue squamous carcinoma cells with different metastatic potentials," *Nanomedicine-Nanotechnology Biology and Medicine,* vol. 9, pp. 864-874, Oct 2013.

[168] X. F. Cai, S. J. Gao, J. Y. Cai, Y. Z. Wu, and H. Deng, "Artesunate Induced Morphological and Mechanical Changes of Jurkat Cell Studied by AFM," *Scanning,* vol. 31, pp. 83-89, Mar-Apr 2009.

[169] S. C. Hsiao, A. K. Crow, W. A. Lam, C. R. Bertozzi, D. A. Fletcher, and M. B. Francis, "DNA-Coated AFM Cantilevers for the Investigation of Cell Adhesion and the Patterning of Live Cells," *Angewandte Chemie-International Edition,* vol. 47, pp. 8473-8477, 2008.

[170] A. M. Whited and P. S. H. Park, "Atomic force microscopy: A multifaceted tool to study membrane proteins and their interactions with ligands," *Biochimica Et Biophysica Acta-Biomembranes,* vol. 1838, pp. 56-68, Jan 2014.

[171] M. Zweyer, B. Troian, V. Spreafico, and S. Prato, "SNOM on cell thin sections: observation of Jurkat and MDAMB453 cells," *Journal of Microscopy-Oxford,* vol. 229, pp. 440-446, Mar 2008.

[172] H. Jin, S. Y. Ma, B. Song, L. N. Ma, J. Pi, X. X. Chen, *et al.*, "Liposome impaired the adhesion and spreading of HEK293 cells: an AFM study," *Scanning,* vol. 33, pp. 413-418, Nov-Dec 2011.

[173] R. Afrin, T. Yamada, and A. Ikai, "Analysis of force curves obtained on the live cell membrane using chemically modified AFM probes (vol 100, pg 187, 2004)," *Ultramicroscopy,* vol. 103, pp. 253-253, Jun 2005.

[174] R. Afrin, T. Yamada, and A. Ikai, "Analysis of force curves obtained on the live cell membrane using chemically modified AFM probes," *Ultramicroscopy,* vol. 100, pp. 187-195, Aug 2004.

[175] Z. Balint, I. A. Krizbai, I. Wilhelm, A. E. Farkas, A. Parducz, Z. Szegletes, *et al.*, "Changes induced by hyperosmotic mannitol in cerebral endothelial cells: an atomic force microscopic study," *Eur Biophys J,* vol. 36, pp. 113-20, Feb 2007.

[176] H. Brochu and P. Vermette, "Young's moduli of surface-bound liposomes by atomic force microscopy force measurements," *Langmuir,* vol. 24, pp. 2009-2014, Mar 4 2008.

[177] S. E. Cross, Y. S. Jin, J. Rao, and J. K. Gimzewski, "Nanomechanical analysis of cells from cancer patients," *Nat Nanotechnol,* vol. 2, pp. 780-3, Dec 2007.

[178] J. A. Hessler, A. Budor, K. Putchakayala, A. Mecke, D. Rieger, M. M. Banaszak Holl, *et al.*, "Atomic force microscopy study of early morphological changes during apoptosis," *Langmuir,* vol. 21, pp. 9280-6, Sep 27 2005.

[179] T. A. Stupina, M. A. Stepanov, and M. P. Teplen'kii, "Role of Subchondral Bone in the Restoration of Articular Cartilage," *Bulletin of Experimental Biology and Medicine,* vol. 158, pp. 820-823, Apr 2015.

[180] E. Neumann and K. Rosenheck, "Permeability changes induced by electric impulses in vesicular membranes," *J Membr Biol,* vol. 10, pp. 279-90, Dec 29 1972.

[181] K. H. Schoenbach, S. J. Beebe, and E. S. Buescher, "Intracellular effect of ultrashort electrical pulses," *Bioelectromagnetics,* vol. 22, pp. 440-8, Sep 2001.

[182] T. R. Gowrishankar and J. C. Weaver, "Electrical behavior and pore accumulation in a multicellular model for conventional and supra-electroporation," *Biochem Biophys Res Commun,* vol. 349, pp. 643-53, Oct 20 2006.

[183] E. Tekle, R. D. Astumian, and P. B. Chock, "Electro-permeabilization of cell membranes: effect of the resting membrane potential," *Biochem Biophys Res Commun,* vol. 172, pp. 282-7, Oct 15 1990.

[184] Z. Vasilkoski, A. T. Esser, T. R. Gowrishankar, and J. C. Weaver, "Membrane electroporation: The absolute rate equation and nanosecond time scale pore creation," *Phys Rev E Stat Nonlin Soft Matter Phys,* vol. 74, p. 021904, Aug 2006.

[185] L. Chopinet, C. Roduit, M. P. Rols, and E. Dague, "Destabilization induced by electropermeabilization analyzed by atomic force microscopy," *Biochim Biophys Acta,* vol. 1828, pp. 2223-9, Sep 2013.

[186] E. L. Hotoiu and J. Deconinck, "A novel pulse shortcut strategy for simulating nano-second pulse electrochemical micro-machining," *Journal of Applied Electrochemistry,* vol. 44, pp. 1225-1238, Nov 2014.

[187] B. Thornton, T. Sakka, T. Masamura, A. Tamura, T. Takahashi, and A. Matsumoto, "Long-duration nano-second single pulse lasers for observation of spectra from bulk liquids at high hydrostatic pressures," *Spectrochimica Acta Part B-Atomic Spectroscopy,* vol. 97, pp. 7-12, Jul 1 2014.

[188] F. Pliquett and S. Wunderlich, "Relationship between Cell Parameters and Pulse Deformation Due to These Cells as Well as Its Change after Electrically Induced Membrane Breakdown," *Bioelectrochemistry and Bioenergetics,* vol. 10, pp. 467-475, 1983.

[189] S. P. Akeson and H. C. Mel, "Voltage-Dependent Membrane Conductance in Red-Blood-Cells and Resealed Ghosts, as Measured by Resistive Pulse Spectroscopy," *Biophysical Journal,* vol. 33, pp. A76-A76, 1981.

[190] T. Yan, R. Sun, H. Deng, B. Tan, and N. Ao, "The morphological and biomechanical changes of keratocytes cultured on modified p (HEMA-MMA) hydrogel studied by AFM," *Scanning,* vol. 31, pp. 246-52, Nov-Dec 2009.

[191] Z. Zhou, C. Zheng, S. Li, X. Zhou, Z. Liu, Q. He, *et al.*, "AFM nanoindentation detection of the elastic modulus of tongue squamous carcinoma cells with different metastatic potentials," *Nanomedicine,* vol. 9, pp. 864-74, Oct 2013.

[192] Z. Y. Liu, S. Persson, and Y. Zhang, "The connection of cytoskeletal network with plasma membrane and the cell wall," *Journal of Integrative Plant Biology,* vol. 57, pp. 330-340, Apr 2015.

[193] F. Baumgart and G. J. Schutz, "Detecting protein association at the T cell plasma membrane," *Biochimica Et Biophysica Acta-Molecular Cell Research,* vol. 1853, pp. 791-801, Apr 2015.

[194] A. G. Pakhomov, J. F. Kolb, J. A. White, R. P. Joshi, S. Xiao, and K. H. Schoenbach, "Long-lasting plasma membrane permeabilization in mammalian cells by nanosecond pulsed electric field (nsPEF)," *Bioelectromagnetics,* vol. 28, pp. 655-63, Dec 2007.

[195] J. A. White, P. F. Blackmore, K. H. Schoenbach, and S. J. Beebe, "Stimulation of capacitative calcium entry in HL-60 cells by nanosecond pulsed electric fields," *J Biol Chem,* vol. 279, pp. 22964-72, May 28 2004.

[196] I. Semenov, S. Xiao, and A. G. Pakhomov, "Primary pathways of intracellular Ca(2+) mobilization by nanosecond pulsed electric field," *Biochim Biophys Acta,* vol. 1828, pp. 981-9, Mar 2013.

[197] A. G. Pakhomov, R. Shevin, J. A. White, J. F. Kolb, O. N. Pakhomova, R. P. Joshi, *et al.*, "Membrane permeabilization and cell damage by ultrashort electric field shocks," *Arch Biochem Biophys,* vol. 465, pp. 109-18, Sep 1 2007.

[198] P. Lipton, "Lysosomal Membrane Permeabilization as a Key Player in Brain Ischemic Cell Death: a "Lysosomocentric" Hypothesis for Ischemic Brain Damage," *Translational Stroke Research,* vol. 4, pp. 672-684, Dec 2013.

[199] M. Stacey, J. Stickley, P. Fox, V. Statler, K. Schoenbach, S. J. Beebe, *et al.*, "Differential effects in cells exposed to ultra-short, high intensity electric fields: cell survival, DNA damage, and cell cycle analysis," *Mutat Res,* vol. 542, pp. 65-75, Dec 9 2003.

[200] M. Stacey, P. Fox, S. Buescher, and J. Kolb, "Nanosecond pulsed electric field induced cytoskeleton, nuclear membrane and telomere damage adversely impact cell survival," *Bioelectrochemistry,* vol. 82, pp. 131-4, Oct 2011.

[201] K. Nakamura, J. Shimizu, N. Kataoka, K. Hashimoto, T. Ikeda, H. Fujio, *et al.*, "Altered nano/micro-order elasticity of pulmonary artery smooth muscle cells of patients with idiopathic pulmonary arterial hypertension," *International Journal of Cardiology,* vol. 140, pp. 102-107, Apr 1 2010.

[202] A. Buxboim, I. L. Ivanovska, and D. E. Discher, "Matrix elasticity, cytoskeletal forces and physics of the nucleus: how deeply do cells 'feel' outside and in?," *Journal of Cell Science,* vol. 123, pp. 297-308, Feb 1 2010.

[203] Parsegia.Va and D. Gingell, "Electrostatic Interaction across a Salt Solution between 2 Bodies Bearing Unequal Charges," *Biophysical Journal,* vol. 12, pp. 1192-&, 1972.

[204] D. Dutta, A. Asmar, and M. Stacey, "Effects of nanosecond pulse electric fields on cellular elasticity," *Micron,* vol. 72, pp. 15-20, May 2015.

VITA

DIGANTA DUTTA
1069 West 41st Street, Apt. 6, Norfolk, VA 23508, USA
Cell: (509) 432-9006, E-mail: ddutt001@odu.edu

EDUCATION

Old Dominion University, Norfolk, Virginia, USA

- **Ph.D. in Mechanical and Aerospace Engineering (August, 2015)**
  - Dissertation Title: Nano Scale mechanical analysis of biological cells, tissues and materials using Atomic Force Microscopy

University of Ulsan, Ulsan, South Korea

- **M.S. in Automotive and Mechanical Engineering** (December 2009)
  - Thesis Title: Effect of pre-mixture condition on HCCI engine and Environmental factor analysis by using primary reference fuel

Chittagong University of Engineering and Technology, Chittagong, Bangladesh

- **B.S. in Mechanical Engineering** (April 2004)
  - Thesis Title: Design of Engine Block the help of Pro-E